Theoretical and numerical studies of atmospheric boundary-layer flows over complex terrain

THÈSE N^{O} 7000 (2016)

PRÉSENTÉE LE 18 AVRIL 2016

À LA FACULTÉ DE L'ENVIRONNEMENT NATUREL, ARCHITECTURAL ET CONSTRUIT
LABORATOIRE DES SCIENCES CRYOSPHÉRIQUES
PROGRAMME DOCTORAL EN MÉCANIQUE

ÉCOLE POLYTECHNIQUE FÉDÉRALE DE LAUSANNE

POUR L'OBTENTION DU GRADE DE DOCTEUR ÈS SCIENCES

PAR

Marco Giovanni GIOMETTO

acceptée sur proposition du jury:

Prof. F. Gallaire, président du jury
Dr J. Fang, Prof. M. Parlange, directeurs de thèse
Prof. C. Meneveau, rapporteur
Prof. M. Rotach, rapporteur
Prof. M. Lehning, rapporteur

ÉCOLE POLYTECHNIQUE
FÉDÉRALE DE LAUSANNE

Suisse
2016

Science, my lad, is made up of mistakes,
but they are mistakes which it is useful to make,
because they lead little by little to the truth.
— In *Jules Verne, A Journey to the Center of the Earth (1864)*

To my family

Acknowledgements

First and foremost, I wish to thank Prof. Marc Parlange and Dr. Jiannong Fang for being more than thesis directors during these years at EPFL. Marc introduced me to the fascinating world of environmental fluid mechanics, and has provided unique opportunities to grow my knowledge and to travel around the world. His dedication in life, both as a manager and as a man, have made him a great role model throughout these years, opening new and inspiring perspectives. Jiannong has been a constant guide during my studies; his unconditional support and great abstraction capabilities have resulted in a most profitable collaboration. They both contributed immensely to my personal and academic development, taught me to aim high and to passionately pursue my interests, which ultimately led to this dissertation.

A big thank you also goes to Prof. Michael Lehning (Michi), for "adopting" me as the EFLUM laboratory closed, and for providing the basis for my future research. Michi sets a perfect example of an organized and highly-productive researcher, and I have constantly benefited from his advice.

A special acknowledgement goes to my collaborators Prof. Charles Meneveau and Prof. Gabriel Katul. The possibility to share fluid mechanical problems with two such masters of the field, as well as their talent and knowledge, have been wonderful gifts.

Thank you to Prof. Gallaire and Prof. Rotach, members of this thesis evaluation committee, for their constructive advices, which allowed to improve the quality of the study.

Another big thank you goes to Marie-Jo Pellaud, who kept the EFLUM lab in place, and represented the perfect complement to Marc's personality.

I am grateful to my ex officemate Prof. Marc Calaf, for his great help during the initial years of my Ph.D., always boosting my confidence and engaging in intricate discussions on physical and numerical problems. He has also always been a role model in terms of general organization, which I unfortunately still lack.

Sincere thanks go to my officemates Ernesto Trujillo and Francesco Comola, for they made my EPFL days pleasant, with their irony, with all the interesting scientific (and unrelated) discussions, and with their constant efforts to get me out for a beer after work.

Thank you to Jordi Cotela and Enrico Fusto, two good friends, hardcore coders and passionate scientists, with whom I was lucky enough to collaborate during the first years of my Ph.D. and whom thought me that dedication and team spirit are key elements of successful research.

I am also indebted to my friends/colleagues of the EFLUM and CRYOS laboratories at EPFL, who made these years special in many ways. In particular, I want to thank Raphael Mutzner, Theophile Mande and Francesco Ciocca, for being the best travel mates ever, Holly Oldroyd and Varun Sharma, for sharing a sincere passion towards turbulence and boundary-layer processes, and for the many scientific interactions. I acknowledge Steven Weiss, for our visionary science discussions, Hendrik Huwald, our senior scientist, for his central organizational role and for his advice throughout these years, Annelen Kahl, the most sporty person I've ever met, Stuart Bartlett, for the interesting discussions on non-equilibrium thermodynamics and fast bikes, and Marc Diebold, Tristan Brauchli and Gallice Aurelien, for the interactions we've had during these years and for their kindness.

In addition, I am grateful to Prof. Gallaire, Prof. Monkewitz, and Prof. Porté-Agel for their teaching on fluid mechanics at EPFL, for they greatly contributed to my education.

A particular recognition goes also to the Universitá di Padova (Italy), and to the International Center for Computational Methods in Engineering (Spain), where I spent exciting years during my bachelor and master studies, which set the basis for my scientific development.

Thanks to all my friends in Italy – whose list would be too long and incomplete – for keeping me up during these tough years, recharging my batteries during Italian holidays.

On a more personal note, a very special thank goes to my family, for their constant care, patience and attention. They are my main source of energy and motivation.

Finally, I acknowledge the CSCS supercomputing center in Lugano for providing computational resources and first-class support, and the Swiss National Science Foundation for generously financing my research activities.

Lausanne, 23 January 2016 M. G.

Abstract

Atmospheric boundary-layer (ABL) flows over complex terrain have been the focus of active research, given their impact on weather and climate variability. Surface complexity is understood in a broad sense and includes variation in roughness properties, inclination of the underlying surface, presence of heterogeneous forcing mechanisms (e.g., buoyancy, humidity), to name but a few. Most assumptions of classical boundary-layer similarity theory do not hold under such conditions, complicating matters from both a measurement and modeling perspective. Despite the increasing body of literature on the subject, the dynamics and thermodynamics of most problems remain poorly understood, making them a challenging research area. Here, a combination of analytical and numerical approaches are used to address two relevant problems where the applicability of Monin-Obukhov similarity theory (MOST) is questionable: the problem of turbulent slope flows, and ABL flows over multi-scale rough surfaces.

The first part of the thesis focuses on slope flows: the building blocks of local weather in mountainous regions, and key players in the surface-atmosphere exchange of mass, momentum and energy. To understand the system conceptually, a closed-form analytic solution to the Prandtl slope flow model is first derived, prescribing transfer coefficients in accordance to the O'Brien K-theory model. Profiles are characterized by stark variations in both phase and amplitude of extrema compared to the classic constant-K and a more recent solution which is valid within the Wentzel-Kramers-Brillouin (WKB) theory, shedding new light on this longstanding geophysical problem. In addition, direct numerical simulation (DNS) is used to study the turbulent structure of anabatic and katabatic flows, and to describe the sensitivity of the solution to variations in the parameter space, within the conceptual framework of the Prandtl model. Variations in the sloping angle from the vertical wall ($\alpha = 90^\circ$) setup are shown to induce a progressive departure of averaged profiles between the two flow regimes, ultimately resulting in stark differences at gentle sloping angles. The thermodynamical mechanisms responsible for sustaining mean and turbulent kinetic energy are used to further distinguish between flow regimes, and to propose a qualitative partition of the boundary layer in slope flows. The DNS setup is additionally adopted to identify coherent structures in katabatic flows over steep slopes. Coherent motions are responsible for the maintenance of turbulence in the ABL, hence their characterization is of fundamental importance toward a better understanding of boundary-layer dynamics. Packets of hairpins are found to connect in the streamwise direction to form large-scale motions (LSMs). In the katabatic flow, hairpins are characterized by a head located upstream in the return flow region and by tails protruding downstream into the inner regions of the flow. For the lower sloping angles that are considered, it is shown how LSMs align to form very-large-scale motions (VLSMs). LSMs and VLSMs are found to be the dominant contributors to streamwise momentum variance and turbulent momentum transfer in the above-jet regions of katabatic flows.

Next, drag properties of realistic fractal-like sea ice surface morphologies are examined within the large-eddy simulation (LES) framework, considering fully-developed, pressure-driven turbulent boundary-layer flows. The effects of large-scale surface features on wind flow are accounted for by an immersed boundary method (IBM). Conversely, the drag forces caused by subgrid-scale features are modeled through a novel dynamic roughness approach, in which the hydrodynamic roughness length parameter is determined using the first-principles based constraint that the total momentum flux (drag) must be independent of the grid-filter scale. This approach leads to accurate flow predictions (resolution invariant) and provides an estimate of the otherwise unknown roughness parameter for sea ice surfaces, of use in climate, weather prediction and scalar transport models to evaluate the hydrodynamic roughness length.

Keywords: anabatic flow, direct numerical simulation, dynamic surface roughness model, energy budget, immersed boundary method, katabatic flow, large-eddy simulation, Prandtl model, rough surfaces, turbulence.

Sommario

Lo studio dello strato limite atmosferico su terreni complessi è stato oggetto di attiva ricerca, data la sua importanza a livello meteorologico e climatologico. Il concetto di complessità è inteso in senso lato ed include ad esempio variazioni spaziali della scabrezza, variazioni spaziali delle forzanti del sistema (e.g., temperatura, umidità), o un'inclinazione media della superficie. Le principali ipotesi delle classiche formulazioni basate sul metodo della somiglianza non sono rispettate in tali condizioni, complicando la situazione sia da un punto di vista modellistico che di misurazione. Nonostante i numerosi studi, tale problema rimane poco compreso, e rappresenta quindi un terreno fertile di ricerca. Questa tesi si concentra su due tra i principali sistemi in cui la teoria di Monin ed Obukhov (MOST) non è applicabile: il problema dei flussi termici su superfici inclinate, ed il problema dei flussi atmosferici su superfici caratterizzate da un ampio spettro di scale di scabrezza.

La prima parte della tesi si concentra sul problema dei venti generati da flussi termici su superfici inclinate: questi sistemi sono alla base della meteorologia in regioni montane, e giocano un ruolo fondamentale nello scambio di massa, di quantità di moto ed di energia tra la superficie e l'atmosfera. Una soluzione analitica del modello di Prandtl è dapprima proposta per inquadrare il problema da un punto di vista concettuale. Effetti dovuti alla turbolenza sono parametrizzati attraverso la teoria K, assumendo coefficienti di trasferimento secondo il modello di O'Brien. I profili di velocità e di galleggiamento sono caratterizzati da variazioni significative rispetto la soluzione di Prandtl (K costante) e rispetto una più recente soluzione approssimata, basata sulla teoria WKB (da Wentzel-Kramers-Brillouin), dando nuova luce al problema. In seguito, venti catabatici ed anabatici sono studiati attraverso il metodo di simulazione numerica diretta, per caratterizzarne la struttura turbolenta e per definire la dipendenza della soluzione dai parametri del sistema. Variazioni nell'angolo di inclinazione della superficie rispetto la verticale ($\alpha = 90°$) risultano in una progressiva differenziazione dei due regimi (anabatico e catabatico), i quali sono significativamente diversi per modesti angoli di inclinazione. I meccanismi termodinamici alla base del sostentamento dell'energia del flusso medio e dell'energia delle fluttuazioni turbolente sono successivamente analizzati per i due regimi di vento, e utilizzati per proporre una partizione dello strato limite in venti anabatici e catabatici.

Lo stesso setup è in seguito utilizzato per identificare strutture coerenti in flussi catabatici su superfici quasi verticali (angolo di inclinazione $\alpha \geq 60°$). Le strutture coerenti all'interno dello strato limite atmosferico sono responsabili per il sostentamento della turbolenza, e una loro caratterizzazione è quindi di grande importanza al fine di meglio comprendere le dinamiche di questi sistemi. Lo studio evidenzia come pacchetti di vortici “hairpin", caratterizzati da una testa localizzata a monte e da code che protrudono a valle, si allineano nella direzione della corrente per formare le cosiddette “large-scale-motions" (LSM). Per angoli di inclinazione $\alpha < 70^\circ$ le LSM si allineano a loro volta tra di loro a formare le “very-large-scale motions" (VLSM). LSM e VLSM contribuiscono in maniera significativa all’energia cinetica e al trasferimento (turbolento) di quantità di moto in direzione verticale nelle regioni esterne dello strato limite catabatico.

Infine, questa tesi esamina le proprietà di drag di superfici composte da ghiaccio marino dell’Antartide, attraverso il metodo di simulazione ai grandi vortici (LES). Nello specifico, si considera uno strato limite totalmente sviluppato su di una superficie ottenuta attraverso misurazioni laser della banchisa in Antartide. Gli effetti dovuti alle grandi scale di scabrezza (quelle scale risolvibili attraverso la discretizzazione LES) sono risolti attraverso un “immersed boundary method" (IBM), mentre gli effetti dovuti alla scabrezza di sottogriglia sono inclusi attraverso un modello dinamico di scabrezza (DSR) recentemente proposto. Il modello DSR permette di calcolare la scala idrodinamica della scabrezza assumendo che il trasferimento totale di quantità di moto in direzione verticale sia lo stesso alla scala di griglia e ad una scala test. Questo approccio permette di ottenere un’accurata ricostruzione del profilo di velocità, indipendentemente dalla risoluzione numerica utilizzata, ed il valore del parametro di scabrezza per la data superficie. Da quest’ultimo, è possibile derivare la scala idrodinamica di scabrezza per l’uso in modelli climatici, in modelli per le previsioni meteorologiche e per lo studio di trasporto su strati limite.

Parole chiave: budget di energia, flussi anabatici, flussi catabatici, immersed boundary method, modello di Prandtl, modello dinamico di scabrezza, simulazione ai grandi vortici, simulazione numerica diretta, superficie scabra, turbolenza.

Contents

Acknowledgements **i**

Abstract **iii**

List of figures **ix**

List of tables **xv**

1 Introduction **1**

2 On the solution of katabatic flows with spatially varying eddy viscosity and diffusivity **11**

2.1 Introduction 11
2.2 Specification of $\hat{K}(\hat{z})$ 14
2.3 The Analytic Solution 15
2.4 Examples 16
2.5 On the computation of the solution 19
2.6 Conclusions 21

3 Direct numerical simulation of slope flows: characterization of mean flow and turbulence **27**

3.1 Introduction 28
3.2 Equations of motion 30
  3.2.1 Normalisation of the equations and governing parameters 31
3.3 Simulations 32
3.4 Time evolution and structure of the flow 34
3.5 Mean flow and turbulence characteristics 38
  3.5.1 Mean flow 38
  3.5.2 TKE and buoyancy variance 41
  3.5.3 Momentum and buoyancy fluxes 43
3.6 Budgets of mean and turbulent kinetic energy 45
  3.6.1 The mean kinetic energy budget 45
  3.6.2 The turbulent kinetic energy budget 47
3.7 Summary and conclusions 52

4 Large and very-large-scale motions in katabatic flows over steep slopes 61

4.1 Introduction 61

4.2 Governing equations and simulation details 63

4.3 Results and discussion 65

4.3.1 Mean flow and velocity fluctuations 65

4.3.2 Pre-multiplied power spectra, co-spectra and quadrant analysis 66

4.3.3 Two point correlation coefficients 71

4.3.4 Characterization of LSMs and VLSMs 74

4.4 Summary and conclusions 77

5 Large-eddy simulation of atmospheric boundary-layer flow over Antarctic sea-ice formations using a dynamic roughness model 83

5.1 Abstract 83

5.2 Introduction 83

5.3 Sea ice surface models and their processing for use in LES 87

5.4 Numerical algorithm and the Dynamic Roughness Model 89

5.4.1 The LES algorithm 89

5.4.2 The Immersed Boundary Method 91

5.4.3 The dynamic surface roughness model 92

5.5 Setup of simulations 94

5.6 Results and discussion 95

5.6.1 The DSR model 95

5.6.2 Velocity profiles 96

5.7 Summary and conclusions 98

6 Conclusions and Perspectives 109

List of Figures

2.1 Slope-aligned coordinate system. 12

2.2 Comparison of the proposed analytic solution (A1) against the constant-K (A2) and the WKB solution (A3). u is positive in the down-slope direction. The constant-K value is fixed to $K_{\mathrm{A2}} = \max(K_{\mathrm{A1}})/3$. Velocity profiles ($u$) are denoted with solid lines whereas buoyancy profiles (b) are denoted by dashed lines. Here $z_0 = 0.001$, $Pr = 1$ and $H = 12$. Assuming $\hat{N} = 10^{-2}$ (Hz), $\hat{\alpha} = 5°$ and $\hat{b}_s = -0.1$ ($\mathrm{m\,s^{-2}}$), the corresponding dimensional system, based on $u_* \equiv \hat{u}_* U^{-1}$ from the A1 solution, is characterised by $\hat{z}_0 = 0.08$ (m) and $\hat{u}_* = 0.18$ ($\mathrm{m\,s^{-1}}$), within the range of commonly observed atmospheric values. 17

2.3 Sensitivity of the normalised A1 (left) and A3 (right) solutions to the z_0 parameter. Solid lines denote down-slope velocity (u) whereas dashed lines denote buoyancy (b). Fixed parameters: $H = 12$, $Pr = 1$. 18

2.4 Sensitivity of the normalised A1 (left) and A3 (right) solutions to the Pr parameter. Solid lines denote down-slope velocity (u) whereas dashed lines denote buoyancy (b). Displayed solutions correspond to: $H = 12$, $z_0 = 0.001$. 18

2.5 Left plot: Sensitivity of velocity u (solid lines) and buoyancy b (dashed lines) profiles on the H parameter. Right plot: convergence test, relative percentage error for z_j (red lines) and $\max(u)$ (blue lines) as a function of N, where N represents the number of terms considered in the truncated ${}_2F_1$ series. Parameters for the H-sensitivity study (left plot): $H_1 = 11.2$, $H_2 = 14$, $H_3 = 16.8$ and $z_0 = 0.001$. Parameters for the convergence test (right plot): $z_0 = 0.00001$ (squares), $z_0 = 0.0001$ (circles), $z_0 = 0.001$ (crosses) and $H = 14$. We define $e_{z_j} = 100(z_j^N - z_j)/z_j$ and $e_{\max(u)} = 100[\max(u^N) - \max(u)]/\max(u)$, where $(\cdot)^N$ represents a quantity computed truncating the ${}_2F_1$ series to N terms, and where z_j and $\max(u)$ represent quantities that are exact in double precision arithmetic. 20

3.1 Slope-aligned coordinate system. 30

3.2 Normalised Kolmogov's scale $\eta(z) = Re^{-3/4}\epsilon(z)^{-1/4}$ for anabatic (dashed lines) and katabatic (solid lines) cases, compared against the slope-normal stencil Δ_z. 34

3.3 Time evolution of slope-normal integrated $\langle u \rangle$ (solid lines) and $\langle b \rangle$ (dashed lines) fields for simulations A, B, C, and D (katabatic flow regime). The total time-integration period is shown for each run. 35

3.4 Dynamic (black lines) and thermodynamic (red lines) identities (equations 3.12 and 3.13) for the considered simulations. Profiles have been shifted on the y axis to allow for proper visualization. We here denote $\langle \tau_{xz}^{tot} \rangle = \frac{1}{Re}\frac{d^2\langle u \rangle}{dz^2} + \langle u' w' \rangle$ and $\langle \tau_{bz}^{tot} \rangle = \frac{1}{RePr}\frac{d^2\langle b \rangle}{dz^2} + \langle b' w' \rangle$ (sum of molecular and turbulent kinematic fluxes of stream-wise momentum and buoyancy in the slope-normal direction). 35

3.5 Color contours of instantaneous streamwise velocity u (top figures) and buoyancy b (bottom figures), on the plane $y = L_y/2$ for simulations A (left figures) and D (right figures). The displayed $u(x,z)$ and $b(x,z)$ fields correspond to the crest of the last simulated gravity-wave oscillation for both runs. For detailed viewing, only the near-surface region of the total domain is shown. 36

3.6 Color contours of instantaneous streamwise velocity u (top figures) and buoyancy b (bottom figures), on the plane $y = L_y/2$ for simulations G (left figures) and J (right figures). The displayed $u(x,z)$ and $b(x,z)$ fields correspond to the crest of the last simulated gravity-wave oscillation for both runs. For detailed viewing, only the near-surface region of the total domain is shown. 37

3.7 Comparison of stream-wise velocity $\langle u \rangle$ (left) and buoyancy $\langle b \rangle$ (right) for anabatic (dashed lines) and katabatic (solid lines) flow cases at $Re = 4.6 \times 10^5$. . . 38

3.8 Absolute value of the slope-normal integrated horizontal momentum flux (left) and absolute value of the mean surface buoyancy flux (right) as a function of α for the highest $Re = 4.6 \times 10^5$ case. 39

3.9 Sensitivity of the stream-wise velocity $\langle u \rangle$ (left) and buoyancy $\langle b \rangle$ (right) on the Re parameter, for katabatic (solid lines) and anabatic (dashed lines) flow regimes at $\alpha = 60^\circ$. 40

3.10 Absolute value of the averaged surface buoyancy flux as a function of Re for anabatic (red line) and katabatic (black line) flow regimes at $\alpha = 60^\circ$ (simulations B,E,F, and H,K,L respectively). 41

3.11 Comparison of turbulent kinetic energy ($1/2\langle u_i' u_i' \rangle$) (left) and buoyancy variance ($\langle b' b' \rangle$) (right) for the katabatic (solid lines) and the anabatic flow (dashed lines) regimes at the highest $Re = 4.6 \times 10^5$ cases. 42

3.12 Normal stress components $\langle u' u' \rangle$ (solid lines), $\langle v' v' \rangle$ (dashed lines) and $\langle w' w' \rangle$ (dot-dashed lines) for the katabatic (left) and the anabatic (right) flow regimes at the highest $Re = 4.6 \times 10^5$ cases. 42

3.13 Sensitivity of the turbulent kinetic energy ($(1/2)\langle u_i' u_i' \rangle$) (left) and buoyancy variance ($\langle b' b' \rangle$) (right) to the Re parameter for katabatic (solid lines) and anabatic (dashed lines) flow regimes at $\alpha = 60^\circ$. 43

3.14 Total (solid lines) and turbulent (dashed lines) momentum flux for the katabatic (top left) and the anabatic (top right) flow regimes, and total (solid lines) and turbulent (dashed lines) buoyancy slope-normal flux for the katabatic (bottom left) and the anabatic (bottom right) flow regimes. All cases are characterized by $Re = 4.6 \times 10^5$. We denote the total stream-wise momentum slope-normal flux as $\langle \tau_{xz}^{tot} \rangle \equiv (1/Re)(d\langle u \rangle/dz) + \langle u'w' \rangle$ and the total slope-normal buoyancy flux as $\langle \tau_{bz}^{tot} \rangle \equiv (1/(RePr))(d\langle b \rangle/dz) + \langle b'w' \rangle$. The height of the LLJ (z_j) is displayed (dotted line) for the different cases to provide a reference. 44

3.15 MKE budget for the katabatic (left) and the anabatic (right) flow regimes at $Re = 4.6 \times 10^5$. Profiles corresponding to $\alpha = 90°, 60°, 30°$ and $15°$ (simulations A, B, C, D for the katabatic regime; G, H, I, J for the anabatic regime) are denoted with solid, dashed, dot-dashed and dotted lines respectively. The location of the LLJ is highlighted with dotted black lines for the various runs, to provide a reference height (note that as α decreases the LLJ height increases, and note also that z_j is the same for the $\alpha = 90°$ and the $\alpha = 60°$ runs). All terms are normalized by $\hat{U}^3\,\hat{L}^{-1} \equiv \hat{b_s}^2\,\hat{N}^{-1}$. 46

3.16 Comparison of TKE budged terms for katabatic (left) and anabatic (right) flow regimes at $Re = 4.6 \times 10^5$. Production and destruction terms (top) have been separated from transport and residual terms (bottom). The $\alpha = 90°, 60°, 30°$ and $15°$ cases (simulations A, B, C, D for the katabatic regime; G, H, I, J for the anabatic regime) are denoted with solid, dashed, dot-dashed and dotted lines respectively. The location of the LLJ is highlighted with dotted black lines for the various runs to facilitate interpretation (note that $\alpha \propto z_j$). All terms are normalized by $\hat{U}^3\hat{L}^{-1} \equiv \hat{b}_s^2\hat{N}^{-1}$. 48

3.17 Comparison of return-to-isotropy terms for katabatic (left) and anabatic (right) flow regimes. We denote $\Phi_1 \equiv \langle p' \frac{\partial u'}{\partial x} \rangle$, $\Phi_2 \equiv \langle p' \frac{\partial v'}{\partial y} \rangle$, and $\Phi_3 \equiv \langle p' \frac{\partial w'}{\partial z} \rangle$. The location of the LLJ is once again highlighted with dotted grey lines and the $\alpha = 90°, 60°, 30°$ and $15°$ runs (simulations A, B, C, D for the katabatic regime; G, H, I, J for the anabatic regime) are denoted with solid, dashed, dot-dashed and dotted lines respectively. All terms are normalized by $\hat{U}^3\,\hat{L}^{-1} \equiv \hat{b}_s^2\,\hat{N}^{-1}$. . . . 49

3.18 Sensitivity of MKE budget terms to Re for the katabatic (left) and the anabatic (right) flow regimes at $\alpha = 60°$. Profiles corresponding to $Re = 3.0 \times 10^5, 4 \times 10^5$, and 4.6×10^5 (simulations B,E,F for the katabatic flow regime, and H,K,L for the anabatic flow regime) are denoted with dot-dashed, dashed, and solid lines respectively. The location of the LLJ is highlighted with dotted black lines for the various runs, to provide a reference height (note that as Re increases the LLJ height decreases). All terms are normalized by $\hat{U}^3\,\hat{L}^{-1} \equiv \hat{b_s}^2\,\hat{N}^{-1}$. 50

3.19 Sensitivity of TKE budget terms to Re for the katabatic (left) and the anabatic (right) flow regimes at $\alpha = 60°$. Profiles corresponding to $Re = 3.0 \times 10^5, 4 \times 10^5$, and 4.6×10^5 (simulations F,E,B for the katabatic flow regime, and L,K,H for the anabatic flow regime) are denoted with dot-dashed, dashed, and solid lines respectively. The location of the LLJ is highlighted with dotted black lines for the various runs, to provide a reference height (note that as Re increases the LLJ height decreases). All terms are normalized by $\hat{U}^3\,\hat{L}^{-1} \equiv \hat{b_s}^2\,\hat{N}^{-1}$. 51

4.1 Time and space averaged along-slope normalized velocity $\langle u \rangle$ (left) and Reynolds stress $\langle u'w' \rangle$ (right). 65

4.2 Fluctuations of the normalized streamwise velocity in the horizontal plane at $z = 8.2$. The flow is from left to right. A smaller portion of the computational domain is shown for each case. 67

4.3 Pre-multiplied power spectra as functions of streamwise wavelength for the streamwise velocity u. 68

4.4 Pre-multiplied co-spectra of the streamwise and normal-to-slope velocity components as functions of streamwise wavelength for the case D ($\alpha = 60°$). 69

4.5 Quadrants for the $u'w'$ momentum flux for the case D ($\alpha = 60°$). From top left to bottom right plots correspond to an increasing distance from the wall ($z = 1.4, 8.2, 16.5$ and 26 respectively). 70

4.6 Streamwise (left) and spanwise (right) two-point correlation coefficients of the streamwise velocity ($R_{uu}(\Delta x, 0, z)$ and $R_{uu}(0, \Delta y, z)$) calculated at different distances from the wall for the case D. 72

4.7 Iso-surfaces of R^{3d}_{uu} with $z_r = 16$. Red iso-surfaces show positive correlation ($R^{3d}_{uu} = 0.1$), whereas blue iso-surfaces show negative correlation ($R^{3d}_{uu} = -0.1$). . 73

4.8 Visualization of the vortex distribution detected by the Q-criterion. The $Q = 0.05Q_{max}$ iso-surfaces are colored by u'. 73

4.9 Vector plot of the instantaneous velocity field over a $x - z$ plane intersecting a high-momentum region, colored by the instantaneous velocity fluctuation with respect to the instantaneous planar average value $u'' = u - \langle u \rangle$. 74

4.10 Schematic of a katabatic flow hairpin vortex and the induced motion. Adapted from Adrian et al. (2000). 75

4.11 Conditionally-averaged flow field, where the conditional event is a high-speed event (of positive u fluctuation) at $(x, y, z) = (0, 0, 16)$. An Iso-surface of positive u fluctuation ($u' = 0.0039$) is displayed in red, flanked by iso-surfaces of negative u fluctuation ($u' = -0.0031$). An inset providing a zoom on the velocity-vector map in the $y - z$ plane is also shown. 76

5.1 Resulting surface from aggregation of the point cloud dataset at 1 cm resolution over a 100m × 100m area. Gaps are indicated by white areas. 87

5.2 One dimensional power spectral densities of surface heights in the x and y coordinate directions. The LES grid size is highlighted with arrows, for the two resolutions that were here considered. N denotes the number of grid nodes in the horizontal directions. 88
5.3 Sea ice surface statistics as a function of the LES filter support (or grid stencil). s_k denotes the skewness of surface heights, σ_h^Δ denotes the r.m.s of the subgrid-scale surface heights. 89
5.4 One-dimensional transect at $y = 10\,\mathrm{m}$ of the scanned sea ice surface, and equivalent transect on a filtered version of the sea ice surface (filter support $\Delta = 6.3\,\mathrm{m}$). The displayed transects have been vertically translated so that their average height equals zero. 91
5.5 Rendering of the periodic sea ice 100m × 100m filtered surfaces (top hat filter). Filter support is $\Delta = 1.56\,\mathrm{m}$ (a), $\Delta = 0.78\,\mathrm{m}$ (b), $\Delta = 0.39\,\mathrm{m}$ (c) and $\Delta = 0.195\,\mathrm{m}$ (d) in the x, y coordinate directions. 94
5.6 Instantaneous (dimensional) stream-wise u velocity over the filtered sea ice surface for case A. The realization corresponds to the last simulated time step. . 95
5.7 Resolved, SGS and total (resolved+SGS) surface stress as a function of the surface roughness parameter α. Curves are representative of the last α-update step. Results are shown for both grid-filter scale (Δ) (black lines) and test-filter scale (2Δ) (red lines). Symbols: solid black lines, $\langle \tau_{xz}^{\Delta} \rangle_{\tilde{\Gamma}_\mathrm{b}} + \langle \tilde{p}_i \tilde{n}_i \rangle_{\tilde{\Gamma}_\mathrm{b}}$; dashed black lines, $\langle \tau_{xz}^{\Delta} \rangle_{\tilde{\Gamma}_\mathrm{b}}$; black crosses, $\langle \tilde{p}_i \tilde{n}_i \rangle_{\tilde{\Gamma}_\mathrm{b}}$, solid red lines, $\langle \tau_{xz}^{2\Delta} \rangle_{\bar{\tilde{\Gamma}}_\mathrm{b}} + \langle \bar{\tilde{p}}_i \bar{\tilde{n}}_i \rangle_{\bar{\tilde{\Gamma}}_\mathrm{b}}$; dashed red lines, $\langle \tau_{xz}^{2\Delta} \rangle_{\bar{\tilde{\Gamma}}_\mathrm{b}}$; red crosses, $\langle \bar{\tilde{p}}_i \bar{\tilde{n}}_i \rangle_{\bar{\tilde{\Gamma}}_\mathrm{b}}$. 96
5.8 Time evolution of the roughness parameter α (top) and corresponding values of spatially averaged kinematic surface stress components (bottom) for case A. Symbols: black squares, $\langle \tau_{xz}^{\Delta} \rangle_{\tilde{\Gamma}_\mathrm{b}}$; red squares, $\langle \tau_{xz}^{2\Delta} \rangle_{\bar{\tilde{\Gamma}}_\mathrm{b}}$; black crosses, $\langle \tilde{p}_i \tilde{n}_i \rangle_{\tilde{\Gamma}_\mathrm{b}}$; red crosses, $\langle \bar{\tilde{p}}_i \bar{\tilde{n}}_i \rangle_{\bar{\tilde{\Gamma}}_\mathrm{b}}$. α is updated every 10 LES time steps, thus the displayed plot accounts for the first 3000 simulation steps after the DSR model has been activated (corresponding to 0.75% of the total simulation time). 97
5.9 Averaged stream-wise velocity profile for cases A,B (left) and C,D (right). 97

List of Tables

3.1 Geometry and parameters for the DNS runs. L_i denotes the domain size in the three coordinate directions, N_i denotes the number of collocation nodes adopted in the three coordinate directions, T denotes the characteristic oscillation period of internal waves characterizing the system (see Sect. 3.4), $Re = \hat{b}_s^2\,\hat{\nu}^{-1}\,\hat{N}^{-3}$ and b_s is the imposed (normalized) surface buoyancy. Simulations $A-F$ correspond to $b_s=-1$, whereas cases $G-L$ correspond to $b_s=+1$. 33

4.1 Geometry and parameters for the DNS runs. 64

5.1 Geometry and parameters for the LES runs. 94

1 Introduction

Turbulence – the main agent governing exchange processes in the land-atmosphere system – remains one of the greatest unsolved problems of physics (Stull, 1988; Carlson et al., 2006). A correct modeling of turbulence in the atmospheric boundary layer (ABL), the atmospheric layer in direct contact with Earth's surface, is of fundamental importance in order to accurately quantify exchange of energy and mass between the Earth and the atmosphere. Exchange processes between the atmosphere and the underlying surface have a direct impact on weather and climate variability, thus affecting humans health, water resource management, and ecological and hydrological processes. It is therefore no surprise that land-atmosphere interaction has been the focus of active, multi-disciplinary research in the past decades, as reflected by the significant number of works published on the subject. Unfortunately, the multi-scale nature of the ABL, coupled with the inherent complexity of the Earth's surface, results in an extremely challenging problem to address, and current knowledge lags behind actual needs (Stensrud, 2007; Fernando, 2010; Katul et al., 2012).

Given the difficulties of solving ABL problems from first principles, the method of similarity theory has represented a valuable analysis tool. A cornerstone in the understanding of the ABL is represented by the Monin-Obukhov similarity theory (MOST) (Monin and Obukhov, 1954), a generalization of Prandtl mixing length model (Prandtl, 1925; Tietjens and Prandtl, 1957), to account for effects induced by stratification. MOST expresses scaled variables as universal functions (to be inferred from experiments) of the dimensionless stability parameter zL^{-1}, where z is the height above the ground and L is the Obukhov length (see Monin and Obukhov (1954); Brutsaert (1982)). In theory, the applicability of MOST is restricted to the inertial sublayer (i.e. the overlap region) of ABL flows over flat and homogeneous terrain, under statistically steady atmospheric conditions, and where Coriolis effects are negligible. In practice, MOST is known to perform relatively well even over complex terrain (Parlange et al., 1995; Andreas et al., 1998; de Franceschi et al., 2009). Such robustness makes it the reference surface closure in numerical weather prediction and climate models (Stensrud, 2007). Nevertheless, alternative models perform better in some settings, and MOST breaks down in others. In strongly unstable regimes, for instance, free convective scaling is preferable (Albertson et al., 1995; Stull, 1988), whereas MOST becomes unreliable for the poorly understood, stably stratified ABL (Mahrt, 2013), for which no similarity theory is yet available. In addition, MOST requires the underlying flat surface to be homogeneous, whereas the Earth's surface is inherently complex. Surface complexity is commonly understood in a broad sense, and accounts for topographic variations, sloping terrain, and for heterogeneous forcing mechanisms (such as soil moisture or temperature), to name but a few. Over heterogeneous surfaces, for instance, the presence of internal boundary layers and of local advection leads to non-negligible flux-divergence, in which case MOST is not necessarily expected to apply (Higgins et al., 2013). Moreover, under stable stratification, the relative importance of surface heterogeneity and of local slopes is increased (Mahrt, 2013). Such complications have motivated a divide-and-conquer strategy, resulting in a host of idealized systems, each focusing on a specific type of land-atmosphere interaction process, based on the idea that one should first understand a problem in its simplest settings before introducing additional complexities and coupling. Furthermore, the land-atmosphere system is such that local features of the exchange processes can have a deep impact on weather and climate at larger scales (Lorenz, 1963). Accordingly, only a better understanding of the individual aspects of the problem will allow an accurate description of energy and mass balance at the Earth surface, which is fundamental to improve the predictive skills of numerical weather and climate models (Stensrud, 2007).

The thesis addresses two specific problems where MOST applicability is problematic: that of thermally-driven stratified flows, commonly arising over sloping surfaces (Chapters 2, 3 and 4), and that of ABL flow over multi-scale rough topographies, such as fluvial landscapes, ocean waves, snow and sea ice surfaces (Chapters 5). Given the ubiquity of such flows in nature, a better understanding of their dynamics will allow significant advances in ABL knowledge at larger scales and in coupled problems.

Slope flows arise under clear sky conditions and weak synoptic forcing. Daytime solar heating of the underlying sloping surfaces (e.g. mountain sides or valleys) causes positively buoyant air to rise upslope, triggering anabatic flows. At night, radiative cooling of the same surfaces results in negatively buoyant air close to the ground descending downslope, generating katabatic flows. Under weak synoptic forcing, anabatic and katabatic winds regulate the transport of scalars such as heat, humidity and pollutants in mountainous regions (Rotach and Zardi, 2007; Fernando, 2010). Katabatic winds are persistent over the ice sheets of Greenland and Antarctica (Egger, 1985; Parish, 1992; Parish and Bromwich, 1998; Renfrew, 2004; Renfrew, I. and Anderson, P., 2006) – affecting local weather and climate – and over melting glaciers (Greuell et al., 1994; Oerlemans, 1998) – whose constant retreat is a matter of public concern, given its impact on both the sea level rise and on water availability. Early studies of slope flows date back to Wagner (1938); Prandtl (1942) and Defant (1949), but current knowledge is still limited, reflecting the fundamental complexity of the phenomena. The geometrical setup of the problem complicates matters from a measurement perspective (Oldroyd et al., 2015), as exemplified by the scarcity of experimental data (Horst and Doran, 1986; Nadeau et al., 2013; Grachev et al., 2015). On the other hand, simulations are challenging due to the stable stratification and lack of a near-surface closure, also resulting in few available numerical studies (Schumann, 1990; Skyllingstad, 2003; Axelsen and Dop, 2009b; Fedorovich and Shapiro, 2009a,b; Shapiro and Fedorovich, 2014). Analytical solutions, numerical studies, and observations have shown that the structure of slope winds is further complicated, as compared to classical boundary layer profiles, by the formation of a so-called low-level jet in the near wall regions and by the presence of several zero-gradient layers in the state variables, manifestation of additional dynamics induced by the interplay of stable stratification, turbulence, and the underlying sloping surface (Prandtl, 1942; Fedorovich and Shapiro, 2009b; Grachev et al., 2015). Hence MOST is likely to fail, if used to approximate the entire boundary layer in slope flows, and a near-surface closure theory most likely needs to be developed from the equations of motion, since there is little hope of finding these solutions by the method of similarity hypothesis.

In Chapters 2,3 and 4, a combination of analytical and numerical approaches are adopted to address these problems. An analytical solution of the one-dimensional Prandtl model equations is derived in Chapter 2, where turbulence effects are modeled within the framework of the K-theory. Analytical solutions of linearized versions of the problem are of great interest, given their potential to be integrated in large-scale models as surface closure, or for the extrapolation of surface fluxes in applications with sensor networks. In Chapter 3, direct numerical simulation (DNS) is used to unravel the turbulent structure of slope flows. The aim of the study is to clarify the dependence of anabatic and katabatic solutions on the model parameters and to examine the budget terms of mean and turbulent kinetic energy balances, which are of great interest from a parameterization perspective. Chapter 4 bridges the gap between the relatively broad knowledge on coherent structures populating canonical wall-bounded flows, and the lack of information on the structure of energy-containing turbulent motions in slope flows. Coherent motions are responsible for maintaining (production and dissipation) turbulence, hence their study is essential for the understanding of boundary-layer dynamics.

The last chapter of the thesis addresses the problem of ABL flows over multi-scale rough topographies, where the applicability of MOST is also known to be problematic. Typical examples of multi-scale surfaces include fluvial landscapes (Rinaldo et al., 1993; Rodriguez-Iturbe et al., 1994), ocean waves (Yang et al., 2013), plant canopies (Finnigan, 2000; Yue et al., 2007; Böhm et al., 2013) and sea ice surfaces (Trujillo et al., 2016). Such topographies display scale-invariance over a broad range of wavelengths, that is, the spectrum of surface heights is characterized by a power-law behavior. In Chapter 5, the specific focus is on Antarctic sea ice surfaces, whose contribution in terms of energy, momentum and mass exchange is key to the understanding of the climate system as a whole (e.g. Papritz et al. (2015)). Roughness properties of snow surfaces are subjected to rapid changes over the ice field, thus a correct representation of momentum transfer is required not only to estimate large-scale ice drift and total ice mass balance (Zhang, 2014), but also to correctly represent erosion and deposition of snow in these heavily wind-blown environments (Groot Zwaaftink et al., 2014). Accurate prediction of mass and momentum exchange on ABL flows over rough surfaces is possible only if the flow in the interfacial layer – the layer bounded by the height of the roughness elements – is correctly represented, hence surface features need to be adequately resolved. Despite the significant advances in computational performance in recent years, the tremendous range of length scales present in sea ice landscapes and the high Reynolds number of the flow prevent DNS from being used for the problem at hand. This has motivated the adoption of closure models designed to reduce resolution requirements in the dissipative range, especially where energy-containing scales are of primary interest (Pope, 2000). Large-eddy simulation (LES) represents a valid alternative to DNS, but the filtering operation (which is implicitly understood in LES) also applies to the underlying surface, thus introducing an additional subgrid-scale (SGS) roughness modeling requirement. This is no trivial task, given the lack of knowledge on turbulent flows in the interfacial layer, and considering that the drag contributions of small scales in natural fractal-like surfaces usually account for a significant percentage of the total (Anderson and Meneveau, 2011; Anderson et al., 2012). This problem is addressed in Chapter 5, where roughness properties of sea ice Antarctic surfaces are studied. In the specific, a recently developed dynamic surface roughness model (DSR) (Anderson and Meneveau, 2011) is adapted for use in conjunction with the immersed boundary method (IBM) and with LES. The effects of large-scale surface features on wind flow are accounted for through the IBM approach, whereas drag forces caused by SGS surface features are accounted for via the DSR model. The DSR model allows to estimate the (otherwise unknown) z_0 parameter, representative of SGS roughness features of sea ice surfaces, based on the first principle constraint that total drag is invariant at grid- and test-filter scales. It thus represents a major step forward in the simulation of flow over multi-scale rough surfaces, opening the doors for a new avenue of research in the field.

In summary, the dissertation is organized around two complex surface environments, each treating a separate problem within the broad realm of flows over complex terrain, as follows. Part I is devoted to the analysis of turbulent slope flows, within the conceptual framework of the Prandtl model.

- In **Chapter 2**, a closed form analytic solution is derived of the steady-state Prandtl model equations, valid for spatially varying eddy diffusivities (O'Briens type) and Prandtl number of unity. The original contributions to this chapter are the derivation of the analytical solution itself, its analysis in terms of sensitivity to model parameters, and its critical comparison against previous analytic solutions.
- **Chapter 3** employs DNS to characterize the turbulent structure of slope flows within the Prandtl model framework, and to determine the sensitivity of the solution to variations in the parameter space. The aim is to better understand the effects of turbulence on the system, which is key to the development of reliable parameterizations for LES and lower dimensional models. The original contributions of the chapter are the implementation of the Prandtl slope flow equations in a parallelized (hybrid openMP / MPI) pseudo-spectral DNS algorithm, and a critical statistical analysis of the sloping angle dependence of several quantities, including integral constraints that the system

has to satisfy, mean kinetic energy (MKE) and turbulent kinetic energy (TKE) budget terms. Emphasis is put on the description of the mechanisms sustaining mean flow and turbulence in katabatic and anabatic flows, and in the comparison among the two flow regimes.

- **Chapter 4** provides additional insights into the turbulent structure of katabatic flows. A combination of statistical analysis and eduction criteria are adopted to identify and characterize coherent energetic motions in katabatic flows over steep slopes, within the DNS framework of Chapter 3. The original contributions in this chapter are the identification and characterization of large scale motions, from both a geometrical and energetic perspective. In addition, a katabatic flow hairpin model is proposed, to explain the formation mechanisms of LSMs and VLSMs.

Part II is devoted to general problem of drag characterization in flows over multi-scale fractal-like rough surfaces, with specific application to flow over sea ice floes.

- In **Chapter 5** a DSR model is adapted for use in conjunction with the IBM, and applied in LES to characterize surface roughness properties of multi-scale sea ice surfaces. The IBM method is used to represent the underlying, resolvable, surface roughness, whereas drag forces caused by subgrid-scale features are accounted for through the DSR model. The original contributions of this chapter are the implementation and validation of a DSR model, in conjunction with an IBM algorithm (adapted from a previously existing version), and the use of such a tool to investigate drag properties and to derive the α dimensionless roughness parameter for sea ice surfaces, of use in large scale models for the computation of the hydrodynamic roughness length.

Concluding remarks and perspectives on future developments of this work are briefly discussed in the final conclusion.

Bibliography

John D. Albertson, Marc B. Parlange, Gabriel G. Katul, Chia-Ren Chu, Han Stricker, and Scott Tyler. Sensible heat flux from arid regions: A simple flux-variance method. *Water Resour Res*, 31(4):969–973, 1995.

W. Anderson and C. Meneveau. Dynamic roughness model for large-eddy simulation of turbulent flow over multiscale, fractal-like rough surfaces. *J Fluid Mech*, 679:288–314, 2011.

W. Anderson, P. Passalacqua, F. Porté-Agel, and C. Meneveau. Large-eddy simulation of atmospheric boundary-layer flow over fluvial-like landscapes using a dynamic roughness model. *Boundary-Layer Meteorol*, 144(2):263–286, 2012.

E L Andreas, R J Hill, J R Gosz, D I Moore, W D Otto, and A D Sarma. Statistics of surface-layer turbulence over terrain with metre-scale heterogeneity. *Boundary-Layer Meteorol*, 86(3): 379–408, 1998.

S. L. Axelsen and H. Dop. Large-eddy simulation of katabatic winds. Part 2: Sensitivity study and comparison with analytical models. *Acta Geophys*, 57(4):837–856, 2009.

M. Böhm, J. J. Finnigan, M. R. Raupach, and D. Hughes. Turbulence structure within and above a canopy of bluff elements. *Boundary-Layer Meteorol*, 146(3):393–419, 2013.

W. Brutsaert. *Evaporation into the Atmosphere*. Springer Netherlands, Dordrecht, 1982.

J. Carlson, A. Jaffe, and A. Wiles. The millennium prize problems. *Centre Belge de Recherches Mathematiques*, 2006.

M. de Franceschi, D. Zardi, M. Tagliazucca, and F. Tampieri. Analysis of second-order moments in surface layer turbulence in an Alpine valley. *Q J R Meteorol Soc*, 135(644):1750–1765, 2009.

F. Defant. Zur theorie der hangwinde, nebst bemerkungen zur theorie der berg- und talwinde. *Archiv für Meteorologie, Geophysik und Bioklimatologie Serie A*, 1:421–450, 1949.

J. Egger. Slope winds and the axisymmetric circulation over Antarctica. *J Atmos Sci*, 42(17): 1859–1867, 1985.

E. Fedorovich and A. Shapiro. Turbulent natural convection along a vertical plate immersed in a stably stratified fluid. *J Fluid Mech*, 636:41–57, 2009a.

E. Fedorovich and A. Shapiro. Structure of numerically simulated katabatic and anabatic flows along steep slopes. *Acta Geophys*, 57(4):981–1010, 2009b.

H. J. S. Fernando. Fluid dynamics of urban atmospheres in complex terrain. *Annu Rev Fluid Mech*, 42(1):365–389, 2010.

J. Finnigan. Turbulence in plant canopies. *Annu Rev Fluid Mech*, 32(1):519–571, 2000.

A. A. Grachev, L. S. Leo, S. D. Sabatino, H. J. S. Fernando, E. R. Pardyjak, and C. W. Fairall. Structure of turbulence in katabatic flows below and above the wind-speed maximum. *Boundary-Layer Meteorol*, 2015.

J. W. Greuell, M. R. Broeke Van den, W. Knap, C. Reijmer, P. Smeets, , and I. Struijk. PASTEX: A glacio-meteorological experiment on the Pasterze (Austria). Technical report, Institute forMarine and Atmospheric Research, Utrecht University, Utrecht, 1994.

C. D. Groot Zwaaftink, M. Diebold, S. Horender, J. Overney, G. Lieberherr, M. B. Parlange, and M. Lehning. Modelling small-scale drifting snow with a Lagrangian stochastic model based on large-eddy simulations. *Boundary-Layer Meteorol*, 153(1):117–139, 2014.

C. W. Higgins, G. G. Katul, M. Froidevaux, V. Simeonov, and M. B. Parlange. Are atmospheric surface layer flows ergodic? *Geophys Res Lett*, 40(12):3342–3346, 2013.

T. W. Horst and J. C. Doran. Nocturnal drainage flow on simple slopes. *Boundary-Layer Meteorol*, 34(3):263–286, 1986.

G. G. Katul, R. Oren, S. Manzoni, C. Higgins, and M. B. Parlange. Evapotranspiration: A process driving mass transport and energy exchange in the soil-plant-atmosphere-climate system. *Rev Geophys*, 50(3):RG3002, 2012.

E. N. Lorenz. Deterministic nonperiodic flow. *J Atmos Sci*, 20:130–141, 1963.

L. Mahrt. Stably stratified atmospheric boundary layers. *Annu Rev Fluid Mech*, 46(July):23–45, 2013.

A. S. Monin and A. M. Obukhov. Basic laws of turbulent mixing in the surface layer of the atmosphere. *Contrib. Geophys. Inst. Acad. Sci. USSR*, 24(151):163–187, 1954.

D. F. Nadeau, E. R. Pardyjak, C. W. Higgins, and M. B. Parlange. Similarity scaling over a steep alpine slope. *Boundary-Layer Meteorol*, 147(3):401–419, 2013.

J. Oerlemans. The atmospheric boundary layer over melting glaciers. In *Clear and Cloudy Boundary Layers*, pages 129–153. Royal Netherlands Academy of Arts and Sciences, 1998.

H. J. Oldroyd, E. R. Pardyjak, H. Huwald, and M.B. Parlange. Adapting tilt corrections and the governing flow equations for steep, fully three-dimensional, mountainous terrain. *Boundary-Layer Meteorol*, pages 1–27, 2015.

L. Papritz, S. Pfahl, H. Sodemann, and H. Wernli. A climatology of cold air outbreaks and their impact on air–sea heat fluxes in the high-latitude south Pacific. *J Clim*, 28(1):342–364, 2015.

T. R. Parish and D. H. Bromwich. A case study of Antarctic katabatic wind interaction with large-scale forcing. *Mon Weather Rev*, 126(1):199–209, 1998.

Thomas R. Parish. On the role of Antarctic katabatic winds in forcing large-scale tropospheric motions. *J Atmos Sci*, 49(15):1374–1385, 1992.

M. B. Parlange, W. E. Eichinger, and J. D. Albertson. Regional scale evaporation and the atmospheric boundary layer. *Rev Geophys*, 33(1):99, 1995.

S. B. Pope. *Turbulent flows*. Cambridge University Press, 2000.

L. Prandtl. Bericht über untersuchungen zur ausgebildeten turbulenz. *Z. Angew. Math. Mech*, 5(2):136–139, 1925.

L. Prandtl. *Führer durch die strömungslehre*. Vieweg & Sohn, Braunschweig, 1942.

I. A. Renfrew. The dynamics of idealized katabatic flow over a moderate slope and ice shelf. *Q J R Meteorol Soc*, 130(598):1023–1045, 2004.

A. Renfrew, I. and S. Anderson, P. Profiles of katabatic flow in summer and winter over Coats Land, Antarctica. *Q J R Meteorol Soc*, 132(616):779–802, 2006.

A. Rinaldo, I. Rodriguez-Iturbe, R. Rigon, E. Ijjasz-Vasquez, and R. L. Bras. Self-organized fractal river networks. *Phys Rev Lett*, 70(6):822–825, 1993.

I. Rodriguez-Iturbe, M. Marani, R. Rigon, and A. Rinaldo. Self-organized river basin landscapes: Fractal and multifractal characteristics. *Water Resour Res*, 30(12):3531–3539, 1994.

M. W. Rotach and D. Zardi. On the boundary-layer structure over highly complex terrain: Key findings from MAP. *Q J R Meteorol Soc*, 133(625):937–948, 2007.

U. Schumann. Large-eddy simulation of the up-slope boundary layer. *Q J R Meteorol Soc*, 116 (493):637–670, 1990.

A. Shapiro and E. Fedorovich. A boundary-layer scaling for turbulent katabatic flow. *Boundary-Layer Meteorol*, 153(1):1–17, 2014.

E. D. Skyllingstad. Large-eddy simulation of katabatic flows. *Boundary-Layer Meteorol*, 106(2): 217–243, 2003.

D. J. Stensrud. *Parameterization schemes*. Cambridge University Press, Cambridge, 2007.

R. B. Stull. *An introduction to boundary layer meteorology*. Kluwer Academic Publishers, Dordrecht, 1988.

O. K. G. Tietjens and L. Prandtl. *Applied hydro-and aeromechanics: based on lectures of L. Prandtl*, volume 2. Courier Corporation, 1957.

E. Trujillo, K. Leonard, T. Maksym, and M. Lehning. Changes in snow distribution and surface topography following a snowstorm on Antarctic sea ice. *J Geophys R, Submitt*, 2016.

A. Wagner. Theorie und beobachtung der periodischen gebirgswinde (theory and observation of periodic mountain winds). *Gerl. Beitr. Geophys.*, (52):408–449, 1938.

D. Yang, C. Meneveau, and L. Shen. Dynamic modelling of sea-surface roughness for large-eddy simulation of wind over ocean wavefield. *J Fluid Mech*, 726:62–99, 2013.

W. Yue, M. B. Parlange, C. Meneveau, W. Zhu, R. Hout, and J. Katz. Large-eddy simulation of plant canopy flows using plant-scale representation. *Boundary-Layer Meteorol*, 124(2): 183–203, 2007.

J. Zhang. Modeling the impact of wind intensification on Antarctic sea ice volume. *J Clim*, 27 (1):202–214, 2014.

2 On the solution of katabatic flows with spatially varying eddy viscosity and diffusivity

Abstract

The Nieuwstadt closed form solution for the stationary Ekman-layer equations (Nieuwstadt, 1983) is here reconsidered and generalized to address the problem of katabatic flows within the conceptual framework of the Prandtl model. The solution is valid for spatially varying eddy viscosity and diffusivity (O'Briens type) and constant Prandtl number (Pr). Momentum and buoyancy transfer coefficients are here specified in accordance to Monin-Obukhov similarity theory (MOST). The characteristics of the solution are discussed as a function of the dimensionless model parameters Pr and $\hat{z}_0\hat{N}^2\hat{b}_s^{-1}$, where $\hat{z}_0$ is the hydrodynamic roughness length, $\hat{b}_s$ is the imposed surface buoyancy and $\hat{N}$ is the Brunt-Väisälä frequency. For the considered range of such parameters, velocity and buoyancy profiles show significant variations in both phase and amplitude of extrema with respect to the classic constant-K model and a more recent approximate solution, based on the Wentzel-Kramers-Brillouin (WKB) theory, hence shedding new light on the problem. Near-wall regions are characterised by relatively stronger surface momentum and buoyancy gradients, whose magnitude is inversely proportional to Pr. In addition, slope-parallel momentum and buoyancy fluxes are reduced, the low-level jet (LLJ) is further displaced toward the wall, and its peak velocity strongly depends on the $\hat{z}_0\hat{N}^2\hat{b}_s^{-1}$ parameter.

2.1 Introduction

Slope flows are of interest not only as a fundamental problem in itself, but also because of their important role in regulating local weather conditions in complex terrain, affecting atmospheric transport of momentum and of scalars such as heat and humidity (Whiteman, 1990, 2000; Monti et al., 2002; Nylen et al., 2004; Rotach and Zardi, 2007; Lehner et al., 2015). Katabatic flows are responsible for the formation of cold pools in confined valleys (Whiteman et al., 2001; Sheridan et al., 2014), which trap pollution and gases, thus affecting human health.

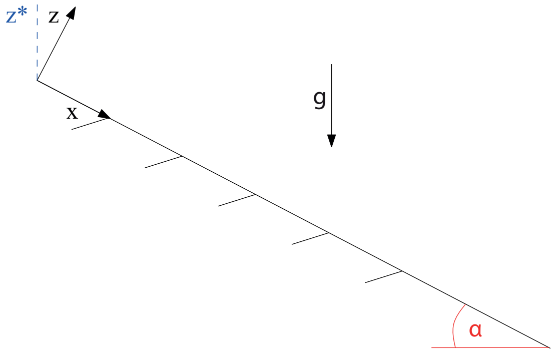

Figure 2.1 – Slope-aligned coordinate system.

Persistent katabatic winds also characterise the atmospheric boundary layer over Antarctica (Chu, 1987; Renfrew, 2004; Renfrew, I. and Anderson, P., 2006; Parish and Bromwich, 1991; Parish, 1992; Parish and Bromwich, 1998) and over glaciers (Oerlemans and Vugts, 1993; Oerlemans, 1994; Greuell et al., 1994; Oerlemans, 1998; Oerlemans and Grisogono, 2002), and therefore an accurate characterisation of such flows is essential to understand and model weather and climate. However, the complex dynamics (e.g. turbulent intermittency, waves, Kelvin-Helmholtz instabilities, low-level jets (LLJs)) and the lack of a satisfactory similarity theory for such flows (Nadeau et al., 2013) pose a heavy burden in terms of computational requirements for numerical modelers. In most cases the required resolution is in fact prohibitively costly (Fedorovich and Shapiro, 2009a,b; Burkholder et al., 2011). Because of this, conceptual models are still of great interest, and represent a valid tool for the characterisation of such systems.

A cornerstone in the understanding slope flows is represented by the classic Prandtl analytic model (Prandtl, 1942), and its recent extensions, to include the effects of Coriolis force (Gutman and Malbakhov, 1964), external winds (Lykosov and Gutman, 1972), and surface heterogeneity (Shapiro and Fedorovich, 2007; Oldroyd et al., 2014), to name but a few. The Prandtl model approximates the atmosphere in a Boussinesq sense and describes a steady flow over a thermally perturbed unbounded planar sloping surface, that lies within a stratified environment. The base stratification is assumed to be a function of the vertical coordinate direction $\hat{z}^*$, and the evolution of the system is described adopting a slope-aligned reference system $(\hat{x}, \hat{y}, \hat{z})$, as displayed in Fig. 2.1. Prandtl assumed a balance between along-slope buoyancy advection and slope-normal buoyancy diffusion, and between the downslope component of buoyancy and slope-normal momentum diffusion, resulting in the following system of ordinary differential equations:

$$-\hat{N}^2\,\hat{u}(\hat{z})\sin\alpha = [\hat{K}_H \hat{b}_{\hat{z}}]_{\hat{z}}\,, \tag{2.1a}$$

$$\hat{b}(\hat{z})\sin\alpha = [\hat{K}_M \hat{u}_{\hat{z}}]_{\hat{z}}\,, \tag{2.1b}$$

where $\hat{(\cdot)}$ is used to denote a dimensional variable or parameter, $\hat{z}$ denotes the normal-to-slope coordinate direction, $\hat{u}$ is the downslope velocity, $\hat{b} \equiv \hat{g}\hat{\theta}'/\hat{\theta}_0$ is buoyancy, where $\hat{g}$ is the gravitational acceleration, $\hat{\theta}'$ is the potential temperature perturbation and $\hat{\theta}_0$ is a reference (constant) temperature, $\hat{N}$ is the buoyancy frequency characterising the system (related to the background stratification), α is the slope angle and $\hat{K}_M$ and $\hat{K}_H$ denote the eddy viscosity and diffusivity (an eddy viscosity/diffusivity model has been used to parametrize turbulent fluxes of momentum and buoyancy). Equations are defined in $\hat{z} \in [\hat{z}_0, \infty)$ with boundary conditions $\hat{u}(\hat{z}_0) = 0$, $\hat{u}(\hat{z} \to \infty) = 0$, $\hat{b}(\hat{z}_0) = \hat{b}_s$ and $\hat{b}(\hat{z} \to \infty) = 0$ ($\hat{b}_s > 0$ for upslope flows, whereas $\hat{b}_s < 0$ for downslope flows). The flow is assumed to be invariant in the along-slope direction and the model can be used to determine the slope-normal ($\hat{z}$) structure of velocity $\hat{u}(\hat{z})$ and buoyancy $\hat{b}(\hat{z})$. The model thus applicable away from ridges and valleys, where non-linear advection terms become negligible (Nappo and Shankar, 1987), and when a steady balance between advection and diffusion (of both momentum and buoyancy) is achieved. Note that the latter constraint is rather restrictive, as shown in Shapiro and Fedorovich (2005) and in Zardi and Serafin (2015). The Prandtl constant-K solution reads

$$\hat{b} = \hat{b}_s \exp(-\hat{\sigma}_c \hat{z}) \cos(\hat{\sigma}_c \hat{z}), \tag{2.2a}$$

$$\hat{u} = -\frac{\hat{b}_s}{NPr} \exp(-\hat{\sigma}_c \hat{z}) \sin(\hat{\sigma}_c \hat{z}), \tag{2.2b}$$

where

$$\hat{\sigma}_c^2 \equiv \frac{\hat{\sigma_0}}{2\hat{K_H}}, \qquad \text{and} \qquad \hat{\sigma}_0 \equiv \frac{\hat{N}\sin(\alpha)}{\sqrt{Pr}}. \tag{2.3}$$

The model is able to represent the LLJ and the return flow region, key features of observed katabatic and anabatic flows. However, the constant-K solution is also known to be over-dissipative in the near-surface regions, and under dissipative above the LLJ regions (Defant, 1949; Oerlemans, 1998; Grisogono and Oerlemans, 2001). It is therefore not able to represent the observed strong surface gradients of temperature and momentum, and – in addition – the predicted wind speed typically decreases more rapidly than in reality. Simple variations in the eddy diffusivity profiles were introduced in a patched analytic solution by Gutman (1983), whereas more recently Grisogono and Oerlemans (2001) considered general variations in the vertical structure of the eddy diffusivities, and derived a patched global solution based on the WKB approximation (Bender and Orszag, 1979). The WKB solution to the Prandtl equations, valid to leading-order in the inner layer and to first-order in the outer layer, reads

$$\hat{f}_{in} \sim \exp\left(-(1 \pm i)(\hat{\sigma}_0/2)^{1/2} \int_0^{\hat{z}} \hat{K}(\hat{z})^{-1/2} \mathrm{d}z\right) \qquad \hat{z} \in [\hat{z}_0, \hat{h}], \tag{2.4a}$$

$$\hat{f}_{out} \sim [\hat{K}(\hat{z})/\hat{K}(\hat{h})]^{-1/4} \exp\left(-(1 \pm i)(\hat{\sigma}_0/2)^{1/2} \int_0^{\hat{z}} \hat{K}(\hat{z})^{-1/2} \mathrm{d}z\right) \qquad \hat{z} \in [\hat{h}, \infty), \tag{2.4b}$$

where $\hat{f}_{in} \equiv \hat{b}_{in} + i\,\hat{u}_{in}$ represents the inner-layer solution, and $\hat{f}_{out} \equiv \hat{b}_{out} + i\,\hat{u}_{out}$ is the outer-layer solution. $\hat{f}_{in}$ and $\hat{f}_{out}$ are patched at $\hat{z} = \hat{h}$, which separates the inner from the outer layer. The WKB solution is able to account for additional dynamics while still retaining an elegant form. However, WKB theory is only applicable when the model parameters ($\hat{K}_M, \hat{K}_H$) vary more slowly than the solution ($\hat{u}, \hat{b}$), and the validity of such a constraint for slope flows has been the subject of debate (Grisogono and Oerlemans, 2002).

Here, a closed-form solution to the Prandtl-model equations is derived on a finite domain ($\hat{z} \in [\hat{z}_0, \hat{H}]$), valid for eddy viscosity and diffusivity coefficients that are modeled as a limited range of cubic polynomials, similar to what proposed in O'Brien (1970) for the planetary boundary layer. The derivation is as a generalization of the solution proposed in Nieuwstadt (1983), where the Ekman-layer equations were solved for the same form of momentum transfer coefficient. Recall that the Ekman-layer equations can be reduced to the Prandtl equations after simple changes of variables, as shown in Shapiro and Fedorovich (2007). The solution, expressed as a combination of Gaussian hypergeometric functions, represents an exact alternative to the WKB formulation for the chosen form of the eddy diffusivities. Its sensitivity to variations in the parameter space are here investigated within the MOST framework, to gain insights on the coupling between the velocity and buoyancy fields.

2.2 Specification of $\hat{K}(\hat{z})$

Here, eddy diffusivities are prescribed in line with the classic O'Brien's model (O'Brien, 1970), viz.

$$\hat{K}(\hat{z}) = \kappa \hat{u}_* \hat{z}(1 - \hat{z}/\hat{H})^2 \qquad \hat{z} \in [\hat{z}_0, \hat{H}], \tag{2.5}$$

where κ is the Von Kármán constant, $\hat{u}_* = \kappa(\hat{z}\hat{u}_{\hat{z}})|_{\hat{z}_0}$ is the friction-velocity, and $\hat{H}$ is the height of the domain, controlling both shape and magnitude of $\hat{K}$. The O'Brien model complies with the $\hat{K}$-requirements defined in Grisogono and Oerlemans (2002), and has often been used in studies of stable boundary layers (see for instance Pielke (1984) and Stull (1988)). A generalized O'Brien model was also recently adopted in Grisogono and Oerlemans (2001) to study katabatic flows. In the original O'Brien's formulation $\hat{H}$ corresponds to the boundary layer depth; here $\hat{H} = 3\hat{h}$ is evaluated iteratively under the constraint $\hat{h} = \hat{z}_r$, where $\hat{z}_r$ is the height of the peak velocity magnitude in the return flow region. Such a choice for $\hat{h}$ is based on results from direct numerical simulation of katabatic flows over steep slopes, which are presented in Chapter 3.

Given the lack of a rigorous similarity theory for katabatic flows, this study is restricted to the MOST framework, which is expected to yield acceptable approximations of transfer coefficients in the near-surface regions (Gutman, 1983). MOST is not expected to hold in the above-jet regions, where eddy viscosity and diffusivity coefficients are likely to depend on an additional set of parameters such as the sloping angle (α), the Brunt-Väisälä frequency ($\hat{N}$), and the imposed surface buoyancy $\hat{b}_s$ (or buoyancy flux). Nevertheless, the proposed solution is valid in a more general sense, and could easily be adapted to a different $\hat{K}$-parameterisation. For instance, one could easily modify κ, to make it depend on the model parameters. Knowledge of $\hat{u}_*$ and $\hat{H}$ (or equivalently $\hat{h}$) allows to univocally specify $\hat{K}(\hat{z}) = \kappa \hat{u}_* \hat{z}(1 - \hat{z}/\hat{H})^2$.

2.3 The Analytic Solution

For the combination

$$\hat{f} = \hat{b} - (i\hat{N}\sqrt{Pr})\hat{u} \tag{2.6}$$

the system of Eqs. 2.1 is decoupled into a complex ordinary differential equation (ODE) for the canonical variable $\hat{f}$:

$$\hat{f} = \left[\frac{-i\hat{K}_M(\hat{z})}{\hat{N}\sin(\alpha)\sqrt{Pr}}\hat{f}_{\hat{z}}\right]_{\hat{z}} \qquad \hat{z} \in [\hat{z}_0, \hat{H}], \tag{2.7}$$

with boundary conditions $\hat{f}(\hat{z}_0) = \hat{b}_s$ and $\hat{f}(\hat{H}) = 0$. Assigning a length, velocity and buoyancy scale $\hat{L} = \hat{u}_*\kappa(\hat{N}\sin\alpha)^{-1}$, $\hat{U} = |\hat{b}_s|\hat{N}^{-1}$ and $\hat{B} = |\hat{b}_s|$ respectively, Eq. 2.7 reduces to:

$$f = \frac{-i}{\sqrt{Pr}}\left[K_M(z)f_z\right]_z \qquad z \in [z_0, H], \tag{2.8}$$

where $K_M(z) = z(1-z/H)^2$ is the normalised eddy viscosity, $z = \hat{z}\hat{L}^{-1}$, $f = \hat{b}\hat{B}^{-1} + (i\sqrt{Pr})\hat{u}\hat{U}^{-1}$, $H = \hat{H}\hat{L}^{-1}$ and $z_0 = \hat{z}_0\hat{L}^{-1}$, with boundary conditions $f(z_0) = -1$, $f(H) = 0$. The canonical form of Eq. 2.7 reads:

$$f_{zz} + Pf_z + Qf = 0, \tag{2.9}$$

where $P(z) = K_z/K$ and $Q(z) = (-i\sqrt{Pr})/K$. Second, it is an easy computation to show that rewriting Eq. 2.9 for $y = \frac{z}{H}$ results in

$$f_{yy} + \widetilde{P}f_y + \widetilde{Q}f = 0, \tag{2.10}$$

where $\widetilde{P}(y) = \gamma_y(y)/\gamma(y)$ and $\widetilde{Q}(y) = (-i\sqrt{Pr}H)/\gamma(y)$, with $\gamma(y) = y(y-1)^2$. Eq. 2.10 is a second order ODE with three regular singular points at $y = 0, 1$ and ∞, as in Morse and Feshbach (1953). This special case is known as the *equation of Papperitz* and its general solution is:

$$f(y) = \alpha(1-y)^{\mu}\,{}_2F_1(\mu, 1-\mu', 1+\mu-\mu', 1-y) + \beta(1-y)^{\mu'}\,{}_2F_1(\mu', 1-\mu, 1+\mu'-\mu, 1-y), \tag{2.11}$$

where ${}_2F_1$ are *Gaussian hypergeometric functions* and μ, μ' are the solutions to the degree two equation

$$x^2 + x - iH\sqrt{Pr} = 0.$$

Upon back-substitution of the independent variable and specification of the integration constants α and β (through the imposition of boundary conditions), the solution in terms of u and b is derived by separating the real and imaginary part of f

$$u(z) = -\frac{\mathrm{Im}(f(z))}{\sqrt{Pr}}, \qquad b(z) = \mathrm{Re}(f(z)). \tag{2.12}$$

As stated in the introduction, the proposed derivation closely resembles that in Nieuwstadt (1983), where the Ekman-layer equations have been solved in closed form for the same eddy viscosity coefficient. Here, the solution is specified for the Prandtl model equations, and generalised to account for arbitrary (constant) Pr. In addition, the proposed solution considers a finite z_0, as opposite to that in Nieuwstadt (1983) (where the simplifying assumption $z_0 = 0$ was adopted). A finite z_0 (hence finite $K_M(z_0)$ and $K_H(z_0)$) is required when solving the Prandtl slope flow model, which would otherwise yield unphysical velocity and buoyancy profiles. Despite the restrictive form of $K(z)$, which might limit the range of applicability of the model, the formulation allows for exact integration of Eqs. 2.1, hence providing a reference to study the dependence of the flow on the dimensionless model parameters Pr and $z_0 \equiv \hat{z}_0 \hat{N}^2 \hat{b}_s^{-1}$. It also represents a useful reference for the validation of numerical and patched/matched solutions.

2.4 Examples

In Fig. 2.2 we compare the proposed analytic solution (A1) against the constant-K (A2) and the WKB solution (A3), considering $Pr = 1$ (i.e., $\hat{K}_M = \hat{K}_H$). The constant-K solution is evaluated based on Eqs. 2.2, whereas the WKB solution is evaluated based on Eqs. 2.4. For the sake of comparison, A1 and A3 are evaluated for the same z_0 and H (hence same $K(z)$) parameters, whereas A2 is computed imposing $K_{A2} = \max(K)/3$. $\hat{h}$ is evaluated iteratively in order to match z_r of the A1 solution. Given that the resulting A1 solution is relatively insensitive to the exact $\hat{h}$ (in the neighborhood of the $\hat{h} = \hat{z}_r$ value) only a few iterations are sufficient to provide a good approximation of the desired $\hat{K}$. The chosen $K(z)$ satisfies the constraints defined in Grisogono and Oerlemans (2002) for the validity of the WKB method. A1 is indistinguishable to a corresponding second-order centered finite-difference numerical solution (also exact in double precision arithmetics), therefore the comparison is omitted. A1 shows a remarkably strong inversion in the near surface regions, when compared against its analytical counterparts, suggesting an over-diffusive behavior of both A2 and A3. For instance, normalised surface buoyancy gradients of simulation A1 are over an order of magnitude larger than those of A3 ($b_z^{\mathrm{A1}}/b_z^{\mathrm{A3}} = \mathcal{O}(10)$ for $z \to z_0$). Nevertheless, $u_z^{\mathrm{A1}} \approx u_z^{\mathrm{A3}}$ for $z \to z_0$, confirming the better dissipative properties of A3, when compared against the constant-K approach. To underline the importance of a decreasing magnitude of eddy diffusivities as the surface is approached, it is worth noting that $u_z^{\mathrm{A1}}/u_z^{\mathrm{A2}} = \mathcal{O}(10)$. Overall, the proposed normalised solution differ significantly when compared against A2 and A3, in both amplitude and location of extrema. Both the height of the LLJ and the peak velocity are significantly reduced, features

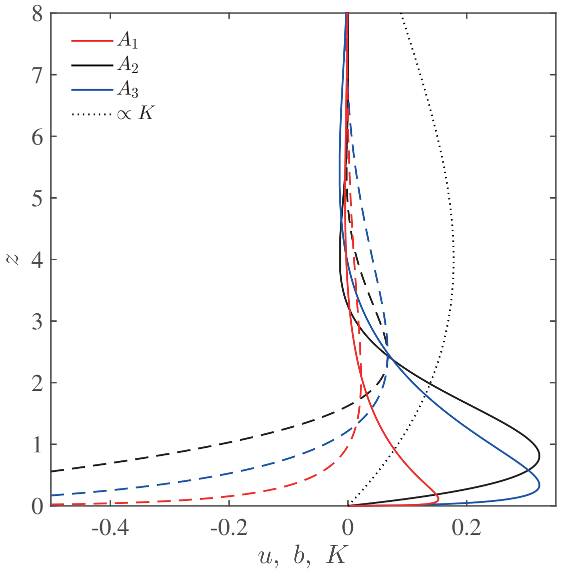

Figure 2.2 – Comparison of the proposed analytic solution (A1) against the constant-K (A2) and the WKB solution (A3). u is positive in the down-slope direction. The constant-K value is fixed to $K_{\mathrm{A2}} = \max(K_{\mathrm{A1}})/3$. Velocity profiles (u) are denoted with solid lines whereas buoyancy profiles (b) are denoted by dashed lines. Here $z_0 = 0.001$, $Pr = 1$ and $H = 12$. Assuming $\hat{N} = 10^{-2}$ (Hz), $\hat{\alpha} = 5°$ and $\hat{b}_s = -0.1$ $(\mathrm{m\,s^{-2}})$, the corresponding dimensional system, based on $u_* \equiv \hat{u}_* U^{-1}$ from the A1 solution, is characterised by $\hat{z}_0 = 0.08$ (m) and $\hat{u}_* = 0.18$ $(\mathrm{m\,s^{-1}})$, within the range of commonly observed atmospheric values.

that are of great importance for an accurate representation of the stable boundary layer and from a parameterisation perspective (Mahrt, 1998). Besides, A1 predicts significantly reduced mass and buoyancy (slope-parallel) fluxes, viz. $\int_0^H u\,\mathrm{d}z$ and $\int_0^H b\,\mathrm{d}z$, with respect to A2 and A3.

The sensitivity of the solution to variations in the z_0 parameter is displayed in Fig. 2.3. Since $(u_*, b_*) \propto z_0$, where $b_* \equiv \kappa z b_z$, larger hydrodynamic roughness lengths (z_0) correspond to stronger transfer rates of momentum and buoyancy in the vertical direction, yielding a larger z_j and $\max(u)$. To highlight differences with respect to the WKB solution, the same z_0 sensitivity test is displayed for the A3 solution in Fig. 2.3. Because $K \approx z$ in the neighborhood of $z = z_0$, A3 predicts $z_j \approx \pi^2/32 + z_0$ and $\max(u) = 0.32$. A3 is therefore able to describe the z_0 (alias K) dependency of z_j, but predicts a K-invariant $\max(u)$, as clear from Fig. 2.3. A2 is also characterised by a K-invariant $\max(u)$. The proposed solution therefore provides additional insights on the physics of the system, suggesting a somewhat different coupling between the velocity and buoyancy fields, when compared to that predicted by previous analytic solutions of the linear Prandtl model. It shows that positive variations of the z_0 parameter result in a higher and stronger LLJ $([z_j, \max(u)] \propto z_0)$. Further, since $\hat{L} = \kappa \hat{u}_*/(\hat{N}\sin\alpha)$, the characteristic scale of the flow $(\hat{L})$ will vary proportionally to z_0 for a prescribed $\hat{U}, \hat{B}, \alpha$ set.

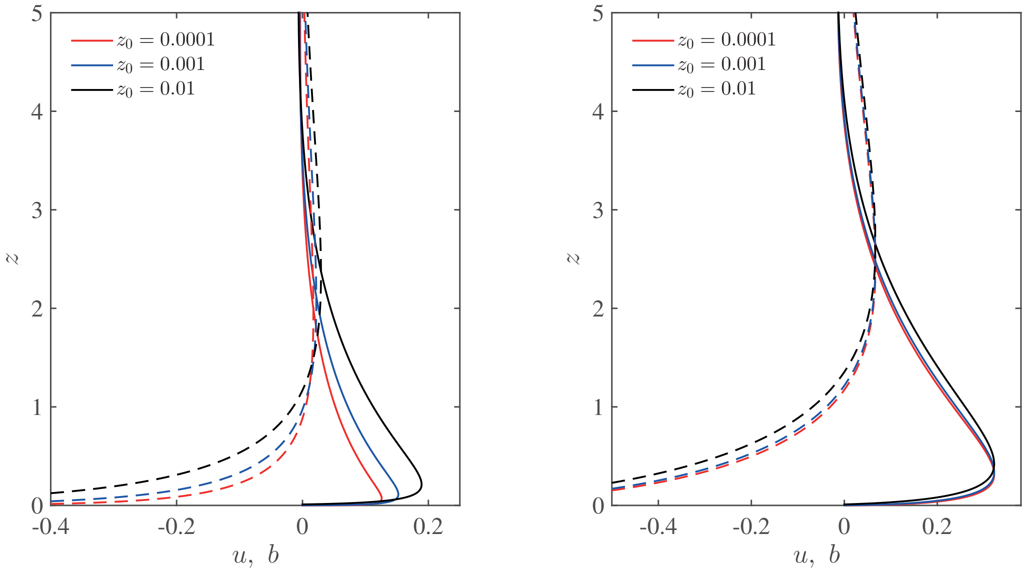

Figure 2.3 – Sensitivity of the normalised A1 (left) and A3 (right) solutions to the z_0 parameter. Solid lines denote down-slope velocity (u) whereas dashed lines denote buoyancy (b). Fixed parameters: $H = 12$, $Pr = 1$.

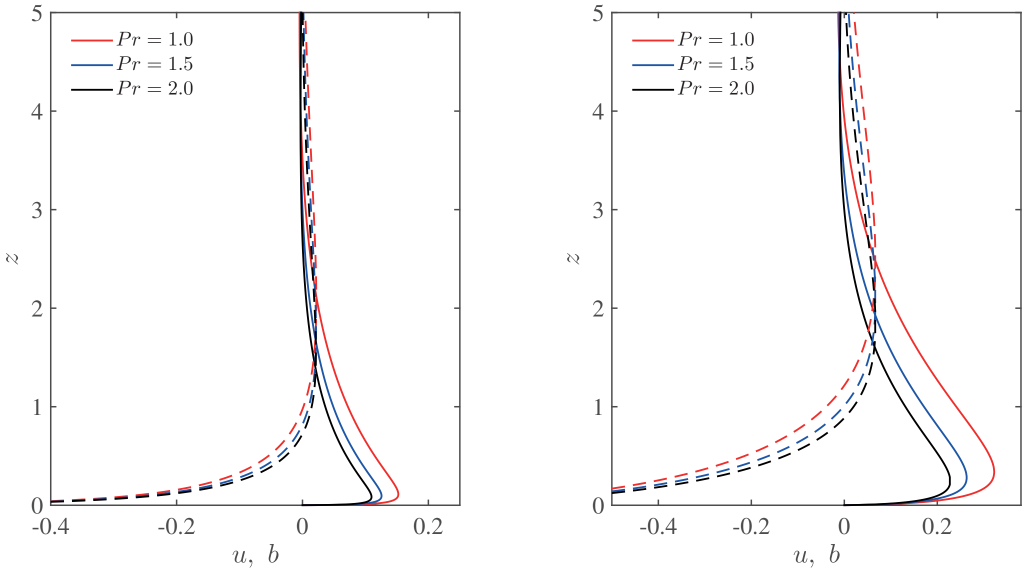

Figure 2.4 – Sensitivity of the normalised A1 (left) and A3 (right) solutions to the Pr parameter. Solid lines denote down-slope velocity (u) whereas dashed lines denote buoyancy (b). Displayed solutions correspond to: $H = 12$, $z_0 = 0.001$.

Under stably stratified environments pressure fluctuations induced by gravity waves sum to those induced by turbulence, and yield an increase in the total momentum flux, without directly influencing the buoyancy flux (Mahrt, 1998). This results in turbulent Prandtl numbers that are usually larger than unity. Variations by a factor of 2 for Pr, perhaps even more under conditions of strong stratification, are common and that can lead changes the relative shapes of vertical profiles of velocity and buoyancy considerably. The sensitivity of the solution to variations in the Pr parameter is displayed in Fig. 2.4. As above, the closed form solution (A1) is intercompared to the WKB solution (A3). Variations in Pr affect the solution throughout the domain for both A1 and A3. larger Pr result in weaker thermal and dynamic boundary-layers, and in a proportional decrease in u_j and z_j. Such a behavior could have been anticipated, since a larger Pr in conjunction with the constant (imposed) surface buoyancy is expected to result in a lower surface buoyancy flux, i.e. in a lower rate of potential energy injected into the system.

To study the sensitivity of the solution on the h parameter we considered a $\pm 10\%$ h-variation, and results are displayed in Fig. 2.5. Despite the non-negligible changes in $K(z)$ in the outer regions of the flow we observe a modest $\approx \pm 0.5\%$ variation in $\max(u)$ and a $\approx \pm 5\%$ variation in z_j, $\min(u)$ and z_r (the location of $\min(u)$), which is well within the degree of accuracy of the current study. Recall that variations in h lead to the same first order Taylor expansion of $K(z)$ around z_0, therefore the inner regions of the flow are relatively insensitive to the exact h value.

2.5 On the computation of the solution

The computation of the Gauss hypergeometric function ${}_2F_1$ with all its parameters complex is known to be a non-trivial task. Although the ${}_2F_1$ function is merely a power series expansion (whose implementation is apparently immediate), its use is prone to cancellation and round-off error, which become especially significant for certain ranges of the parameters and of the independent variable (Pearson, 2009). In our case, the solution $f = b + iu$ is evaluated in $y \in (z_0/H, 1)$, which is within the radius of convergence (R) of the hypergeometric functions that define f (the radius of convergence of ${}_2F_1(a,b,c,y)$ is $|y| = 1$). The solution computed here represents the ${}_2F_1$ functions as truncated power series, i.e. ${}_2F_1(a,b,c,y) = [(a)_k(b)_k]/[(c)_k k!]y^k$, where a, b, c are the three input parameters, $(\cdot)_k$ is the Pochhammer symbol and $k!$ denotes the factorial of $k = 1, 2, \ldots N$. All computations are performed in double precision arithmetic. In Fig. 2.5 we display the convergence of the solution, in terms of z_j and $\max(u)$, for a given set of z_0 values and $H = 10$. The solution shows sub-logarithmic convergence for both $e_{z_j} = 100(z_j^N - z_j)/z_j$ and $e_{\max(u)} = 100[\max(u^N) - \max(u)]/\max(u)$, and clearly, the smaller the z_0 parameter, the slower the resulting convergence rate. This behavior is justified by the fact that as z_0 is reduced, the solution is evaluated closer to R, where the convergence of ${}_2F_1$ in its power series form is known to be retarded. Note that despite the slow convergence of the solution, its evaluation is stable throughout the range of realistic z_0, and is significantly more efficient than a direct numerical solution of the equivalent model, which for the considered z_0 values would require an extremely fine spatial stencil. The efficacy of the

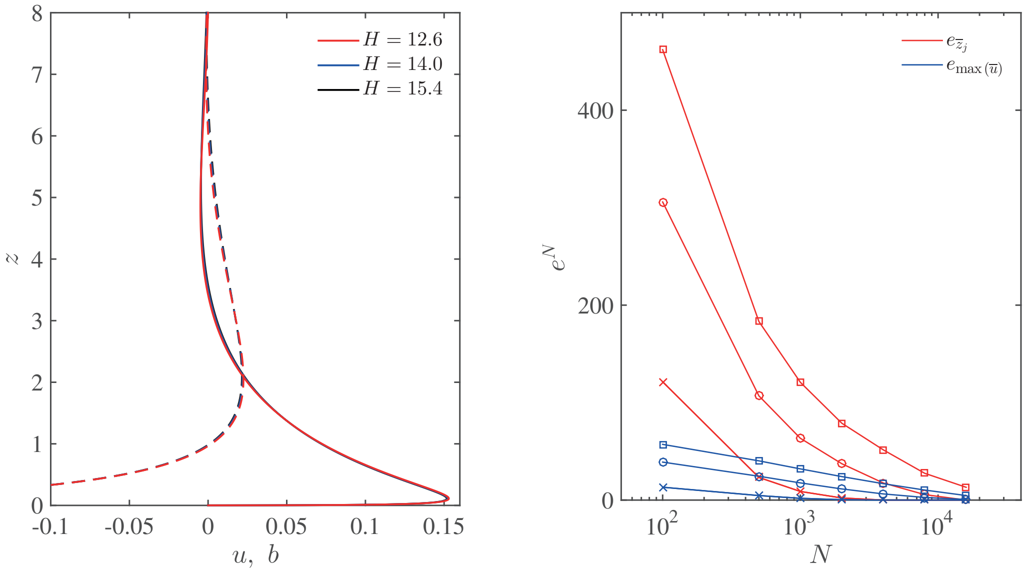

Figure 2.5 – Left plot: Sensitivity of velocity u (solid lines) and buoyancy b (dashed lines) profiles on the H parameter. Right plot: convergence test, relative percentage error for z_j (red lines) and $\max(u)$ (blue lines) as a function of N, where N represents the number of terms considered in the truncated ${}_2F_1$ series. Parameters for the H-sensitivity study (left plot): $H_1 = 11.2$, $H_2 = 14$, $H_3 = 16.8$ and $z_0 = 0.001$. Parameters for the convergence test (right plot): $z_0 = 0.00001$ (squares), $z_0 = 0.0001$ (circles), $z_0 = 0.001$ (crosses) and $H = 14$. We define $e_{z_j} = 100(z_j^N - z_j)/z_j$ and $e_{\max(u)} = 100[\max(u^N) - \max(u)]/\max(u)$, where $(\cdot)^N$ represents a quantity computed truncating the ${}_2F_1$ series to N terms, and where z_j and $\max(u)$ represent quantities that are exact in double precision arithmetic.

series summation can be much improved by various techniques (e.g., Shanks method, Padé summation, etc.), but such an analysis is beyond the goal of the current study.

2.6 Conclusions

To conclude, a closed form solution of the Prandtl model equations has been proposed herein, valid for O'Brien-type eddy diffusivities and constant Prandtl number. The solution is conceived for the specific problem of katabatic flows and is an adaptation of the solution proposed in Nieuwstadt (1983) for the Ekman-layer equations, generalized to account for $Pr \neq 1$. Its characteristics have been discussed assuming transfer coefficients for momentum and buoyancy in accordance to MOST (albeit the solution lend itself to more general K-parameterisations). In the specific, the dependence of the normalised solution on the model dimensionless parameters Pr and $\hat{z}_0 \hat{N}^2 \hat{b}_s^{-1}$ has been tested and compared against corresponding WKB solutions. For the same geometrical and physical parameters, profiles show significant variations in both phase and amplitude of extrema with respect to their WKB counterparts: stronger surface gradients (inversely proportional to Pr) are combined with overall reduced slope-parallel fluxes, and the LLJ is further displaced toward the wall. In addition, its peak velocity, LLJ height, and surface gradients proved to be strongly sensitive to variations of the dimensionless parameter $\hat{z}_0 \hat{N}^2 \hat{b}_s^{-1}$, highlighting a more complex coupling between the velocity and buoyancy fields. The proposed model can be of use to validate numerical or patched / matched solutions of the Prandtl equations, and to improve future stable boundary layer parameterisations, when coupled with other parts of the boundary layer physics.

Bibliography

C. M. Bender and S. A. Orszag. *Advanced mathematical methods for scientists and engineers*, volume 63. 1979.

B. Burkholder, E. Fedorovich, and A. Shapiro. Evaluating subgrid-scale models for large-eddy simulation of turbulent katabatic flow. In *Quality and reliability of large-eddy simulations II*, ERCOFTAC Series, pages 149–160, Dordrecht, 2011. Springer Netherlands.

P. C. Chu. An instability theory of ice-air interaction for the formation of ice edge bands. *J Geophys Res*, 92(C7):6966–6970, 1987.

F. Defant. Zur theorie der hangwinde, nebst bemerkungen zur theorie der berg- und talwinde. *Archiv für Meteorologie, Geophysik und Bioklimatologie Serie A*, 1:421–450, 1949.

E. Fedorovich and A. Shapiro. Turbulent natural convection along a vertical plate immersed in a stably stratified fluid. *J Fluid Mech*, 636:41–57, 2009a.

E. Fedorovich and A. Shapiro. Structure of numerically simulated katabatic and anabatic flows along steep slopes. *Acta Geophys*, 57(4):981–1010, 2009b.

J. W. Greuell, M. R. Broeke Van den, W. Knap, C. Reijmer, P. Smeets, , and I. Struijk. PASTEX: A glacio-meteorological experiment on the Pasterze (Austria). Technical report, Institute forMarine and Atmospheric Research, Utrecht University, Utrecht, 1994.

B. Grisogono and J. Oerlemans. Katabatic flow: Analytic solution for gradually varying eddy diffusivities. *J Atmos Sci*, 58(21):3349–3354, 2001.

B. Grisogono and J. Oerlemans. Justifying the WKB approximation in pure katabatic flows. *Tellus*, 54(5):453–462, 2002.

L. N. Gutman. On the theory of the katabatic slope wind. *Tellus*, 35A:213–218, 1983.

L. N. Gutman and V. M. Malbakhov. On the theory of the katabatic winds of Antarctica. *Met. Issled.*, 9:150–155, 1964.

M. Lehner, C. D. Whiteman, S. W. Hoch, D. Jensen, E. R. Pardyjak, L. S. Leo, S. Di Sabatino, and H. J. S. Fernando. A case study of the nocturnal boundary layer evolution on a slope at the foot of a desert mountain. *J Appl Meteorol Clim*, 54(4):732–751, 2015.

V. N. Lykosov and L. N. Gutman. Turbulent boundary layer above a sloping underlying surface. *Proc USSR Acad Sci*, 8:799–809, 1972.

L. Mahrt. Stratified atmospheric boundary layers and breakdown of models. *Theor Comput Fluid Mech*, 11:263–279, 1998.

P. Monti, H. J. S. Fernando, M. Princevac, W. C. Chan, T. A. Kowalewski, and E. R. Pardyjak. Observations of flow and turbulence in the nocturnal boundary layer over a slope. *J Atmos Sci*, 59(17):2513–2534, 2002.

P. M. Morse and H. Feshbach. *Methods of theoretical physics*. McGraw-Hill, 1953.

D. F. Nadeau, E. R. Pardyjak, C. W. Higgins, and M. B. Parlange. Similarity scaling over a steep alpine slope. *Boundary-Layer Meteorol*, 147(3):401–419, 2013.

C. J. Nappo and R. K. Shankar. A model study of pure katabatic flows. *Tellus*, 39(1):61–71, 1987.

F. T. M. Nieuwstadt. On the solution of the stationary, baroclinic Ekman-layer equations with a finite boundary-layer height. *Boundary-Layer Meteorol*, 26(4):377–390, 1983.

T. H. Nylen, A. G. Fountain, and P. T. Doran. Climatology of katabatic winds in the McMurdo dry valleys, southern Victoria Land, Antarctica. *Journal of Geophysical Research: Atmospheres*, 109(D3):1–9, 2004.

J. J. O'Brien. A note on the vertical structure of the eddy exchange coefficient in the planetary boundary layer. *J Atmos Sci*, 27(8):1213–1215, 1970.

J. Oerlemans. Quantifying global warming from the retreat of glaciers. *Science*, 264(5156): 243–245, 1994.

J. Oerlemans. The atmospheric boundary layer over melting glaciers. In *Clear and Cloudy Boundary Layers*, pages 129–153. Royal Netherlands Academy of Arts and Sciences, 1998.

J. Oerlemans and B. Grisogono. Glacier winds and parameterisation of the related surface heat fluxes. *Tellus*, 54(5):440–452, 2002.

J. Oerlemans and H. F. Vugts. A meteorological experiment in the melting zone of the Greenland ice sheet. *Bull Am Meteorol Soc*, 74(3):355–365, 1993.

H. J. Oldroyd, G. G. Katul, E. R. Pardyjak, and M. B. Parlange. Momentum balance of katabatic flow on steep slopes covered with short vegetation. *Geophys Res Lett*, 41(13):4761–4768, 2014.

T. R. Parish and D. H. Bromwich. Continental-scale simulation of the Antarctic katabatic wind regime. *J Clim*, 4(2):135–146, 1991.

T. R. Parish and D. H. Bromwich. A case study of Antarctic katabatic wind interaction with large-scale forcing. *Mon Weather Rev*, 126(1):199–209, 1998.

Thomas R. Parish. On the role of Antarctic katabatic winds in forcing large-scale tropospheric motions. *J Atmos Sci*, 49(15):1374–1385, 1992.

J. Pearson. *Computation of hypergeometric functions*. PhD thesis, Oxford, 2009.

R. A. Pielke. Mesoscale numerical modeling. *Adv Geophys*, 23:185–344, 1984.

L. Prandtl. *Führer durch die strömungslehre*. Vieweg & Sohn, Braunschweig, 1942.

I. A. Renfrew. The dynamics of idealized katabatic flow over a moderate slope and ice shelf. *Q J R Meteorol Soc*, 130(598):1023–1045, 2004.

A. Renfrew, I. and S. Anderson, P. Profiles of katabatic flow in summer and winter over Coats Land, Antarctica. *Q J R Meteorol Soc*, 132(616):779–802, 2006.

M. W. Rotach and D. Zardi. On the boundary-layer structure over highly complex terrain: Key findings from MAP. *Q J R Meteorol Soc*, 133(625):937–948, 2007.

A. Shapiro and E. Fedorovich. Natural convection in a stably stratified fluid along vertical plates and cylinders with temporally periodic surface temperature variations. *J Fluid Mech*, 546:295–311, 2005.

A. Shapiro and E. Fedorovich. Katabatic flow along a differentially cooled sloping surface. *J Fluid Mech*, 571:149–175, 2007.

P. F. Sheridan, S. B. Vosper, and A. R. Brown. Characteristics of cold pools observed in narrow valleys and dependence on external conditions. *Q J R Meteorol Soc*, 140(679):715–728, 2014.

R. B. Stull. *An introduction to boundary layer meteorology*. Kluwer Academic Publishers, Dordrecht, 1988.

C. D. Whiteman. Observations of thermally developed wind systems in mountainous terrain. *Atmos Process over complex terrain, Meteor Monogr*, 45:5–42, 1990.

C. D. Whiteman. Mountain meteorology: Fundamentals and applications. *Mountain Research and Development*, 21(1):355, 2000.

C. D. Whiteman, S. Zhong, W. J. Shaw, J. M. Hubbe, X. Bian, and J. Mittelstadt. Cold pools in the Columbia basin. *Weather and Forecasting*, 16(4):432–447, 2001.

D. Zardi and S. Serafin. An analytic solution for time-periodic thermally driven slope flows. *Q J R Meteorol Soc*, 141(690):1968–1974, 2015.

3 Direct numerical simulation of slope flows: characterization of mean flow and turbulence

Abstract

Turbulent convection of stably stratified fluid over an unbounded, smooth, sloping surface is studied using Direct Numerical Simulations (DNS), within the framework of the Prandtl model. DNS is computational expensive when compared to evaluating analytic one-dimensional solutions (e.g. the one proposed in Ch. 2), but overcomes the need for a parameterization of turbulent mixing, since turbulence is directly resolved down to the dissipative scales of the flow. This makes it the method of choice in the current study, where the aim is to characterize turbulence effects on the system, to inform parameterizations for use in lower-order models. In the specific, the study focuses on variations of mean flow, second order statistics, and budgets of mean (MKE) and turbulent kinetic energy (TKE), as a function of the sloping angle (α) and Reynolds number (Re), at fixed Prandtl number ($Pr = 1$). Four sloping angles ($\alpha = 15^\circ, 30^\circ, 60^\circ$ and 90°) and three Reynolds number ($Re = 3 \times 10^5, 4 \times 10^5$ and 4.6×10^5) are considered. A dynamic and a thermodynamic identity are highlighted, which can diagnose the quality of the averaging operation. Turbulent anabatic (upward moving warm fluid along the slope) and katabatic (downward moving cold fluid along the slope) regimes are found to be structurally similar at high sloping angles, qualitatively resembling the analytic solution presented in Chapter 2, but undergo a different transition as the sloping angle decreases, leading to stark statistical differences between the two flow regimes as $\alpha \lessapprox 30^\circ$. In addition, budget equations show how MKE is fed into the system through the imposed surface buoyancy, and turbulent fluctuations redistribute it from the low-level jet (LLJ) nose toward the below- and above-LLJ regions. Analysis of the TKE budget equation suggests a subdivision of the boundary layer of anabatic and katabatic flows into three distinct regions: 1. an *outer layer*, where turbulent transport balances dissipation, 2. an *intermediate layer*, where shear and buoyant production overcome dissipation, and turbulent and pressure transport terms relocate the excess of TKE, and 3. a *wall layer*, capped by the jet nose, where pressure and turbulent transport balance dissipation and viscous diffusion of TKE. Interestingly, a zone of global backscatter (energy

transfer from the turbulent eddies to the mean flow) is consistently found below the LLJ in both flow regimes.

3.1 Introduction

When an inclined surface is thermally perturbed, the resulting buoyancy force projects in both the along- and across-slope directions. Surface cooling results in a downslope flow (katabatic flow), whereas surface heating triggers an upslope flow (anabatic flow). The significance of thermally driven flows along sloping surfaces is rarely disputed given the role they play over a broad range of scales and applications. Katabatic and anabatic flows are ubiquitous over complex terrain (Whiteman, 1990; Rampanelli et al., 2004; Haiden and Whiteman, 2005; Fernando, 2010; Zardi and Whiteman, 2013; Oldroyd et al., 2014, 2015; Grachev et al., 2015), and despite their local nature, their interaction with larger scale forcing mechanisms can favor the development of cyclonic vorticity in the middle and upper troposphere (Parish, 1992; Parish and Bromwich, 1998). Katabatic winds are regulating energy, momentum and mass transfer over the ice sheets of Greenland and Antarctica (Egger, 1985; Parish, 1992; Parish and Bromwich, 1998; Renfrew, 2004; Renfrew, I. and Anderson, P., 2006), and are also influencing the movement of the marginal ice zone (Chu, 1987). In addition, katabatic flows are a permanent feature of the atmospheric boundary layer (ABL) over melting glaciers (Greuell et al., 1994; Oerlemans, 1998), whose constant retreat is a matter of public interest, given its impact on both the sea level rise and on water resource management.

Prandtl (1942) framed the problem of slope flows in a conceptually simple model, considering a doubly-infinite (no leading edges) plate which is uniformly heated or cooled and lies within a stably stratified environment. The Prandtl model (Prandtl, 1942) states that slope-parallel advection of buoyancy is balanced by buoyancy flux divergence, whereas the parallel-to-slope component of buoyancy balances with momentum flux divergence. This particular type of flows are termed *equilibrium flows* (Mahrt, 1982), given the nature of the balance between a turbulent flux divergence and a generation/destruction mechanism. Under such settings the Boussinesq equations of motion and thermal energy reduce to one-dimensional form, which allows for analytical treatment. Accounting for a base stratification allows the solutions to approach steady-state conditions at large times, whereas in the absence of a stable stratification (classical solutions), the thermal and dynamic boundary layers (TBL and DBL in the following) grow in an unbounded manner (Menold and Yang, 1962).

The original model assumed constant turbulent diffusivities – and is therefore incapable of representing the observed steep near-surface gradients, as shown in Chapter 2. In addition, the return flow region predicted by the constant-K solution is usually stronger, when compared to measurements or numerical simulations, and also vanishes more rapidly away from the surface. These limitation were recently addressed in (Grisogono and Oerlemans, 2001, 2002), where an approximate analytical solution able to account for spatially variable eddy diffusivities was proposed, valid under the WKB approximation (after Wentzel–Kramers–Brillouin).

Modifications of the Prandtl model to allow for variations in surface forcing (Shapiro and Fedorovich, 2007; Burkholder et al., 2009), in the slope angle (Zammett and Fowler, 2007), and to account for weakly non-linear effects (Grisogono et al., 2015), were also recently proposed.

The Prandtl conceptual approach is also of interest for numerical modelers. It alleviates computational costs by constraining the geometry to regular domains, thus allowing the use of efficient numerical schemes such as methods based on finite differences or spectral expansions. The existence of a statistically steady state solution also provides some benchmark quantitative analysis. The past decades have seen significant advances in computational performance, achieved through both improvements of computer hardware and of numerical algorithms to solve differential problems. Nevertheless, computational cost of simulating high *Re* flows over long slopes remains prohibitively high, and has motivated the use of closure models that aim at reducing the resolution requirements in the dissipative range, especially if energy-containing scales are of primary interest (Pope, 2000). Schumann (1990) pioneered the use of large-eddy simulation (LES) to resolve turbulent anabatic flows within the conceptual settings of the Prandtl model. LES profiles were found to be in qualitative agreement with the constant-K solution profiles in terms of sensitivity to the model parameters, but also confirmed that transfer coefficients have to decrease as the surface is approached, for parameterized lower dimensional models to match LES surface-dissipation rates. More recent LES studies – all within the Prandtl model framework – also unfolded the main structure of mean flow and turbulence in katabatic flows, and provided insights on the dependency of the solution on the system parameters (Skyllingstad, 2003; Axelsen and Dop, 2009). Analytic solutions, observations and numerical studies have shown that the structure of slope winds is further complicated – when compared against classical boundary layer profiles – by the formation of the LLJ and by the presence of several zero-gradient layers in the state variables. This is direct manifestation of additional dynamics induced by the interplay of stable stratification, turbulence and by the sloping surface. Such complications have led to a fundamental mistrust on the performance and validity of classical LES closure models for simulation of slope flows. For instance, because of the stable stratification, katabatic flows experience a reduction in the size of the eddies, which leads to an increased reliance on subgrid-scale (SGS) terms in the bulk of the flow. At the same time, because of the stable stratification, turbulence can become spatially and temporally intermittent and highly anisotropic (Meroney et al., 1997; Mahrt, 1998, 2013). For such conditions, the main assumptions upon which SGS models are derived (i.e. Kolmogorov's theories) become questionable (Pope, 2000). Besides, the lack of a near-surface closure theory (Monti et al., 2014) makes it impossible to prescribe adequate surface fluxes in simulations. These limitations have motivated recent use of direct numerical simulations (DNS), which, despite their modest range of *Re*, provide the most comprehensive view of the flow structure (Shapiro and Fedorovich, 2004a,b; Fedorovich and Shapiro, 2009b). These studies showed that slope flow statistics are sensitive to variations in the parameter space. The magnitude of the surface forcing, the slope angle and the strength of the ambient stratification all play a role in determining the characteristics of the flow. This finding motivated recent efforts towards a derivation of scaling relations that allow the elimination of the dependency

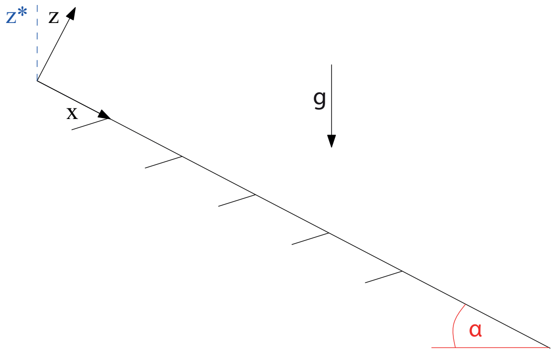

Figure 3.1 – Slope-aligned coordinate system.

of the solution on the sloping angle for instance (Shapiro and Fedorovich, 2014). Scaling relations are of interest since they facilitate the design of experiments and have potentials to yield significant computational savings in parametric studies when explored through LES and DNS.

The problem of anabatic and katabatic flows and the properties of the LLJ in the near wall region are here explored through high resolution DNS. The focus is on variations in the slope-normal structure of selected flow's statistics and in integrated quantities as a function of the model parameters (the sloping angle and Re). Throughout the study, the flow is driven through a homogeneous constant surface buoyancy force. Note that such a forcing has not yet received much attention in numerical slope-flow simulation studies. In addition, we limit the study to $Pr = 1$. Mean kinetic energy (MKE) and turbulent kinetic energy budget (TKE) terms are also evaluated and their interaction across various layers within the boundary layer discussed. The aim here is to explore interactions between turbulence and the mean state as well as the role of the LLJ in energy and momentum exchanges. The long-term goal is to solicit improvements of current turbulence closure models for sloping and stable conditions that can be imminently used in large-scale atmospheric models.

The governing equations for the problem are derived in section 2. Section 3 provides details on the the numerical algorithm and on the setup of simulations, and main results are presented in §4 . Summary and concluding remarks follow in §5.

3.2 Equations of motion

Thermal convection of turbulent stratified fluid flow over sloping surfaces can be conveniently described in a rotated reference system $(\hat{x}, \hat{y}, \hat{z})$ aligned in the along-slope direction ($\hat{}$ denotes a dimensional variable), as displayed in Fig. 3.1, and to split the potential temperature $\hat{\theta}(\hat{\mathbf{x}}, \hat{t})$ into a base state $\hat{\theta}_\infty(\hat{\mathbf{x}})$ and a perturbation component $\hat{\theta}''(\hat{\mathbf{x}}, \hat{t}) \equiv \hat{\theta}(\hat{\mathbf{x}}, \hat{t}) - \hat{\theta}_\infty(\hat{\mathbf{x}})$ as proposed by Prandtl (1942). Assuming the base state $\hat{\theta}_\infty(\hat{\mathbf{x}})$ to be a linear function of the vertical coordinate direction $\hat{z}^*$, results in $\hat{N} \equiv \sqrt{\hat{\beta}\frac{d\hat{\theta}_\infty}{d\hat{z}^*}} = constant$, where $\hat{N}$ is the buoyancy frequency (equivalent to the Brunt–Väisälä frequency in stable flows). The thermal expansion coefficient $\hat{\beta} = \hat{g}/\hat{\theta}_\infty$ is set to be constant for convenience and $\hat{g}$ is the gravitational acceleration constant. Moreover, invoking the Boussinesq approximation (i.e. ignoring density differences except where they appear in terms multiplied by $\hat{g}$) and neglecting rotational effects, the conservation equations in their dimensional form reduce to

$$\frac{\partial \hat{u}_i}{\partial \hat{t}} + \hat{u}_j \frac{\partial \hat{u}_i}{\partial \hat{x}_j} = -\frac{\partial \hat{\pi}}{\partial \hat{x}_i} + \hat{\nu} \frac{\partial^2 \hat{u}_i}{\partial \hat{x}_j^2} - \hat{\beta}\hat{\theta}''(\hat{\mathbf{x}}, \hat{t})\,[\delta_{i1} \sin\alpha - \delta_{i3} \cos\alpha], \tag{3.1}$$

$$\frac{\partial \hat{u}_i}{\partial \hat{x}_i} = 0, \tag{3.2}$$

$$\frac{\partial \hat{\theta}''}{\partial \hat{t}} + \frac{\partial \hat{u}_j \hat{\theta}''}{\partial \hat{x}_j} = -\frac{\partial \hat{u}_j \hat{\theta}_\infty}{\partial \hat{x}_j} + \hat{\kappa} \frac{\partial^2 \hat{\theta}''}{\partial \hat{x}_j^2}, \tag{3.3}$$

where $\hat{t}$ (s) denotes time, $\hat{u}_i$ (m s^{-1}) are the velocity components in the three coordinate directions $(\hat{x}, \hat{y}, \hat{z})$ (m), $\hat{\pi} \equiv [\hat{p} - \hat{p}_\infty(\hat{x}, \hat{y}, \hat{z})]/\hat{\rho}_\infty$ (m s^{-2}) is the normalized deviation of pressure from the background hydrostatic value, $\hat{\rho}_\infty$ (kg m^{-3}) is a reference constant density, α (rad) is the slope angle, $\hat{\nu}$ (m^2 s^{-1}) and $\hat{\kappa}$ (m^2 s^{-1}) are the kinematic molecular viscosity and diffusivity coefficients. Note that the dissipation term has been neglected in the energy equation due to low velocities involved. Introducing the buoyancy variable $\hat{b}(\hat{\mathbf{x}}, \hat{t}) \equiv \hat{\beta}\hat{\theta}''(\hat{\mathbf{x}}, \hat{t})$, and since $\hat{z}^*(\hat{\mathbf{x}}) \equiv -\hat{x}\sin\alpha + \hat{z}\cos\alpha$, Eqs. 4.1, 4.2 and 4.3 can be re-written as follows

$$\frac{\partial \hat{u}_i}{\partial \hat{t}} + \hat{u}_j \frac{\partial \hat{u}_i}{\partial \hat{x}_j} = -\frac{\partial \hat{\pi}}{\partial \hat{x}_i} + \hat{\nu} \frac{\partial^2 \hat{u}_i}{\partial \hat{x}_j^2} - \hat{b}(\hat{\mathbf{x}}, \hat{t})\,[\delta_{i1} \sin\alpha - \delta_{i3} \cos\alpha], \tag{3.4}$$

$$\frac{\partial \hat{u}_i}{\partial \hat{x}_i} = 0, \tag{3.5}$$

$$\frac{\partial \hat{b}}{\partial \hat{t}} + \frac{\partial \hat{u}_j \hat{b}}{\partial \hat{x}_j} = \hat{N}^2 [\hat{u}_1 \sin\alpha - \hat{u}_3 \cos\alpha] + \hat{\kappa} \frac{\partial^2 \hat{b}}{\partial \hat{x}_j^2}. \tag{3.6}$$

3.2.1 Normalisation of the equations and governing parameters

To express the governing equations as a function of suitable dimensionless parameters we define a characteristic velocity, buoyancy and length scales can be defined as

$$\hat{L} \equiv \frac{|\hat{b}_s|}{\hat{N}^2}, \qquad \hat{B} \equiv |\hat{b}_s|, \qquad \hat{U} \equiv \frac{|\hat{b}_s|}{\hat{N}}, \tag{3.7}$$

where $\hat{b}_s$ is the surface buoyancy term. When the imposed $\hat{b}_s > 0$, the slope flow is termed anabatic. Conversely, when $\hat{b}_s < 0$, the slope flow is katabatic. These aforementioned parameters can now be used to introduce the following normalized variables:

$$x_i \equiv \hat{x}_i/\hat{L}, \qquad u_i \equiv \hat{u}_i/\hat{U}, \qquad \pi \equiv \hat{\pi}/\hat{U}^2, \qquad b \equiv \hat{b}/\hat{B}. \tag{3.8}$$

Relations 3.7 are derived selecting $\hat{b}_s$ and $\hat{N}$ as repeating parameters for convenience though this choice is by no means unique and other options are possible. Substituting the expressions 3.8 into the governing equations 4.4, 3.5 and 3.6 results in

$$\frac{du_i}{dt} = -\frac{\partial \pi}{\partial x_i} - b(\delta_{i1}\sin\alpha - \delta_{i3}\cos\alpha) + \frac{1}{Re}\frac{\partial^2 u_i}{\partial x_j^2}, \tag{3.9}$$

$$\frac{\partial u_i}{\partial x_i} = 0, \tag{3.10}$$

$$\frac{db}{dt} + \frac{\partial u_j b}{\partial x_j} = (u_1 \sin\alpha - u_3\cos\alpha) + \frac{1}{RePr}\frac{\partial^2 b}{\partial x_j^2}, \tag{3.11}$$

where $Re = \hat{b}_s^2\,\hat{\nu}^{-1}\,\hat{N}^{-3}$ can be interpreted as a Reynolds number for the flow, defined as a ratio between the energy production at the surface (given that $\hat{b}_s^2 > 0$) and the work against the background stratification and viscous forces. From equations (3.9), (3.10) and (3.11) it follows that any relation between $\hat{u}, \hat{v}, \hat{w}, \hat{p}, \hat{b}$, and $\hat{x}, \hat{y}, \hat{z}$ will be the same, if the different flows are characterized by the same similarity parameters α, Re and Pr.

3.3 Simulations

Equations 3.9, 3.10 and 3.11 are integrated across a range of sloping angles α and Re, considering both anabatic (upslope) and katabatic (downslope) flow regimes, as summarized in Table 3.1. Given the computational cost of DNS, variations in the Re parameters are limited to the $\alpha = 60°$ case.

The DNS algorithm is a modification of the code that has been previously used to study land atmosphere interaction processes (Albertson and Parlange, 1999a,b), to develop and test linear and nonlinear LES subgrid scale models (Meneveau et al., 1996; Porté-Agel et al., 2000; Porté-Agel, 2004; Higgins et al., 2003; Porté-Agel, 2004; Bou-Zeid et al., 2005; Lu and Porté-Agel, 2010, 2013), to design surface-flux parameterizations (Hultmark et al., 2013), and to develop the dynamic surface roughness model (Anderson and Meneveau, 2011). Equations are solved in rotational form to ensure conservation of mass and kinetic energy (Orszag and Pao, 1975). A pseudospectral collocation approach (Orszag, 1969, 1970) based on truncated Fourier expansions is used in the x, y coordinate directions whereas a second-order accurate centered finite differences scheme is adopted in the slope-normal direction, requiring a staggered grid approach for the u, v, p, b state variables (these are stored at $(i+1/2)\Delta_Z$, where i denotes a given layer of collocation nodes in the slope-normal direction). Time integration

Label	$L_x \times L_y \times L_z$	$N_x \times N_y \times N_z$	α	T	Re	b_s
A, G	$0.252^2 \times 0.384$	$384^2 \times 1032$	$90°$	6.28	4.6×10^5	± 1
B, H	$0.252^2 \times 0.384$	$384^2 \times 1032$	$60°$	7.25	4.6×10^5	± 1
C, I	$0.252^2 \times 0.384$	$384^2 \times 1032$	$30°$	12.57	4.6×10^5	± 1
D, J	$0.252^2 \times 0.384$	$384^2 \times 1032$	$15°$	24.28	4.6×10^5	± 1
E, K	$0.252^2 \times 0.384$	$256^2 \times 1032$	$60°$	7.25	4.0×10^5	± 1
F, L	$0.252^2 \times 0.384$	$256^2 \times 1032$	$60°$	7.25	3.0×10^5	± 1

Table 3.1 – Geometry and parameters for the DNS runs. L_i denotes the domain size in the three coordinate directions, N_i denotes the number of collocation nodes adopted in the three coordinate directions, T denotes the characteristic oscillation period of internal waves characterizing the system (see Sect. 3.4), $Re = \hat{b}_s^2\, \hat{\nu}^{-1}\, \hat{N}^{-3}$ and b_s is the imposed (normalized) surface buoyancy. Simulations $A-F$ correspond to $b_s = -1$, whereas cases $G-L$ correspond to $b_s = +1$.

is performed adopting a fully explicit second-order accurate Adams-Bashforth scheme. A fractional step method (Chorin, 1968; Temam, 1968) is adopted to compute the pressure field by solving an additional Poisson equation, which is derived enforcing mass continuity for the incompressible fluid $\frac{\partial u_i}{\partial x_i} = 0$. Further, all nonlinear terms are de-aliased adopting a $3/2$ rule so as to avoid artificial pile up of energy at the high wavenumber range (Kravchenko and Moin, 1997; Canuto et al., 2006).

To allow this specific study, significant efforts have been devoted to speedup the original algorithm, and to reduce its memory requirements. In the specific, openMP 4.0 (OpenMP Architecture Review Board, 2013) directives have been included to allow for a shared memory parallelization of loops which, together with a better organization of the structure of the algorithm, has resulted in a $\mathcal{O}(10)$ speedup.

Equations are integrated over a regular domain $[0, L_x] \times [0, L_y] \times [0, L_z]$, with boundary conditions $u(x, y, 0) = u(x, y, L_z) = b(x, y, L_z) = 0$ and $b(x, y, 0) = \hat{b}_s/\hat{B} = \pm 1$. The domain size is chosen in order to allow the representation of coherent structures populating the thermal and dynamic boundary layers, while at the same time allowing to resolve the flow in the dissipative range of scales.

As shown in Fig. 3.2, the slope-normal grid stencil satisfies the resolvability condition $\Delta_Z < 2\eta$, where $\eta = Re^{-3/4}\epsilon^{-1/4}$ is the Kolmogorov length scale in normalized units. The horizontal grid stencil ($\Delta_x = \Delta_y = 3\Delta_z$) does not fulfill the resolvability requirement, hence the need to verify the quality of proposed results. To do so, a higher resolution DNS run is performed for the $\alpha = 90°$ case, with grid satisfying $\Delta = (\Delta_x \cdot \Delta_y \cdot \Delta_z)^{1/3} < 2\eta$, where Δ denotes a reference grid size (Scotti et al., 1993). First and second order statistics are found to be in good agreement with those presented herein (not shown), underlining how current resolution is sufficient to represent most of the dissipative scales.

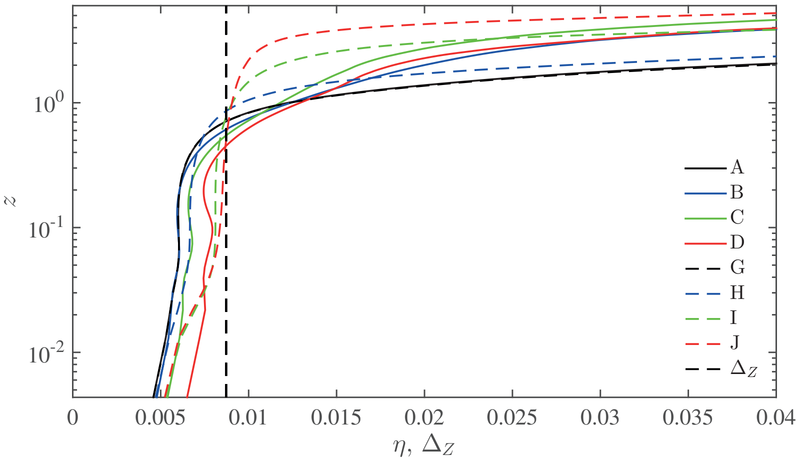

Figure 3.2 – Normalised Kolmogov's scale $\eta(z) = Re^{-3/4}\epsilon(z)^{-1/4}$ for anabatic (dashed lines) and katabatic (solid lines) cases, compared against the slope-normal stencil Δ_z.

Simulations are run for a minimum of $7T$, where $T = 2\pi \sin^{-1}\alpha$ is the characteristic (normalized) period of internal gravity waves that arise in the system due to the imposed stable background stratification. Statistics are computed over the last $5T$ for the cases $\alpha = 90°, \alpha = 60°$, and over the last $4T$ for the cases $\alpha = 30°, \alpha = 15°$ (previous steps are disregarded to allow turbulence to fully develop). All simulations are characterized by $Pr = 1$.

Throughout the study $\langle\cdot\rangle$ will denote averaging in time and along spatial coordinates of statistical homogeneity (x, y) and time fluctuations are written as $(\cdot)'$.

3.4 Time evolution and structure of the flow

The time evolution of the slope-normal integrated, space averaged, normalized stream-wise velocity $\langle u\rangle$ and buoyancy $\langle b\rangle$ is displayed in Fig. 3.3. The system exhibits the classical quasi-periodic, low-frequency, oscillatory behavior (surges), superimposed to a base flow, as observed in previous DNS (Fedorovich and Shapiro, 2009b) and in experiments (Monti et al., 2002; Princevac et al., 2008). It can be shown (McNider, 1982) that the slope-normal integrated $\langle u\rangle$, $\langle b\rangle$ variables behave as a system of coupled (damped) oscillators, whereby steady state is slowly reached through decaying oscillations characterized by a period $\hat{T} = 2\pi(\hat{N}\sin\alpha)^{-1}$ (normalized period is $T = 2\pi\sin^{-1}\alpha$), as shown here. For a typical atmospheric value of $\hat{N} = 10^{-2}$ (Hz) and sloping angles of 15°, 30° and 60°, such a period corresponds to approximately 40, 20 and 10 minutes. Averaging Eqs. 3.9, 3.10 and 3.11 in time and over directions of statistical homogeneity (x, y) results in

$$\sin(\alpha)\langle b\rangle = \frac{d\langle\tau_{xz}^{tot}\rangle}{dz}, \tag{3.12}$$

$$-\sin(\alpha)\langle u\rangle = \frac{d\langle\tau_{bz}^{tot}\rangle}{dz}, \tag{3.13}$$

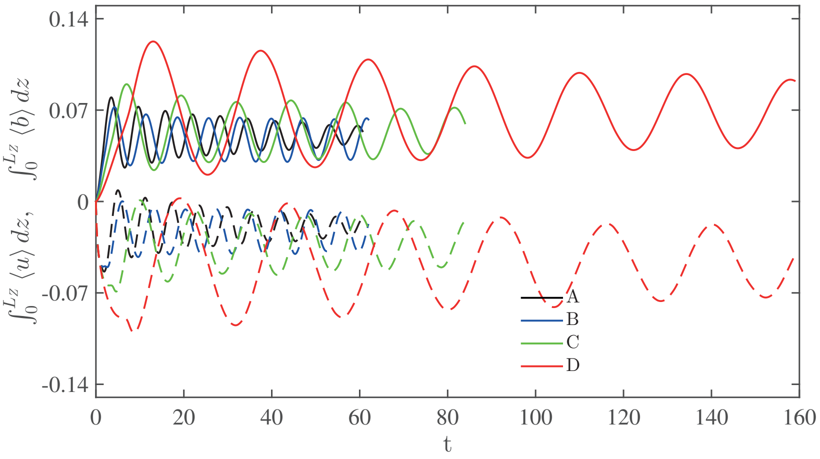

Figure 3.3 – Time evolution of slope-normal integrated $\langle u \rangle$ (solid lines) and $\langle b \rangle$ (dashed lines) fields for simulations A, B, C, and D (katabatic flow regime). The total time-integration period is shown for each run.

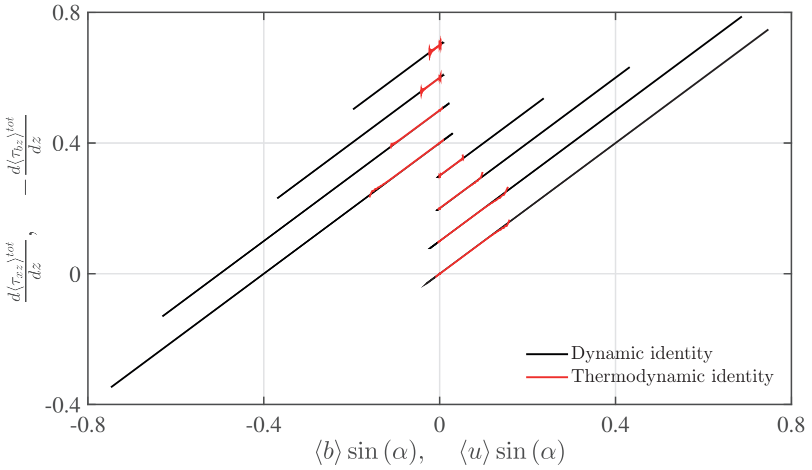

Figure 3.4 – Dynamic (black lines) and thermodynamic (red lines) identities (equations 3.12 and 3.13) for the considered simulations. Profiles have been shifted on the y axis to allow for proper visualization. We here denote $\langle \tau_{xz}^{tot} \rangle = \frac{1}{Re}\frac{d^2\langle u \rangle}{dz^2} + \langle u' w' \rangle$ and $\langle \tau_{bz}^{tot} \rangle = \frac{1}{RePr}\frac{d^2\langle b \rangle}{dz^2} + \langle b' w' \rangle$ (sum of molecular and turbulent kinematic fluxes of stream-wise momentum and buoyancy in the slope-normal direction).

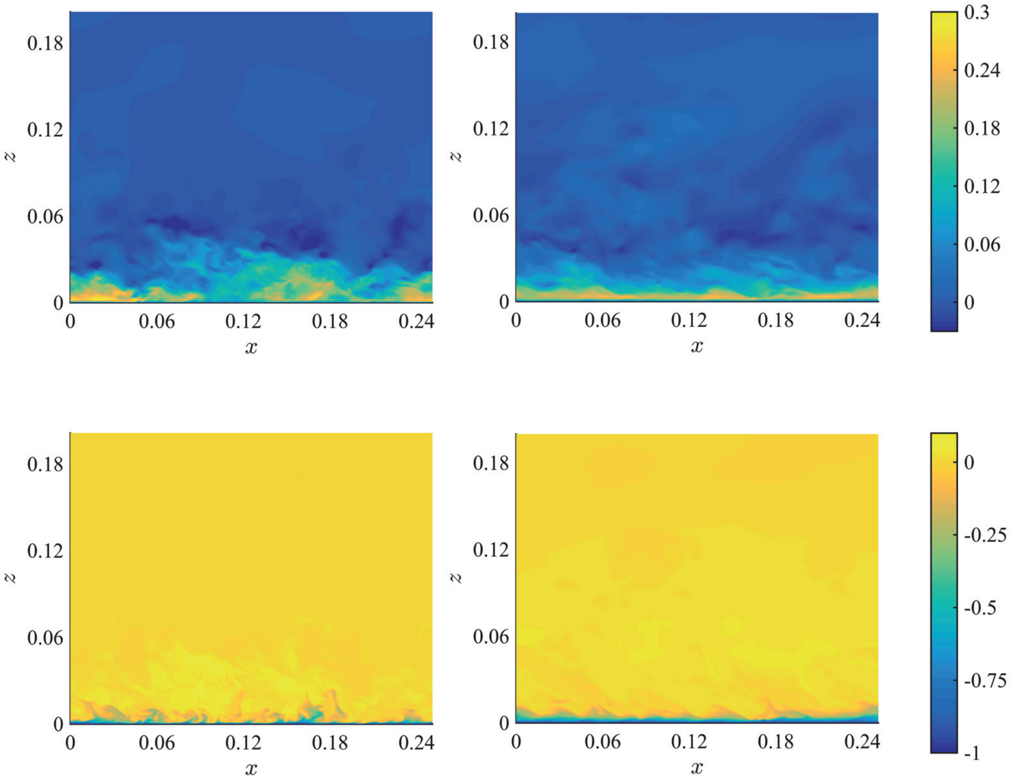

Figure 3.5 – Color contours of instantaneous streamwise velocity u (top figures) and buoyancy b (bottom figures), on the plane $y = L_y/2$ for simulations A (left figures) and D (right figures). The displayed $u(x,z)$ and $b(x,z)$ fields correspond to the crest of the last simulated gravity-wave oscillation for both runs. For detailed viewing, only the near-surface region of the total domain is shown.

where $\langle\tau_{xz}^{tot}\rangle = \frac{1}{Re}\frac{d^2\langle u\rangle}{dz^2} + \langle u'w'\rangle$ and $\langle\tau_{bz}^{tot}\rangle = \frac{1}{RePr}\frac{d^2\langle b\rangle}{dz^2} + \langle b'w'\rangle$ are the normalised total (molecular + turbulent) slope-normal kinematic momentum and buoyancy fluxes. Equations 3.12 and 3.13 can be used to test the quality of computed statistics (steady state is guaranteed only if the two identities hold). Numerical results are displayed in Fig. 3.4, and certify that averaging over $4T$, after a transient of at least $3T$ is sufficient to satisfy both Eqs. 3.12 and 3.13. Apparent oscillations characterizing the numerically computed thermodynamic identity (Eq. 3.13) are likely to be due to interpolation errors that arise when evaluating the flux gradient term $d\langle\tau_{bz}^{tot}\rangle/dz$ in the near surface region.

Figure 3.5 and 3.6 display a contour of the instantaneous stream-wise normalised velocity field (u) and of the normalised buoyancy field (b) for simulations A, D and G, J respectively. The TBL appears to be much shallower when compared to the DBL, as noted in prior DNS of sloping flows (Fedorovich and Shapiro, 2009a,b). A reversed flow characterizes the above-jet regions, resulting from the interaction between the flow and the background stably stratified environment, in qualitative agreement with the predictions of the linear Prandtl model

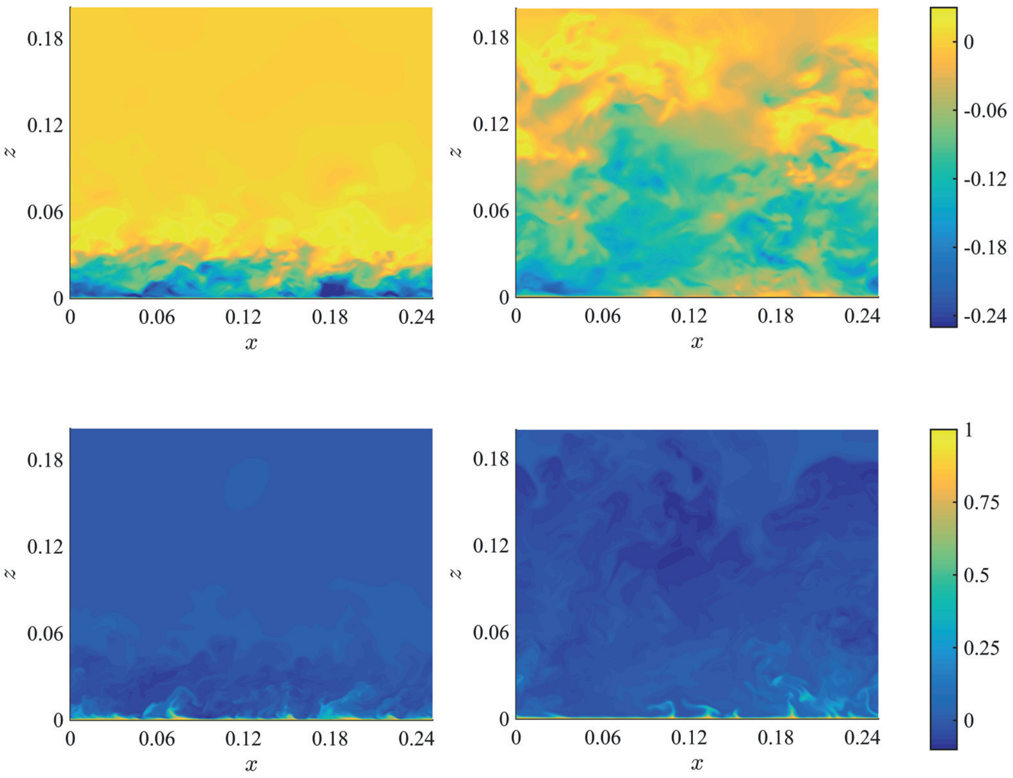

Figure 3.6 – Color contours of instantaneous streamwise velocity u (top figures) and buoyancy b (bottom figures), on the plane $y = L_y/2$ for simulations G (left figures) and J (right figures). The displayed $u(x,z)$ and $b(x,z)$ fields correspond to the crest of the last simulated gravity-wave oscillation for both runs. For detailed viewing, only the near-surface region of the total domain is shown.

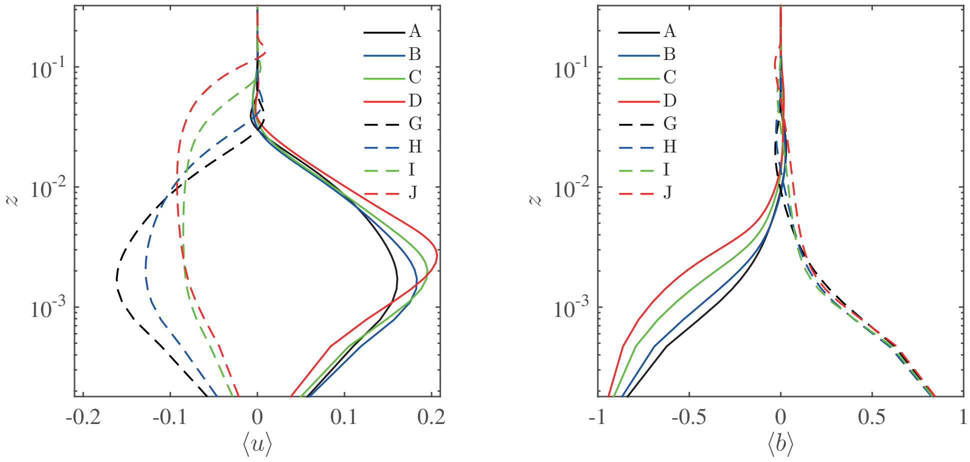

Figure 3.7 – Comparison of stream-wise velocity $\langle u \rangle$ (left) and buoyancy $\langle b \rangle$ (right) for anabatic (dashed lines) and katabatic (solid lines) flow cases at $Re = 4.6 \times 10^5$.

(Prandtl, 1942). Note the visual similarity between boundary layers for the $\alpha = 90°$ cases (left plots in Fig. 3.5 and 3.6), and the dissimilarity at $\alpha = 15°$ (right plots in Fig. 3.5 and 3.6). As α decreases, a broadening of scales for the anabatic flow cases occurs with significant thickening of the LLJ region (negative up-slope velocity), likely induced by the convective type regime characterizing the flow at small sloping angles. Katabatic flows are instead characterized by a strong static stability at small sloping angles (see Fig. 3.5), which damps positive slope-normal velocity fluctuations, thus maintaining the LLJ relatively close to the wall and reducing the overall mixing of momentum and buoyancy in the near wall regions. Further, the strong stability induced by the imposed surface buoyancy in the katabatic flow regime at small α results in apparent laminarisation of the LLJ.

3.5 Mean flow and turbulence characteristics

3.5.1 Mean flow

Mean profiles of kinematic momentum $\langle u \rangle$ and buoyancy $\langle b \rangle$ are displayed in Fig. 3.7 for anabatic and katabatic runs at the highest $Re = 4.6 \times 10^5$. The profiles here qualitatively resemble those obtained from the Prandtl solution (Prandtl, 1942). The most important features are a peak velocity (u_j) in the near wall regions – identifying the LLJ – and by a return flow capping both the TBL and DBL. As previously observed in Fedorovich and Shapiro (2009b), profiles are sensitive to the sloping angle (α). The smaller the α, the larger the difference between the anabatic and the corresponding katabatic flow solution. In contrast to the katabatic case, the anabatic regime is characterized by a sensitivity of both z_j and u_j to α. As α decreases, a simultaneous increase in the height of the LLJ (z_j) and a reduction in u_j are observed. This behavior is related to the strengthening of the slope-normal component

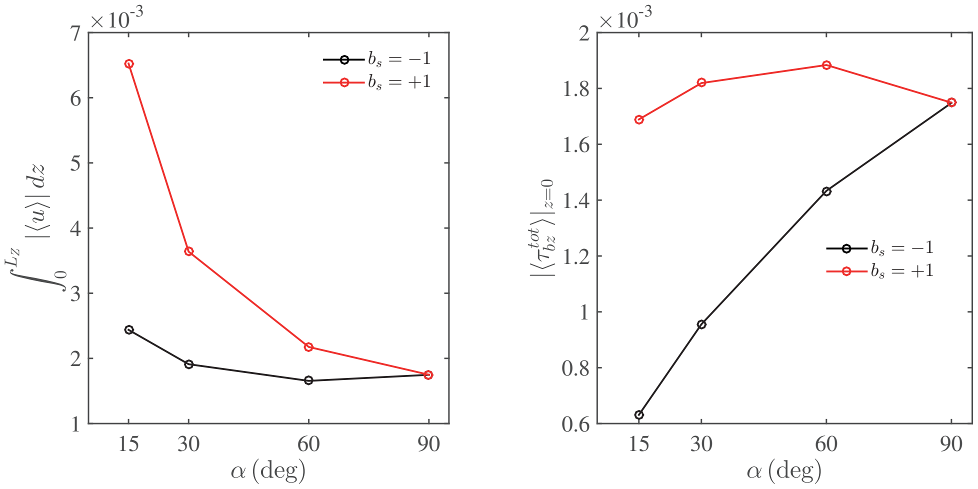

Figure 3.8 – Absolute value of the slope-normal integrated horizontal momentum flux (left) and absolute value of the mean surface buoyancy flux (right) as a function of α for the highest $Re = 4.6 \times 10^5$ case.

of the imposed (positive) surface buoyancy as α decreases, which works against the stable background stratification and enhances both TKE production and the slope-normal flux of momentum in the near wall regions, leading to well mixed profiles of velocity and buoyancy, in agreement with findings of Fedorovich and Shapiro (2009b).

Another apparent difference between the katabatic and anabatic flow solutions is the sensitivity of the TBL and DBL height to the sloping angle α. The z_r delineating the distance from the wall where the return flow reaches its peak velocity is inversely proportional to α in both katabatic and anabatic flow conditions. However, variations in the anabatic regime are arguably larger as apparent from Fig. 3.7. For instance, at $\alpha = 90°$ the two regimes are characterized by a similar z_r but at a lower $\alpha = 15°$, z_r of the anabatic flow solution is roughly three times larger than its katabatic counterpart. The slope-normal integrated horizontal momentum flux in the anabatic flow regime also shows a sensitivity to the α parameter, roughly varying by a factor of three across the range of α values considered here (see Fig. 3.8).

Such behavior may be better understood when slope-normal integrating Eqs. 3.12 and 3.13. Since $\langle \tau_{bz}^{tot}(z \to \infty) \rangle = 0$, this integration results in

$$\int_0^{L_Z} \langle u \rangle dz = -\frac{\langle \tau_{bz} \rangle|_{z=0}}{\sin\alpha}, \tag{3.14}$$

where $\langle \tau_{bz} \rangle|_{z=0}$ is the surface buoyancy flux and $\int_0^{L_Z} \langle u \rangle dz$ is the slope-normal integrated horizontal flux of momentum. Variations of $\int_0^{L_Z} |\langle u \rangle| dz$ and $|\langle \tau_{bz} \rangle|_{z=0}$ as a function of the α parameter are displayed in Fig. 3.8, where absolute values are considered to contrast the two flow regimes. The anabatic flow solution is characterized by a relatively stronger mixing induced by the positive (imposed) surface buoyancy b_s, resulting in a weaker sensitivity of the

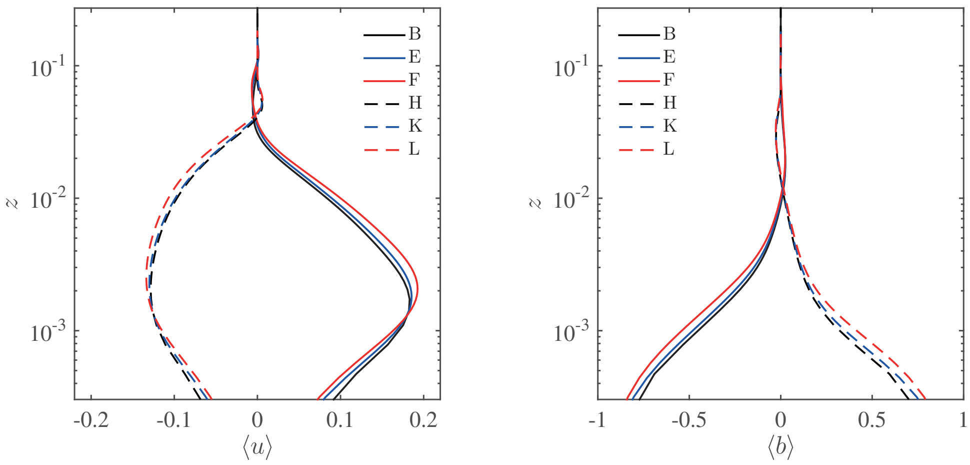

Figure 3.9 – Sensitivity of the stream-wise velocity $\langle u \rangle$ (left) and buoyancy $\langle b \rangle$ (right) on the Re parameter, for katabatic (solid lines) and anabatic (dashed lines) flow regimes at $\alpha = 60°$.

surface buoyancy flux to α. For this setup, the slope-normal integrated horizontal momentum flux is proportional to $\sin^{-1}(\alpha)$. In the katabatic flow regime, a relatively steeper drop in the surface buoyancy flux $\langle \tau_{bz} \rangle|_{z=0}$ is noted as α increases, proportional to $\sin^{-1}(\alpha)$, thus resulting in an approximately constant slope-normal integrated horizontal momentum flux. Such a behavior is justified when noting that as the sloping angle decreases, the normal-to-slope b_s component ($b_s \cos(\alpha)$) increases, yielding a stronger inversion layer in the near surface regions, which damps turbulent fluctuations and the related (turbulent) fluxes of buoyancy and momentum.

As α decreases, the along-slope component of the imposed surface buoyancy b_s also decreases, but in conjunction with it, the effects of the background stratification becomes weaker, so it is more likely that this reduction in $\langle \tau_{bz} \rangle|_{z=0}$ is related the strong inversion layer that forms in the near surface regions, rather than to a decrease of the imposed along-slope forcing. In Fedorovich and Shapiro (2009b) anabatic and katabatic flow solutions were found to share a similar flow depth (z_r), inversely proportional to the sloping angle α, which is in contrast with the proposed DNS results. This mismatch is likely related to the constant surface buoyancy flux that was applied as boundary condition in the Fedorovich and Shapiro (2009b) study, which, given the integral constraint 3.14, forces the slope-normal integrated horizontal momentum flux to match between anabatic and related katabatic flow regimes.

The sensitivity of anabatic and katabatic flow solutions to variations in Re is displayed in Fig. 3.9 for $\alpha = 60°$. For the (narrow) Re range considered, $(z_j, u_j, z_r) \propto Re^{-1}$. The observed behavior is justified based on the inverse proportionality of the normalized surface buoyancy flux and Re, as apparent from Fig. 3.10. Increasing Re results in less energy that is fed into the fluid system through the imposed surface buoyancy (b_s), resulting in a weaker (normalized) velocity profile.

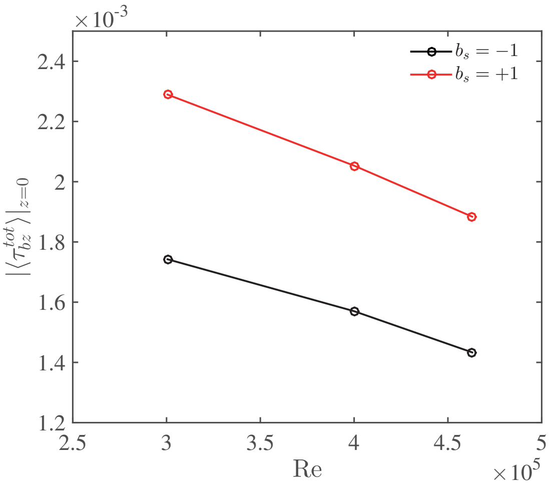

Figure 3.10 – Absolute value of the averaged surface buoyancy flux as a function of *Re* for anabatic (red line) and katabatic (black line) flow regimes at $\alpha = 60°$ (simulations B,E,F, and H,K,L respectively).

3.5.2 TKE and buoyancy variance

Slope-normal variations of TKE and of buoyancy variance $\langle b'b' \rangle$ are featured in Fig. 3.11. In the katabatic regime, TKE exhibits a decrease in magnitude approximately proportional to α with a TKE peak located between $3z_j$ and $5z_j$. The proportionality of TKE to α in the katabatic flow solution is clearly related to the strengthening of the normal-to-wall component of the surface buoyancy, resulting in a stronger stable stratification. TKE profiles from the anabatic flow solution are again more sensitive to α when compared to their katabatic counterparts. The location of the TKE peak in the anabatic regime is inversely proportional to α, but its magnitude shows no monotonic behavior, thus suggesting a more complex α-dependence. Furthermore, the TKE in the neighborhood of the LLJ is characterized by a modest positive slope-normal gradient (i.e. is approximately constant).

The buoyancy variance $\langle b'b' \rangle$ peaks in the near wall regions for both flow regimes where strong buoyancy gradients occur, in agreement with Fedorovich and Shapiro (2009b). Variations in $\langle b'b' \rangle$ as a function of α in the below-LLJ region are significant only for the katabatic flow regime, with peak value and its location being directly and inversely proportional to the α parameter respectively. The above-LLJ regions of the boundary layer are characterized by a rapid decay in $\langle b'b' \rangle$, most evident for the katabatic flow regime. The anisotropic nature of turbulence in slope flows is apparent from Fig. 3.12, where normal stress components $\langle u'u' \rangle$, $\langle v'v' \rangle$, and $\langle w'w' \rangle$ are inter-compared. The boundary layer character of the system is apparent with the wall providing an effective damping of the $\langle w'w' \rangle$ central moment, in both anabatic and katabatic flow regimes. It is to be noted that self-similarity in $\langle w'w' \rangle$ profiles emerge as α is varied for both wind regimes. This behavior is related to the expected dependence of $\langle w'w' \rangle$ on the effective stratification (background + perturbation), given that buoyancy has direct control on slope-normal velocity fluctuation w'. Because of this, as α decreases, the

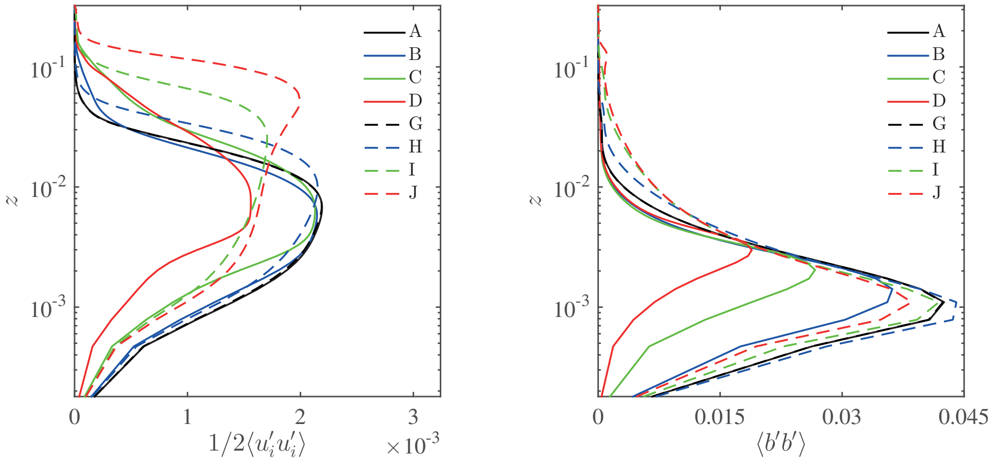

Figure 3.11 – Comparison of turbulent kinetic energy ($1/2\langle u_i' u_i' \rangle$) (left) and buoyancy variance ($\langle b' b' \rangle$) (right) for the katabatic (solid lines) and the anabatic flow (dashed lines) regimes at the highest $Re = 4.6 \times 10^5$ cases.

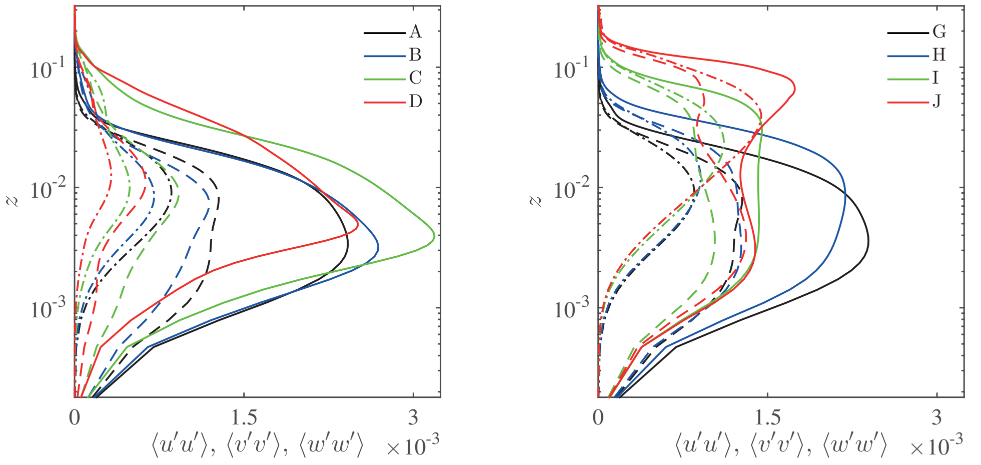

Figure 3.12 – Normal stress components $\langle u' u' \rangle$ (solid lines), $\langle v' v' \rangle$ (dashed lines) and $\langle w' w' \rangle$ (dot-dashed lines) for the katabatic (left) and the anabatic (right) flow regimes at the highest $Re = 4.6 \times 10^5$ cases.

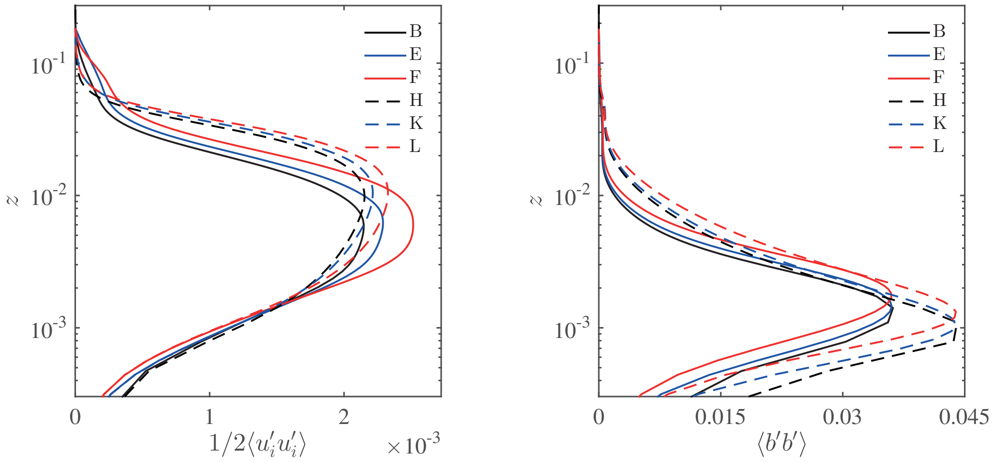

Figure 3.13 – Sensitivity of the turbulent kinetic energy ($(1/2)\langle u_i' u_i' \rangle$) (left) and buoyancy variance ($\langle b' b' \rangle$) (right) to the Re parameter for katabatic (solid lines) and anabatic (dashed lines) flow regimes at $\alpha = 60°$.

turbulence characterizing katabatic flows becomes more anisotropic (the strong, effective, stable stratification damps $\langle w' w' \rangle$) in contrast to its anabatic counterpart, where the interplay between the background stable stratification and the positive surface buoyancy leads to an isotropisation of turbulent motions. The observed trend here supports the recently proposed scaling of Shapiro and Fedorovich (2014) based on the assumption of large scale separation between slope-normal and slope-parallel motions populating katabatic flows, which might indeed be effective at small sloping angles.

The sensitivity of normalized TKE and normalized buoyancy variance ($\langle b' b' \rangle$) to Re is presented in Fig. 3.13 for both flow regimes. Commencing with below the LLJ regions, here both TKE and $\langle b' b' \rangle$ are proportional to Re, despite the reduction in the overall energy that is fed into the system as Re increases. This result is directly related to molecular dissipation, which is effective in damping the small-scale near-wall turbulence. In the outer regions of the flow we instead have a counterintuitive behavior, i.e. $(TKE, \langle b' b' \rangle) \propto Re^{-1}$. This is directly linked to the chosen normalization, since the (normalized) energy of the system is inversely proportional to Re, and to the fact that molecular dissipation does not directly affect the large-scale outer-layer turbulent structures.

3.5.3 Momentum and buoyancy fluxes

Shear stresses and slope-normal buoyancy fluxes for the considered runs are displayed in Fig. 3.14. As observed in previous numerical and experimental studies (Axelsen and Dop, 2009b; Fedorovich and Shapiro, 2009a,b; Oldroyd et al., 2014; Grachev et al., 2015), the near-wall (below-LLJ) regions are characterized by a negative total momentum flux ($\langle \tau_{xz}^{tot} \rangle < 0$), on the other hand, the above-LLJ region, where velocity gradients are negative, is characterized by

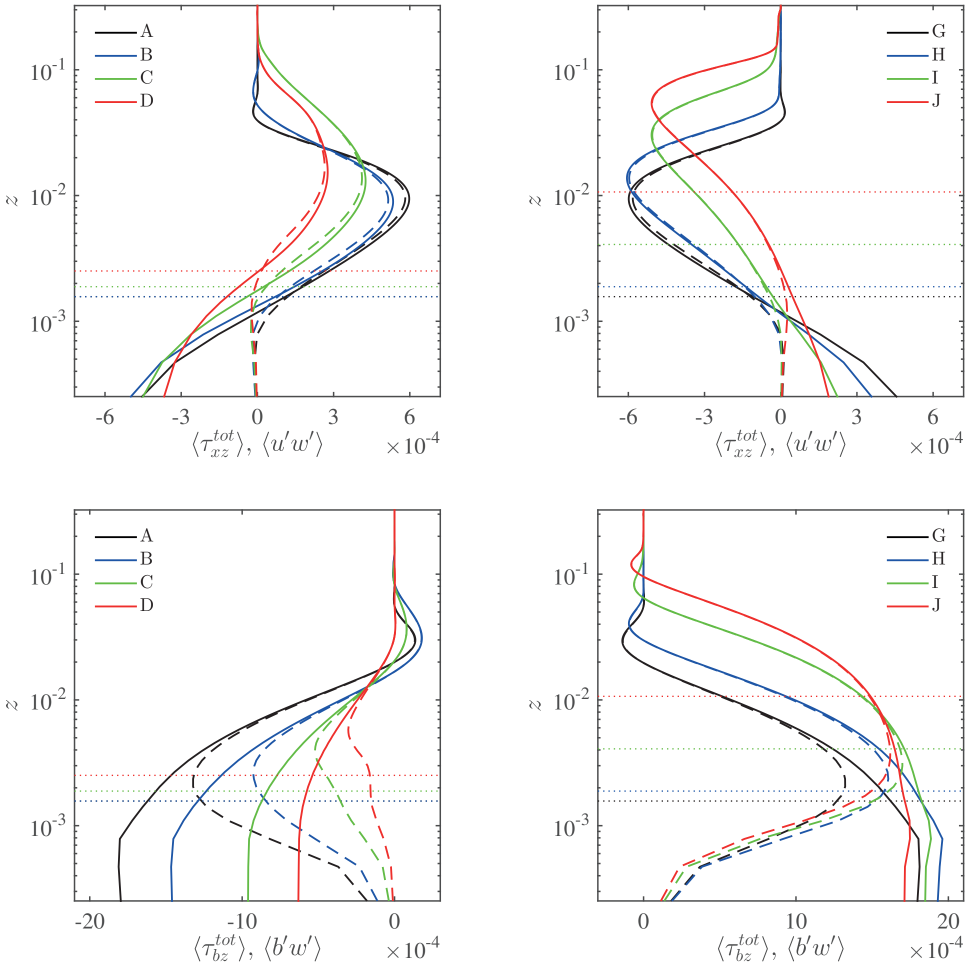

Figure 3.14 – Total (solid lines) and turbulent (dashed lines) momentum flux for the katabatic (top left) and the anabatic (top right) flow regimes, and total (solid lines) and turbulent (dashed lines) buoyancy slope-normal flux for the katabatic (bottom left) and the anabatic (bottom right) flow regimes. All cases are characterized by $Re = 4.6 \times 10^5$. We denote the total stream-wise momentum slope-normal flux as $\langle \tau_{xz}^{tot} \rangle \equiv (1/Re)(d\langle u \rangle / dz) + \langle u'w' \rangle$ and the total slope-normal buoyancy flux as $\langle \tau_{bz}^{tot} \rangle \equiv (1/(RePr))(d\langle b \rangle / dz) + \langle b'w' \rangle$. The height of the LLJ (z_j) is displayed (dotted line) for the different cases to provide a reference.

a positive total momentum flux. Interestingly, the zero crossings in the mean profiles of $\langle b\rangle$ and $\langle u\rangle$ are not precisely co-located with the extrema of the total fluxes. At the LLJ location for instance, a positive (negative) total slope-normal momentum flux for the katabatic (anabatic) flow regime are observed. As discussed in the following, this will result in consistent counter gradient fluxes and in negative TKE production rates in the neighborhood of the LLJ. In the near wall regions, total momentum fluxes $\langle\tau_{xz}^{tot}\rangle|_{z=0}$ are insensitive to variations in α for both flow regimes. This insensitivity is partly justified by the fact that slope-normal momentum transport in the below-LLJ regions is dominated by molecular diffusion (at all the considered α) and is not affected by stability effects despite the finite TKE. This finding hints that turbulent motion in the below-jet regions are 'inactive' in the Townsend (1956) sense and contribute to the overall TKE but do not appreciably contribute to the turbulent slope-normal transport of momentum.

Near wall surface buoyancy fluxes in the anabatic flow regime are also insensitive to variations in α, despite the non-negligible turbulent component. This is likely due to the interplay between the positive surface buoyancy and the background stable stratification (whose magnitude is proportional to α), which compensate each other. Conversely, a stark α dependency characterizes total surface buoyancy fluxes in the katabatic flow regime, as apparent from Fig. 3.14. This again can be related to the combined effects of the background stable stratification and the imposed surface buoyancy: as the sloping angle decreases, the increasing strength of the inversion layer progressively damps w', resulting in a reduction of the turbulent buoyancy flux $\langle b'w'\rangle$.

3.6 Budgets of mean and turbulent kinetic energy

3.6.1 The mean kinetic energy budget

The budget equation for MKE, assuming horizontal homogeneity ($\partial\langle\cdot\rangle/\partial x = \partial\langle\cdot\rangle/\partial y = 0$) and no subsidence ($\langle w\rangle = 0$), is derived by multiplying the equation for $\langle u_i\rangle$ by $\langle u_i\rangle$. The derivation subject to the aforementioned assumption leads to

$$\frac{1}{2}\frac{\partial(\langle u_i\rangle\langle u_i\rangle)}{\partial t} = \langle u_i' w'\rangle\frac{\partial\langle u_i\rangle}{\partial z} - \langle u_i\rangle\langle b\rangle\sin(\alpha) - \frac{\partial(\langle u_i\rangle\langle u_i' w'\rangle)}{\partial z} + \frac{1}{Re}\langle u_i\rangle\frac{\partial^2\langle u_i\rangle}{\partial z^2}, \qquad (3.15)$$

where the left hand side of Eq. 3.15 is the storage term of MKE, $\mathscr{P}_s \equiv \langle u_i' w'\rangle\frac{\partial\langle u_i\rangle}{\partial z}$ denotes shear production / destruction of MKE, $\mathscr{P}_b \equiv -\langle u_i\rangle\langle b\rangle\sin(\alpha)$ denotes buoyancy production / destruction of MKE, transport of MKE by turbulent motions is $\mathscr{T}_t \equiv -\frac{\partial(\langle u_i\rangle\langle u_i' w'\rangle)}{\partial z}$ and dissipation of MKE by viscous diffusion is $\mathscr{E} \equiv \frac{1}{Re}\langle u_i\rangle\frac{\partial^2\langle u_i\rangle}{\partial z^2}$. When the time-averaging is over a sufficiently long enough period (as shown here), then $\partial\langle\cdot\rangle/\partial t = 0$, and the storage term can be neglected.

The normalized MKE budget terms for the considered anabatic and katabatic runs are displayed in Fig. 3.15. Note that the choice of $\hat{b}_s^{\,2}\hat{N}^{-1}$ as a normalizing factor is not critical for the

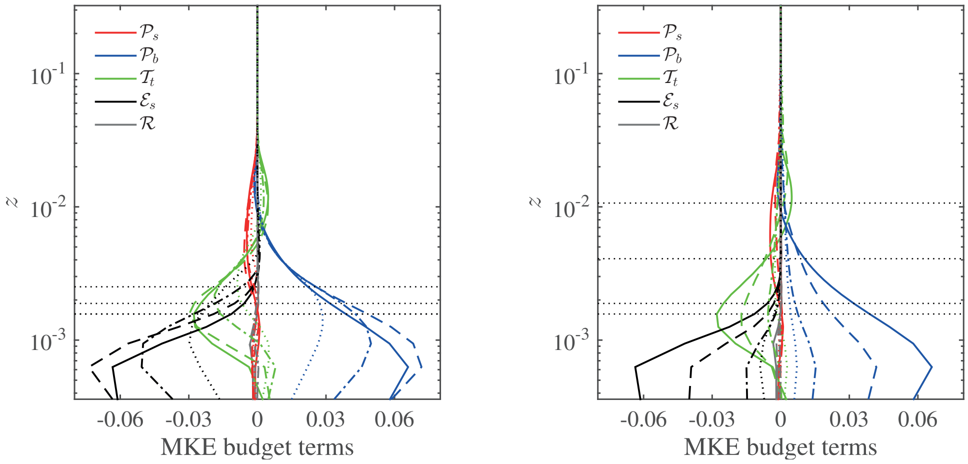

Figure 3.15 – MKE budget for the katabatic (left) and the anabatic (right) flow regimes at $Re = 4.6 \times 10^5$. Profiles corresponding to $\alpha = 90°, 60°, 30°$ and $15°$ (simulations A, B, C, D for the katabatic regime; G, H, I, J for the anabatic regime) are denoted with solid, dashed, dot-dashed and dotted lines respectively. The location of the LLJ is highlighted with dotted black lines for the various runs, to provide a reference height (note that as α decreases the LLJ height increases, and note also that z_j is the same for the $\alpha = 90°$ and the $\alpha = 60°$ runs). All terms are normalized by $\hat{U}^3\,\hat{L}^{-1} \equiv \hat{b_s}^2\,\hat{N}^{-1}$.

interpretation of the budget, since the relative magnitude of terms is unchanged. As expected, the mean source of MKE is from buoyancy production ($\mathscr{P}_b$), which peaks in the below-jet regions, and is characterized by a gradual decrease throughout the boundary layer. In the outer regions of the flow, $\mathscr{P}_b$ becomes a sink of MKE in both flow regimes starting from the zero crossing of $\langle b \rangle$ and up to the start of the return flow region. Here, energy is provided by turbulent transport ($\mathscr{T}_t$), which balances dissipation ($\mathscr{E}$) and buoyant production ($\mathscr{P}_b$). At the wall, buoyant production is overcome by dissipation for both upslope and downslope flows, and transport from turbulent motions is responsible to close the MKE budget. $\mathscr{T}_t$ acts as a sink of MKE in the highly energetic LLJ regions, displacing it toward the wall to balance dissipation, and in the outer layer of the flow.

In both up-slope and down-slope flows, shear production of MKE ($\mathscr{P}_s$) acts as a sink of MKE in the above-jet regions, draining energy from the mean flow and transferring it to turbulence through the classical energy cascade process. Interestingly, for both regimes and sloping angles, the below-jet regions are characterized by $\mathscr{P}_s > 0$, highlighting a region of global energy backscatter, i.e. energy is transferred from the turbulent eddies to the mean flow. Forward scatter is known to be mainly caused by vortex stretching by the strain rate, whereas backscatter indicates vortex compression by the strain rate, which is not commonly observed in canonical wall bounded flows.

3.6.2 The turbulent kinetic energy budget

Under the assumptions leading to Eq. 3.15, the budget equation for the second central velocity moment $(1/2)\langle u_i' u_i' \rangle$ (the so-called TKE budget equation), is given as

$$\left(\frac{1}{2}\right)\frac{\partial \langle u_i' u_i' \rangle}{\partial t} = -\langle u_i' w' \rangle \frac{\partial \langle u_i \rangle}{\partial z} + \delta_{3i} \langle b' u_i' \rangle \cos(\alpha) - \delta_{1i} \langle b' u_i' \rangle \sin(\alpha) - \frac{1}{2}\frac{\partial \langle u_i' u_i' w' \rangle}{\partial z} - \frac{\partial \langle \pi' w' \rangle}{\partial z} + \frac{1}{2}\nu \frac{\partial^2 \langle u_i' u_i' \rangle}{\partial z^2} - \nu \langle \frac{\partial u_i' \partial u_i'}{\partial x_j^2} \rangle, \quad (3.16)$$

where $\left(\frac{1}{2}\right)\frac{\partial \langle u_i' u_i' \rangle}{\partial t}$ is the storage of TKE term, shear production of TKE is denoted as $P_s \equiv -\langle u_i' w' \rangle \frac{\partial \langle u_i \rangle}{\partial z}$, buoyant production / destruction of TKE is composed of two terms, namely $P_{b,1} \equiv \delta_{1i} \langle b' u_i' \rangle \sin(\alpha)$ and $P_{b,3} \equiv \delta_{3i} \langle b' u_i' \rangle \cos(\alpha)$, turbulent transport of TKE is $T_t \equiv -\frac{1}{2}\frac{\partial \langle u_i' u_i' w' \rangle}{\partial z}$, pressure transport $T_p \equiv -\frac{\partial \langle \pi' w' \rangle}{\partial z}$, viscous diffusion of TKE is $T_\nu \equiv \frac{1}{2}\nu \frac{\partial^2 \langle u_i' u_i' \rangle}{\partial z^2}$ and viscous dissipation $\epsilon \equiv -\nu \langle \frac{\partial u_i' \partial u_i'}{\partial x_j^2} \rangle$. With regard to the buoyancy production / destruction terms, $P_{b,1}$ accounts for production / destruction of TKE due to cross-correlation between along-slope velocity (u) and buoyancy (b), whereas $P_{b,3}$ accounts for production / destruction of TKE due to cross-correlation between normal-to-slope velocity (w) and buoyancy (b). The splitting of the buoyancy production term, which is commonly understood to act in the slope-normal direction only, is clearly a result of the inclined reference system that is adopted to describe the evolution of the system.

TKE budget terms for the considered runs at $Re = 4.6 \times 10^5$ are displayed in Fig. 3.16. Shear production (P_s) appears with opposite signs in the budgets of MKE and TKE as expected; it is the net transfer from MKE to TKE as the result of their interactions that often sustains turbulence in classical boundary layer theory on flat slopes. For both wind regimes, P_s is characterized by two positive peaks, one in the above jet regions and one in the very near wall regions, and by a negative region just below the LLJ, where global energy backscatter occurs. Occurrence of negative P_s indicates local counter-gradient turbulent momentum flux. Simulations at higher Re and a spectral analysis are needed for definitive conclusions about the scales experiencing this energy backscatter. Nevertheless, the current results suggest that closure models based on an imposed mixing length assumption, such as Smagorinsky-type for instance (Smagorinsky, 1963; Germano et al., 1991; Lilly, 1992; Meneveau et al., 1996; Porté-Agel et al., 2000; Bou-Zeid et al., 2005), might not be appropriate for such flows as they cannot account for energy backscatter. In both katabatic and anabatic flow regimes dissipation (ϵ) peaks at the wall, is approximately constant in the core of the flow, and then decreases to zero in the return flow region. The $P_{b,3}$ is a sink of TKE for the katabatic regime and a source of TKE for the anabatic regime, as expected. In the anabatic regime $P_{b,3} \approx 0$ at $\alpha = 90$ (deg), but gains considerable importance (as a TKE source term) in the overall budget as α decreases. For instance, considering the $\alpha = 15$ (deg) run, $P_{b,3}$ alone overcomes TKE dissipation in the core of the LLJ. To the contrary, the modest magnitude of $P_{b,3}$ highlights

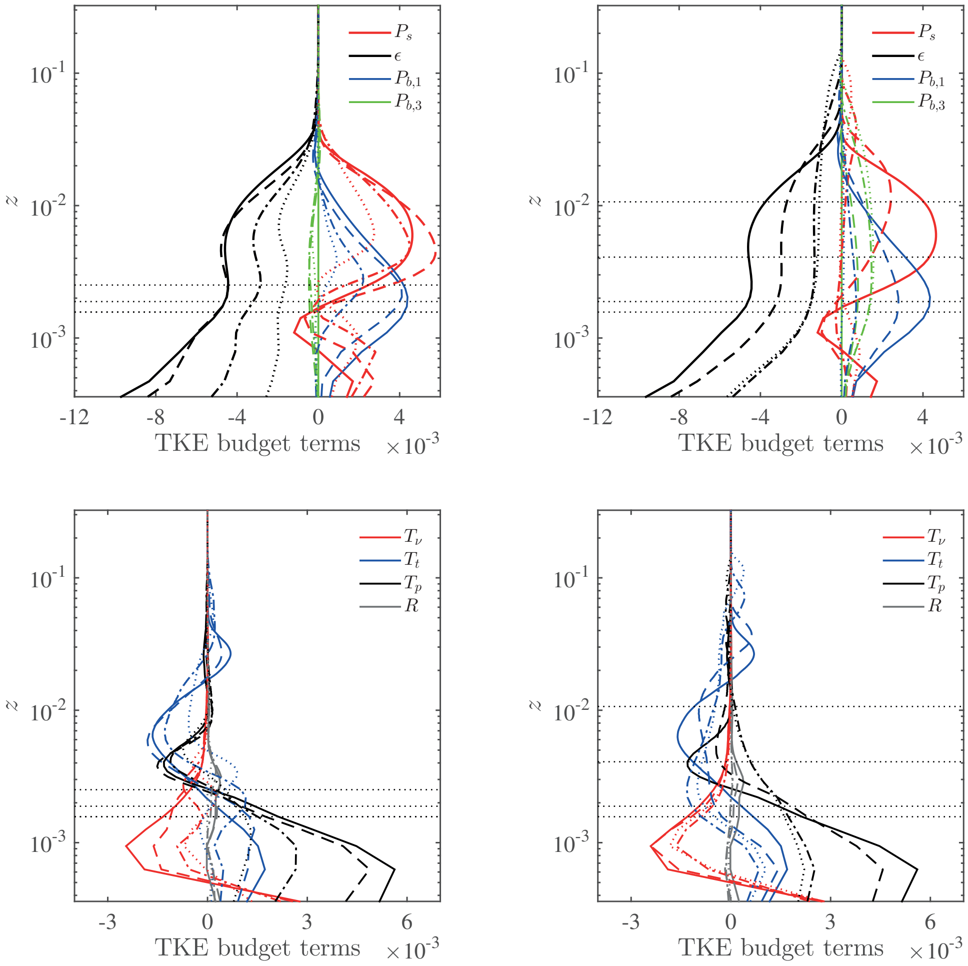

Figure 3.16 – Comparison of TKE budged terms for katabatic (left) and anabatic (right) flow regimes at $Re = 4.6 \times 10^5$. Production and destruction terms (top) have been separated from transport and residual terms (bottom). The $\alpha = 90°, 60°, 30°$ and 15° cases (simulations A, B, C, D for the katabatic regime; G, H, I, J for the anabatic regime) are denoted with solid, dashed, dot-dashed and dotted lines respectively. The location of the LLJ is highlighted with dotted black lines for the various runs to facilitate interpretation (note that $\alpha \propto z_j$). All terms are normalized by $\hat{U}^3 \hat{L}^{-1} \equiv \hat{b}_s^2 \hat{N}^{-1}$.

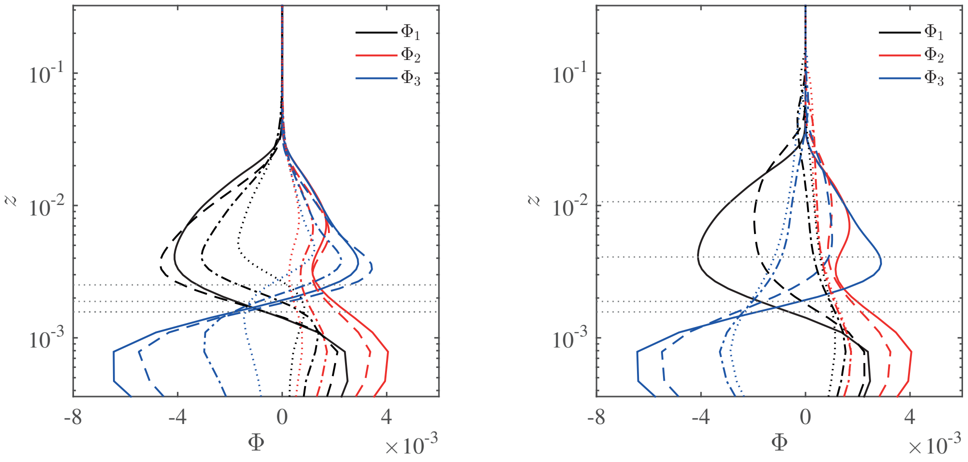

Figure 3.17 – Comparison of return-to-isotropy terms for katabatic (left) and anabatic (right) flow regimes. We denote $\Phi_1 \equiv \langle p' \frac{\partial u'}{\partial x} \rangle$, $\Phi_2 \equiv \langle p' \frac{\partial v'}{\partial y} \rangle$, and $\Phi_3 \equiv \langle p' \frac{\partial w'}{\partial z} \rangle$. The location of the LLJ is once again highlighted with dotted grey lines and the $\alpha = 90°, 60°, 30°$ and $15°$ runs (simulations A, B, C, D for the katabatic regime; G, H, I, J for the anabatic regime) are denoted with solid, dashed, dot-dashed and dotted lines respectively. All terms are normalized by $\hat{U}^3 \hat{L}^{-1} \equiv \hat{b}_s^2 \hat{N}^{-1}$.

how buoyant destruction of TKE is not the primary mechanism though which buoyancy acts to suppress turbulence in katabatic flows. Following the same reasoning of Shah and Bou-Zeid (2013) (where stability effects on the Ekman layer were studied through DNS), it is argued here that negative buoyancy directly reduces $\langle w' w' \rangle$, thus reducing local production of $\langle u' w' \rangle$. A reduction in $\langle u' w' \rangle$ would ultimately results in the observed decrease in $\langle P_s \rangle$ and related TKE magnitude. $P_{b,1}$ is the major source of TKE at the LLJ for the katabatic flow regime at all the considered α. On the other hand, in the anabatic flow regime $P_{b,3}$ overcomes $P_{b,1}$ as α decreases, becoming the leading buoyant production term. Overall, the sum of production terms $(P_s + P_{b,1} + P_{b,3})$ overcome dissipation in the above-jet regions (roughly up to $10 z_j$), and transport terms are responsible to dislocate this excess in TKE down towards the wall, and toward the outer regions of the flow. Turbulent transport (T_t) is a more effective carrier of TKE in the outer regions of the flow, whereas pressure fluctuations (T_p) are more effective in transporting TKE down toward the wall, to balance dissipation and viscous diffusion. The viscous diffusion term T_v resembles its pressure-driven boundary layer analog, where T_v is a sink of TKE in the buffer sublayer, and a source of TKE in the laminar sublayer, below $z^+ = 5$ (corresponding to $z = 5 \times 10^{-4}$ in current units).

The return-to-isotropy term (also known as pressure redistribution term) contracts to zero, and so vanishes from the TKE budget equation. However, such a term provides useful insights on the nature of turbulence if plotted for the single TKE budget components, as displayed in Fig. 3.17. The single components of the return-to-isotropy term (Φ_1, Φ_2, Φ_3) show a consistent behavior in the below-jet layer for all the considered sloping angles and flow regimes, redis-

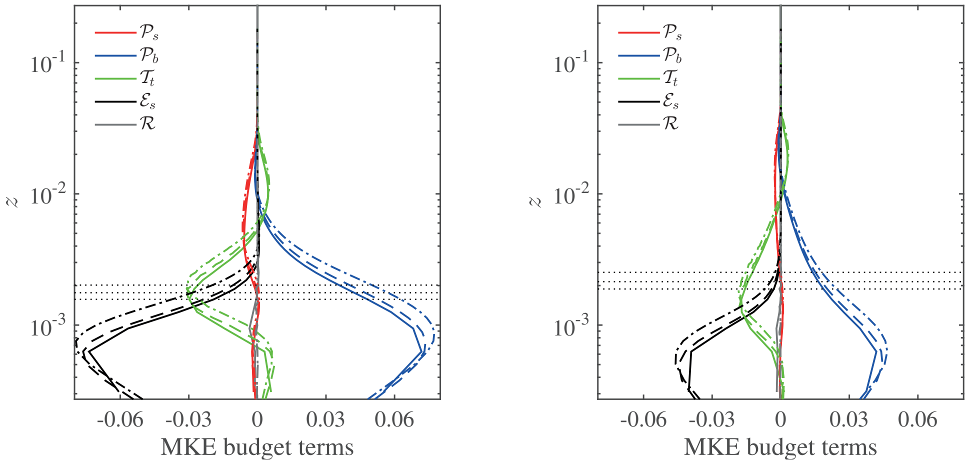

Figure 3.18 – Sensitivity of MKE budget terms to Re for the katabatic (left) and the anabatic (right) flow regimes at $\alpha = 60°$. Profiles corresponding to $Re = 3.0 \times 10^5, 4 \times 10^5$, and 4.6×10^5 (simulations B,E,F for the katabatic flow regime, and H,K,L for the anabatic flow regime) are denoted with dot-dashed, dashed, and solid lines respectively. The location of the LLJ is highlighted with dotted black lines for the various runs, to provide a reference height (note that as Re increases the LLJ height decreases). All terms are normalized by $\hat{U}^3 \hat{L}^{-1} \equiv \hat{b}_s^{\,2} \hat{N}^{-1}$.

tributing energy from the slope-normal component ($\langle w'w' \rangle$) to the horizontal components ($\langle u'u' \rangle$ and $\langle v'v' \rangle$ respectively). In the above-jet regions for the katabatic flow regime, a consistent energy redistribution among the TKE components are observed across the sloping angles, with energy being transferred from the stream-wise component ($\langle u'u' \rangle$) to the span-wise and slope-normal components ($\langle v'v' \rangle$ and $\langle w'w' \rangle$ respectively). For the anabatic flow regime, the return-to-isotropy terms in the above-jet regions highlight a transition in the dynamic and thermodynamic properties of turbulence as a function of α. When the two highest sloping angles are considered ($\alpha = 60°$ and $\alpha = 90°$), energy transfer is qualitatively equivalent to that characterizing the katabatic flow regime, i.e. the stream-wise variance feeds the span-wise and slope-normal variance components. For $\alpha = 15°$ and $\alpha = 30°$ the return-to-isotropy term becomes a sink for $\langle w'w' \rangle$ and a source for $\langle u'u' \rangle$ and $\langle v'v' \rangle$, indicative of energy transfer from the slope-normal TKE component, to the stream-wise and span-wise TKE components. This transition suggests that at low sloping angles, anabatic flow regimes are characterized by slope-normal elongated eddies, as apparent from the contours of Fig. 3.6, which feed $\langle u'u' \rangle$ and $\langle v'v' \rangle$ from $\langle w'w' \rangle$, the latter being directly sustained by the slope-normal component of the imposed surface buoyancy. Conversely, katabatic flow eddies are streamwise elongated and remove energy from $\langle u'u' \rangle$ – directly fed by the streamwise component of the imposed surface buoyancy – to transfer it to $\langle w'w' \rangle$ and $\langle v'v' \rangle$. Katabatic flows are thus characterized by a self-preservation of slope-normal velocity variance embedded in them through this energy redistribution despite the adverse role of stability.

The dependence of MKE budget terms on Re is highlighted in Fig. 3.18. The MKE profiles

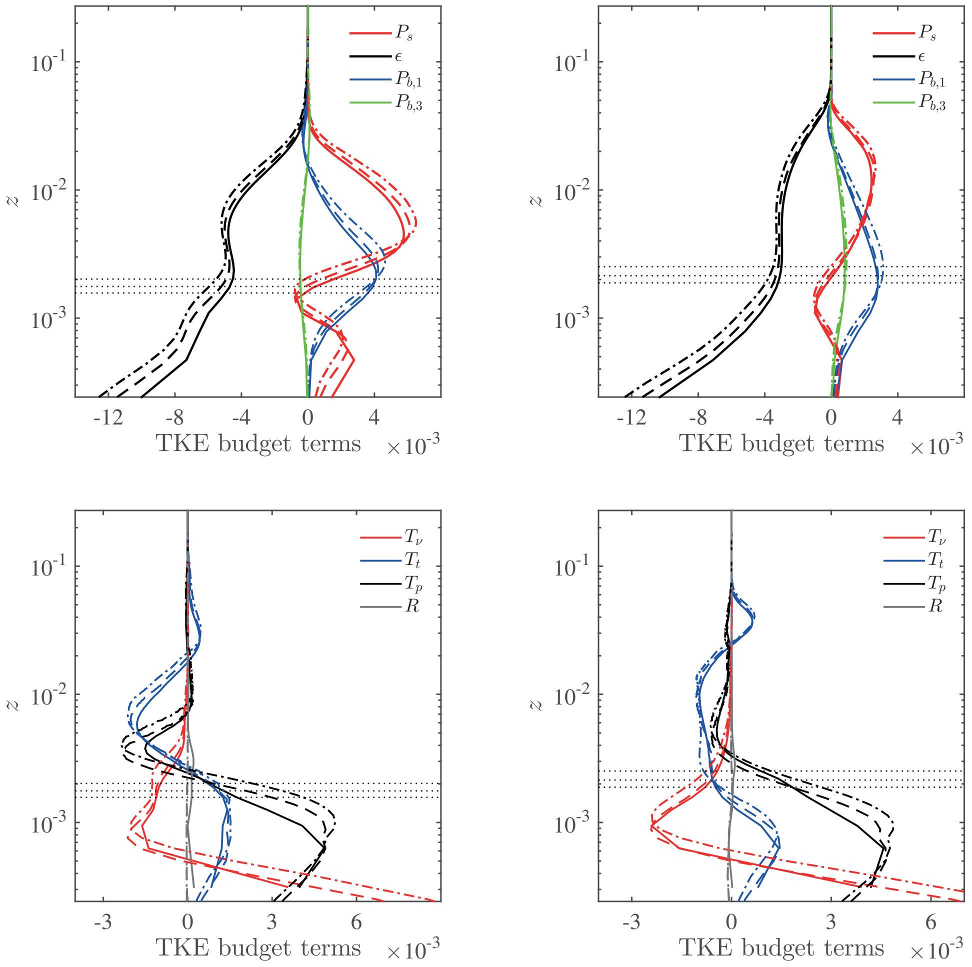

Figure 3.19 – Sensitivity of TKE budget terms to Re for the katabatic (left) and the anabatic (right) flow regimes at $\alpha = 60°$. Profiles corresponding to $Re = 3.0 \times 10^5, 4 \times 10^5$, and 4.6×10^5 (simulations F,E,B for the katabatic flow regime, and L,K,H for the anabatic flow regime) are denoted with dot-dashed, dashed, and solid lines respectively. The location of the LLJ is highlighted with dotted black lines for the various runs, to provide a reference height (note that as Re increases the LLJ height decreases). All terms are normalized by $\hat{U}^3\,\hat{L}^{-1} \equiv \hat{b_s}^2\,\hat{N}^{-1}$.

appear to be characterized by apparent self-similarity across the range of Re considered here for the outer layer. The absolute magnitude of terms weakens as Re increases and the characteristic scales also decrease. In contrast, in the LLJ and near-wall regions, $\mathscr{P}_s \propto Re$ underlying how more energy is locally converted to TKE as Re increases, as expected. TKE budget terms are also self-similar in the outer layer as apparent from Fig. 3.19. Near the wall, positive variations of Re result in a decreased magnitude of ϵ and T_v and in a strengthening of P_s. This suggests that at higher Re when compared to those considered herein, anabatic and katabatic flows might be characterized by a relatively important local TKE production rate in the below-LLJ regions, ultimately resulting in stronger TKE, and thus larger z_j and in well-mixed profiles of buoyancy and velocity. Such a region might well be the equivalent of the overlap (logarithmic) region in canonical wall bounded turbulent flows, which is not observed here, probably because of the relatively low Re.

Overall, current results suggest that the boundary layer characterizing slope flows at sloping angles $\alpha \geq 15°$ and $Re < 4.6 \times 10^5$ can be subdivided into three dynamically distinct regions, namely

1. an *outer layer*, corresponding approximately to the return flow region, where turbulent transport (T_t) is the main source of TKE and balances dissipation (ϵ);
2. an *intermediate layer*, capped below by the LLJ, where the sum of shear and buoyant production ($P_s + P_{b,1} + P_{b,3}$) overcomes dissipation (ϵ), and where turbulent and pressure transport terms (T_t, T_p) are a sink of TKE;
3. a *a wall layer*, $z \leq z_j$, where TKE is provided by turbulent and pressure transport terms, to balance viscous diffusion and dissipation.

3.7 Summary and conclusions

In this study DNS is used to characterize mean flow and turbulence of thermally-driven, stably-stratified flows along an uniformly cooled/heated sloping plate, within the conceptual framework of the Prandtl slope-flow model. The study focuses on the sensitivity of statistics to variations in both the sloping angle (α) and Reynolds number (Re), for fixed Prandtl number ($Pr = 1$). Four sloping angles are considered, ($\alpha = 15°, 30°, 60°$, and $90°$), and three Reynolds number ($Re = 3 \times 10^5, 4 \times 10^5$, and 4.6×10^5), where $Re = \hat{b}_s^2 \hat{\nu}^{-1} \hat{N}^{-3}$ is a modified Reynolds number, defined as the ratio between the energy production at the surface and the work against the background stratification and viscous forces. The study naturally complements the Fedorovich and Shapiro (2009b) analysis, where a similar range of sloping angle and Re is considered, but where the flow is forced using a constant surface buoyancy flux.

The initial transient is characterized by quasi-stationary oscillatory patterns in the mean variables, the normalized oscillation frequency being proportional to the sine of the sloping angle, in agreement with field observations of slope flows (Princevac et al., 2008; Monti et al., 2014).

The quality of the averaging operation is tested against a dynamic and a thermodynamic identity, readily derived from the equations of motions, that the average solution has to satisfy.

With respect to their basic features, the mean katabatic and anabatic flows appear similar to the corresponding laminar (Prandtl) counterparts. Turbulent anabatic and katabatic regimes are found to be structurally similar at high sloping angles, but to undergo a different transition as the sloping angle decreases, leading to stark statistical differences between the two flow regimes for the $\alpha \lessapprox 30°$ range. As α decreases, the negative surface buoyancy driving downslope flows leads to the formation of a strong surface inversion layer, leading to a progressive laminarisation of the solution in the below-jet regions and resulting in small variation in the integrated horizontal momentum flux, and to an overall small variability of mean profiles with respect to α. Anabatic flows on the other hand are characterized by a strengthening of TKE production and turbulent momentum fluxes as α decreases, by a significant α-dependence of the overall horizontal momentum flux, and by well mixed profiles of buoyancy and velocity, suggesting the presence of convective cells for $\alpha \lessapprox 30°$.

As in Fedorovich and Shapiro (2009b), we identified no region with constancy (even approximate) of any of the fluxes with distance from the wall.

Budget equations show how MKE is fed into the system through the imposed surface buoyancy, and turbulent fluctuations redistribute it from the lower edge of the jet toward the wall and toward the outer layer.

In addition, results show how the overall energy of the system is inversely proportional to Re, in the considered range of the parameter space, and how turbulent fluctuations gain importance in the below-jet regions as Re increases. Despite the low Reynolds range that was here considered, based on the observed trends, one might speculate about the existence of a (turbulent) overlap layer at higher Re, located in the below-LLJ region, separating the LLJ from the laminar sublayer.

Interestingly, a zone of global backscatter (energy transfer from the turbulent eddies to the mean flow) is consistently found in the below-jet regions, which highlights the presence of a complex interaction between dynamics and thermodynamics, and suggest that closure models based on a pre-set mixing length assumption might not be appropriate for the study of slope flows.

Further, analysis of the α-dependence of TKE budget terms suggests a subdivision of the boundary layer in three distinct regions for the considered range of Re and sloping angles: 1. an *outer layer*, roughly corresponding to the return flow region, where turbulent transport balances dissipation, 2. an *intermediate layer*, bounded below by the LLJ, where shear and buoyant production overcome dissipation, and turbulent and pressure fluctuations are responsible to relocate the excess of TKE down toward the wall and toward the outer layer, and

3. a *wall layer*, capped above by the LLJ, where pressure and turbulent transport balance dissipation and viscous diffusion of TKE.

Bibliography

J. D. Albertson and M. B. Parlange. Surface length scales and shear stress: implications for land-atmosphere interaction over complex terrain. *Water Resour Res*, 35(7):2121–2132, 1999a.

J. D. Albertson and M. B. Parlange. Natural integration of scalar fluxes from complex terrain. *Adv Water Resour*, 23(3):239–252, 1999b.

W. Anderson and C. Meneveau. Dynamic roughness model for large-eddy simulation of turbulent flow over multiscale, fractal-like rough surfaces. *J Fluid Mech*, 679:288–314, 2011.

S. Axelsen and H. Dop. Large-eddy simulation of katabatic winds. Part 1: Comparison with observations. *Acta Geophys*, 57(4):803–836, 2009a.

S. L. Axelsen and H. Dop. Large-eddy simulation of katabatic winds. Part 2: Sensitivity study and comparison with analytical models. *Acta Geophys*, 57(4):837–856, 2009b.

E. Bou-Zeid, C. Meneveau, and M. B. Parlange. A scale-dependent Lagrangian dynamic model for large eddy simulation of complex turbulent flows. *Phys Fluids*, 17(2):025105, 2005.

B. Burkholder, A. Shapiro, and E. Fedorovich. Katabatic flow induced by a cross-slope band of surface cooling. *Acta Geophys*, 57(4):923–949, 2009.

C. Canuto, M. Y. Hussaini, A. Quarteroni, and T. A. Zang. *Spectral methods*. Scientific Computation. Springer Berlin Heidelberg, Berlin, Heidelberg, 2006.

A. J. Chorin. Numerical solution of the Navier-Stokes equations. *Math Comput*, 22(104): 745–762, 1968.

P. C. Chu. An instability theory of ice-air interaction for the formation of ice edge bands. *J Geophys Res*, 92(C7):6966–6970, 1987.

J. Egger. Slope winds and the axisymmetric circulation over Antarctica. *J Atmos Sci*, 42(17): 1859–1867, 1985.

E. Fedorovich and A. Shapiro. Turbulent natural convection along a vertical plate immersed in a stably stratified fluid. *J Fluid Mech*, 636:41–57, 2009a.

E. Fedorovich and A. Shapiro. Structure of numerically simulated katabatic and anabatic flows along steep slopes. *Acta Geophys*, 57(4):981–1010, 2009b.

H. J. S. Fernando. Fluid dynamics of urban atmospheres in complex terrain. *Annu Rev Fluid Mech*, 42(1):365–389, 2010.

M. Germano, U. Piomelli, P. Moin, and W. Cabot. A dynamic subgrid-scale eddy viscosity model. *Phys Fluids*, 3(7):1760–1765, 1991.

A. A. Grachev, L. S. Leo, S. D. Sabatino, H. J. S. Fernando, E. R. Pardyjak, and C. W. Fairall. Structure of turbulence in katabatic flows below and above the wind-speed maximum. *Boundary-Layer Meteorol*, 2015.

J. W. Greuell, M. R. Broeke Van den, W. Knap, C. Reijmer, P. Smeets, , and I. Struijk. PASTEX: A glacio-meteorological experiment on the Pasterze (Austria). Technical report, Institute forMarine and Atmospheric Research, Utrecht University, Utrecht, 1994.

B. Grisogono and J. Oerlemans. Katabatic flow: Analytic solution for gradually varying eddy diffusivities. *J Atmos Sci*, 58(21):3349–3354, 2001.

B. Grisogono and J. Oerlemans. Justifying the WKB approximation in pure katabatic flows. *Tellus*, 54(5):453–462, 2002.

B. Grisogono, T. Jurlina, Ž. Večenaj, and I. Güttler. Weakly nonlinear Prandtl model for simple slope flows. *Q J R Meteorol Soc*, 141(688):883–892, 2015.

T. Haiden and C. D. Whiteman. Katabatic flow mechanisms on a low-angle slope. *J Appl Meteorol*, 44(1):113–126, 2005.

C. W. Higgins, M. B. Parlange, and C. Meneveau. Alignment trends of velocity gradients and subgrid-scale fluxes in the turbulent atmospheric boundary layer. *Boundary-Layer Meteorol*, 109(1):59–83, 2003.

M. Hultmark, M. Calaf, and M. B. Parlange. A new wall shear stress model for atmospheric boundary layer simulations. *J Atmos Sci*, 70(11):3460–3470, 2013.

A. G. G. Kravchenko and P. Moin. On the effect of numerical errors in large eddy simulations of turbulent flows. *J Comput Phys*, 131(2):310–322, 1997.

D. K. Lilly. A proposed modification of the Germano subgridscale closure method. *Phys Fluids*, 4(3):633–635, 1992.

H. Lu and F. Porté-Agel. A modulated gradient model for large-eddy simulation: Application to a neutral atmospheric boundary layer. *Phys Fluids*, 22(1):015109, 2010.

H. Lu and F. Porté-Agel. A modulated gradient model for scalar transport in large-eddy simulation of the atmospheric boundary layer. *Phys Fluids*, 25(1):015110, 2013.

L. Mahrt. Momentum balance of gravity flows. *J Atmos Sci*, 39(12):2701–2711, 1982.

L. Mahrt. Stratified atmospheric boundary layers and breakdown of models. *Theor Comput Fluid Mech*, 11:263–279, 1998.

L. Mahrt. Stably stratified atmospheric boundary layers. *Annu Rev Fluid Mech*, 46(July):23–45, 2013.

R. T. McNider. A note on velocity fluctuations in drainage flows. *J Atmos Sci*, 39(7):1658–1660, 1982.

C. Meneveau, T. S. Lund, and W. H. Cabot. A Lagrangian dynamic subgrid-scale model of turbulence. *J Fluid Mech*, 319:353–385, 1996.

E. R. Menold and K. Yang. Asymptotic solutions for unsteady laminar free convection on a vertical plate. *J Appl Mech*, 29(1):124–126, 1962.

R. N. Meroney, Y. Ohya, and D. E. Neff. Turbulence structure in a stratified boundary layer under stable conditions. *Boundary-Layer Meteorol*, 83(1):139–162, 1997.

P. Monti, H. J. S. Fernando, M. Princevac, W. C. Chan, T. A. Kowalewski, and E. R. Pardyjak. Observations of flow and turbulence in the nocturnal boundary layer over a slope. *J Atmos Sci*, 59(17):2513–2534, 2002.

P. Monti, H. J. S. Fernando, and M. Princevac. Waves and turbulence in katabatic winds. *Environ Fluid Mech*, 14(2):431–450, 2014.

J. Oerlemans. The atmospheric boundary layer over melting glaciers. In *Clear and Cloudy Boundary Layers*, pages 129–153. Royal Netherlands Academy of Arts and Sciences, 1998.

H. J. Oldroyd, G. G. Katul, E. R. Pardyjak, and M. B. Parlange. Momentum balance of katabatic flow on steep slopes covered with short vegetation. *Geophys Res Lett*, 41(13):4761–4768, 2014.

H. J. Oldroyd, E. R. Pardyjak, H. Huwald, and M.B. Parlange. Adapting tilt corrections and the governing flow equations for steep, fully three-dimensional, mountainous terrain. *Boundary-Layer Meteorol*, pages 1–27, 2015.

OpenMP Architecture Review Board. OpenMP application program interface version 4.0, 2013.

S. A. Orszag. Numerical methods for the simulation of turbulence. *Phys Fluids*, 12(12):II–250, 1969.

S. A. Orszag. Transform method for the calculation of vector-coupled sums: application to the spectral form of the vorticity equation. *J Atmos Sci*, 27(6):890–895, 1970.

S. A. Orszag and Y. H. Pao. Numerical computation of turbulent shear flows. In *Adv Geophys*, volume 18 of *Advances in Geophysics*, pages 225–236. Elsevier, 1975.

T. R. Parish and D. H. Bromwich. A case study of Antarctic katabatic wind interaction with large-scale forcing. *Mon Weather Rev*, 126(1):199–209, 1998.

Thomas R. Parish. On the role of Antarctic katabatic winds in forcing large-scale tropospheric motions. *J Atmos Sci*, 49(15):1374–1385, 1992.

S. B. Pope. *Turbulent flows*. Cambridge University Press, 2000.

F. Porté-Agel. A scale-dependent dynamic model for scalar transport in large-eddy simulations of the atmospheric boundary layer. *Boundary-Layer Meteorol*, 112(1):81–105, 2004.

F. Porté-Agel, C. Meneveau, and M. B. Parlange. A scale-dependent dynamic model for large-eddy simulation: application to a neutral atmospheric boundary layer. *J Fluid Mech*, 415: 261–284, 2000.

L. Prandtl. *Führer durch die strömungslehre*. Vieweg & Sohn, Braunschweig, 1942.

M. Princevac, J. C. R. Hunt, and H. J. S. Fernando. Quasi-steady katabatic winds on slopes in wide valleys: Hydraulic theory and observations. *J Atmos Sci*, 65(2):627–643, 2008.

G. Rampanelli, D. Zardi, and R. Rotunno. Mechanisms of up-valley winds. *J Atmos Sci*, 61(24): 3097–3111, 2004.

I. A. Renfrew. The dynamics of idealized katabatic flow over a moderate slope and ice shelf. *Q J R Meteorol Soc*, 130(598):1023–1045, 2004.

A. Renfrew, I. and S. Anderson, P. Profiles of katabatic flow in summer and winter over Coats Land, Antarctica. *Q J R Meteorol Soc*, 132(616):779–802, 2006.

U. Schumann. Large-eddy simulation of the up-slope boundary layer. *Q J R Meteorol Soc*, 116 (493):637–670, 1990.

A. Scotti, C. Meneveau, and D. K. Lilly. Generalized Smagorinsky model for anisotropic grids. *Physics of Fluids A: Fluid Dynamics*, 5(9):2306–2308, 1993.

S Shah and E Bou-Zeid. Direct numerical simulations of turbulent Ekman layers with increasing static stability: Modifications to the bulk structure and second-order statistics. *Bull Am Phys Soc*, 2013.

A. Shapiro and E. Fedorovich. Unsteady convectively driven flow along a vertical plate immersed in a stably stratified fluid. *J Fluid Mech*, 498:333–352, 2004a.

A. Shapiro and E. Fedorovich. Prandtl number dependence of unsteady natural convection along a vertical plate in a stably stratified fluid. *Int J Heat Mass Transf*, 47(22):4911–4927, 2004b.

A. Shapiro and E. Fedorovich. Katabatic flow along a differentially cooled sloping surface. *J Fluid Mech*, 571:149–175, 2007.

A. Shapiro and E. Fedorovich. A boundary-layer scaling for turbulent katabatic flow. *Boundary-Layer Meteorol*, 153(1):1–17, 2014.

E. D. Skyllingstad. Large-eddy simulation of katabatic flows. *Boundary-Layer Meteorol*, 106(2): 217–243, 2003.

J. Smagorinsky. General circulation experiments with the primitive equations. *Mon Weather Rev*, 91(3):99–164, 1963.

R. Temam. Une methode d'approximation de la solution des equations de Navier-Stokes. *Bull. Soc. Math. France*, 96:115–152, 1968.

A. A. Townsend. *The structure of turbulent shear flow*. 1956.

C. D. Whiteman. Observations of thermally developed wind systems in mountainous terrain. *Atmos Process over complex terrain, Meteor Monogr*, 45:5–42, 1990.

R. J. Zammett and A. C. Fowler. Katabatic winds on ice sheets: A refinement of the Prandtl model. *J Atmos Sci*, 64(7):2707–2716, 2007.

D. Zardi and C. D. Whiteman. Diurnal mountain wind systems. In *Mt Weather Res Forecast*, pages 35–119. Springer, 2013.

4 Large and very-large-scale motions in katabatic flows over steep slopes

Abstract

Evidence of Large and very-large-scale motions populating the outer layer in katabatic flows over steep slopes via direct numerical simulations (DNS) is presented. DNS are performed at a modified Reynolds number $Re_m = 967$, considering four sloping angles. Large coherent structures prove to be strongly dependent on the inclination of the underlying surface. Power spectra certify the presence of large-scale motions (LSMs), characterized by a streamwise extension in the order of the boundary layer thickness (δ). A second low-wavenumber mode characterizes pre-multiplied spectra and co-spectra when the slope angle is below 70 degrees, indicative of very-large-scale motions (VLSMs). VLSMs contribute to the turbulent kinetic energy and shear stress in the above-jet regions up to 30% and 45% respectively. Both LSMs and VLSMs are inactive in the near-wall regions. Results suggest that packets of hairpins, characterized by a head located upstream in the return flow region and by tails protruding downstream into the inner regions of the flow, concatenate in the streamwise direction to form LSMs and VLSMs. The hairpins are pumping fluid from the LLJ regions up in the outer layer, resulting in narrow bands of high momentum, flanked on each side by relatively broader regions of low momentum fluid (also induced by the hairpin legs), resulting in the observed LSMs and VLSMs statistical signatures.

4.1 Introduction

The structure of energy-containing turbulent motions populating the inner, overlap and outer layers of zero-pressure-gradient boundary layer flows has been extensively studied in the past decades, from both an experimental and a numerical perspective. Recent efforts have focused on the characterization of LSMs (Adrian et al., 2000; Ganapatisubramani et al., 2003; Del Lamo et al., 2004) and VLSMs (Kim and Adrian, 1999; Del Lamo et al., 2004; Guala et al., 2006; Balakumar and Adrian, 2007), given their crucial role in the transport of mass and momentum. Based on current understanding, LSMs are induced by packets of hairpins that align in the streamwise direction, and propagate with small velocity dispersion, pumping slow fluid from the lower regions, and resulting in patches of approximately uniform momentum. The alignment of hairpins and the self-regeneration properties (Zhou et al., 1999) justifies the high length-to-width ratios of observed two-point correlation maps (Kovasznay et al., 1970) and the highly energetic low-wavenumber peaks in the outer region pre-multiplied spectra (Guala et al., 2006). Typical lengh scales connected to LSMs are in the order of the boundary layer thickness δ.

VLSMs represent a relatively recent finding, and have been the focus of significant research. VLSMs have been studied in pipe flows (Kim and Adrian, 1999; Guala et al., 2006), channel flows (Del Lamo et al., 2004; Chung and McKeon, 2010), in laboratory boundary-layer flows at low to moderate Reynolds numbers (Tomkins and Adrian, 2003; Hutchins and Marusic, 2007b; Lee and Sung, 2011), and in atmospheric boundary-layer flows at very high Reynolds numbers (Hutchins et al., 2012; Shah and Bou-Zeid, 2014; Fang and Porté-Agel, 2015). Adrian (2007) and Marusic et al. (2010) have provided an excellent review of these structures including LSMs. Kim and Adrian (1999) examined pre-multiplied spectra for a turbulent pipe flow at $y^+ = yu_\tau \nu^{-1} = 132$, where u_τ is the friction-velocity and ν denotes the fluid kinematic viscosity, and interpreted their shapes as indicating a bimodal distribution in which the wavelengths at which the maxima occur represent VLSMs and LSMs. Guala et al. (2006) and Adrian (2007) have investigated the pre-multiplied power spectra of velocity fluctuations and determined criteria for distinguishing between VLSMs and LSMs in turbulent pipe flows, channel flows and boundary layers. They found that the maximum streamwise extent of LSMs is about 3δ (δ denotes the boundary layer height), and that the boundary that distinguishes VLSMs from LSMs and smaller motions is $k_x\delta = 2$ (k_x denotes a streamwise wavenumber), given the crossover in the co-spectra of the streamwise and vertical velocity components. Typical features of the VLSMs in canonical boundary-layer flows include peaks occurring at low frequencies in the pre-multiplied energy spectra, and highly streamwise-elongated, alternating low- and high-speed, meandering zones in the instantaneous velocity field. Further, it has been shown that VLSMs make significant contributions to the turbulent kinetic energy and to the Reynolds shear stress (Hutchins and Marusic, 2007a), have strong influence on the near-wall cycle (Hutchins and Marusic, 2007a,b; Mathis et al., 2009; Chung and McKeon, 2010), and coexist with large-scale counter-rotating roll modes of similar length (Marusic and Hutchins, 2008; Hutchins et al., 2012).

The turbulence-structure knowledge that results from studies of canonical boundary-layer flows can be easily transposed to study other types of boundary-layer flows, such as thermally driven stratified flows over sloping surfaces, the so-called “slope flows". Slope flows have been the focus of a significant study in the past two decades by the geophysical community, given the important role they play from a meteorological perspective (Whiteman, 1990, 2000; Fernando, 2010; Nadeau et al., 2013; Zardi and Whiteman, 2013; Sheridan et al., 2014; Monti et al., 2014; Oldroyd et al., 2014, 2015; Grachev et al., 2015) and because of their strong connection to the problem of melting glaciers and mass, momentum and energy balance in polar regions (Oerlemans and Vugts, 1993; Oerlemans, 1998; Parish and Bromwich, 1998; Renfrew, I.

and Anderson, P., 2006). Analytical solutions (Prandtl, 1942; Gutman, 1983; Grisogono and Oerlemans, 2001; Shapiro and Fedorovich, 2004a,b, 2007; Burkholder et al., 2009; Grisogono et al., 2015), observations (Oerlemans and Vugts, 1993; Oerlemans, 1998; Renfrew, I. and Anderson, P., 2006; Oldroyd et al., 2014) and numerical studies (Schumann, 1990; Skyllingstad, 2003; Axelsen and Dop, 2009; Fedorovich and Shapiro, 2009b,a; Shapiro and Fedorovich, 2014) have shown the structure of slope winds is characterized by a so-called low-level jet (LLJ) near the wall, and by a return flow in the upper regions of the boundary layer, thus significantly differing from canonical wall-bounded flows. The current study aims at bridging the gap between the relatively broad knowledge related to coherent structures populating classical boundary layer flows, and the lack of information on coherent structures in slope flows. A set of DNS is carried out, at a fixed Re number and considering different sloping angles, with the aim of characterizing turbulent motions in the outer layer (above-jet regions) of katabatic flows, and their interaction with the inner layer (below-jet regions). Given their theoretical and practical interest, the study will focus on the identification and characterization of the energetic scales populating the system, and on a qualitative and quantitative comparison between the slope flow system and canonical wall-bounded flows. Specific questions we aim at answering: 1. are slope flows characterized by LSMs and/or VLSMs? If so, 2. what is their structure? 3. What are the underlying mechanisms responsible for the formation of LSMs and VLSMs? And 4. do they interact with the inner regions of the flow?

4.2 Governing equations and simulation details

Considering a sloping surface immersed in a gravitationally stable environment and introducing a Cartesian coordinate system $(\hat{x}, \hat{y}, \hat{z})$ aligned in the direction of the slope, the three-dimensional Boussinesq equations for velocity, pressure and thermodynamic energy, read

$$\frac{\partial \hat{u}_i}{\partial \hat{t}} + \hat{u}_j \frac{\partial \hat{u}_i}{\partial \hat{x}_j} = -\frac{\partial \hat{\pi}}{\partial \hat{x}_i} + \hat{\nu} \frac{\partial^2 \hat{u}_i}{\partial \hat{x}_j^2} - \hat{b}(\hat{\mathbf{x}}, \hat{t})[\delta_{i1} \sin\alpha - \delta_{i3} \cos\alpha], \tag{4.1}$$

$$\frac{\partial \hat{u}_i}{\partial \hat{x}_i} = 0, \tag{4.2}$$

$$\frac{\partial \hat{b}}{\partial \hat{t}} + \frac{\partial \hat{u}_j \hat{b}}{\partial \hat{x}_j} = \hat{N}^2[\hat{u}_1 \sin\alpha - \hat{u}_3 \cos\alpha] + \hat{\kappa} \frac{\partial^2 \hat{b}}{\partial \hat{x}_j^2}. \tag{4.3}$$

where $\hat{(\cdot)}$ denotes a dimensional quantity, $\hat{t}$ (s) denotes time, $\hat{u}_i$ (m s^{-1}) are the velocity components in the three coordinate directions $(\hat{x}, \hat{y}, \hat{z})$ (m), $\hat{\pi} \equiv [\hat{p} - \hat{p}_\infty(\hat{x}, \hat{y}, \hat{z})]/\hat{\rho}_\infty$ (m s^{-2}) is the normalized deviation of pressure from the background hydrostatic value, $\hat{\rho}_\infty$ (kg m^{-3}) is a reference constant density, $\hat{b}$ (m s^{-2}) denotes the buoyancy variable, α (rad) is the slope angle, $\hat{N}$ (Hz) is the environmental buoyancy frequency (assumed constant), and $\hat{\nu}$ (m^2 s^{-1}) and $\hat{\kappa}$ (m^2 s^{-1}) are the kinematic molecular viscosity and diffusivity coefficients. Throughout the study we assume $Pr = 1$, i.e. $\hat{\kappa} = \hat{\nu}$, and neglect rotational effects. For a detailed derivation

Table 4.1 – Geometry and parameters for the DNS runs.

Label	$L_x \times L_y \times L_z$	$N_x \times N_y \times N_z$	Re_m	α	T
A	$1200 \times 200 \times 100$	$1024 \times 256 \times 768$	967	90°	6132
B	$1200 \times 200 \times 100$	$1024 \times 256 \times 768$	967	80°	6132
C	$1600 \times 400 \times 200$	$1024 \times 256 \times 768$	967	70°	6132
D	$3200 \times 400 \times 200$	$2048 \times 256 \times 768$	967	60°	6132

of Eqs. 4.1, 4.2 and 4.3 we refer the interested reader to Fedorovich and Shapiro (2009b). Integration of Eqs. 4.1, 4.2 and 4.3 is performed over a regular bounded spatial domain $[0,\hat{L}_x] \times [0,\hat{L}_y] \times [0,\hat{L}_z]$, with periodic boundary conditions in the along-slope and across-slope directions $(\hat{x},\hat{y})$ and where $\hat{u}(\hat{L}_z) = \hat{b}(\hat{L}_z) = 0$, $\hat{u}(0) = 0$, and $\hat{b}(0) = \hat{b}_s$.

Results are presented in normalized units, i.e. $u_i \equiv \hat{u}_i \hat{U}^{-1}$, $b \equiv \hat{b}\hat{B}^{-1}$, $x_i \equiv \hat{x}_i \hat{L}^{-1}$ where the characteristic velocity $\hat{U}$, buoyancy $\hat{B}$ and length $\hat{L}$ scales are defined as

$$\hat{L} = \sqrt{\frac{\hat{\nu}}{\hat{N}\sin\alpha}}, \quad \hat{B} = |\hat{b}_s|, \quad \hat{U} = \frac{|\hat{b}_s|}{\hat{N}}. \tag{4.4}$$

Based on the Π theorem (Buckingham, 1914) it is possible to show that the dimensionless solution is a universal function of the three dimensionless parameters $Re_m = |\hat{b}_s|(\hat{N}^{3/2}\hat{\nu}\sin\alpha)^{-1}$, α, and Pr, where Re_m is a modified Reynolds number, which depends on α. Relations 4.4 were found to significantly reduce the sensitivity of averaged mean profiles with respect to the model dimensionless parameters, thus providing a solid ground for analysis. Further, the current definition of Re_m allows to maintain a constant prefactor to the viscous term in the non-dimensional settings, therefore allowing for an equivalent scale separation (in terms of turbulence) across the considered sloping angles. We solve the dimensionless version of Eqs. 4.1, 4.2 and 4.3, where the non-linear terms are represented in their rotational form, to ensure conservation of mass and kinetic energy. The DNS algorithm is a modification of the code originally developed in (Albertson and Parlange, 1999b) to study land atmosphere interaction processes. A pseudo-spectral collocation approach based on truncated Fourier expansions is used in the x, y coordinate directions whereas a second-order accurate centered finite differences scheme is adopted in the vertical direction, requiring a staggered grid approach for the u, v, p, b variables. Time integration is performed adopting a fully explicit second-order accurate Adams-Bashforth scheme and a fractional step method is adopted to compute the pressure field by solving an additional Poisson equation. All nonlinear terms are de-aliased adopting the 3/2 rule (Canuto et al., 2006). Normalized boundary condition are $u(0) = u(L_z) = b(L_z) = 0$ and $b(0) = -1$ (downslope flow). We fix $Pr = 1$ and the modified Reynolds number $Re_m = 967$ throughout the runs. The domain size is chosen in order to allow a full representation of coherent structures populating the boundary layer. The current resolution satisfies the resolvability condition in the normal-to-slope direction $\Delta_z < 2\eta$, where $\eta = Re_m^{-3/4}\epsilon^{-1/4}$ (Kolmogorov length scale in normalized units). In the horizontal directions

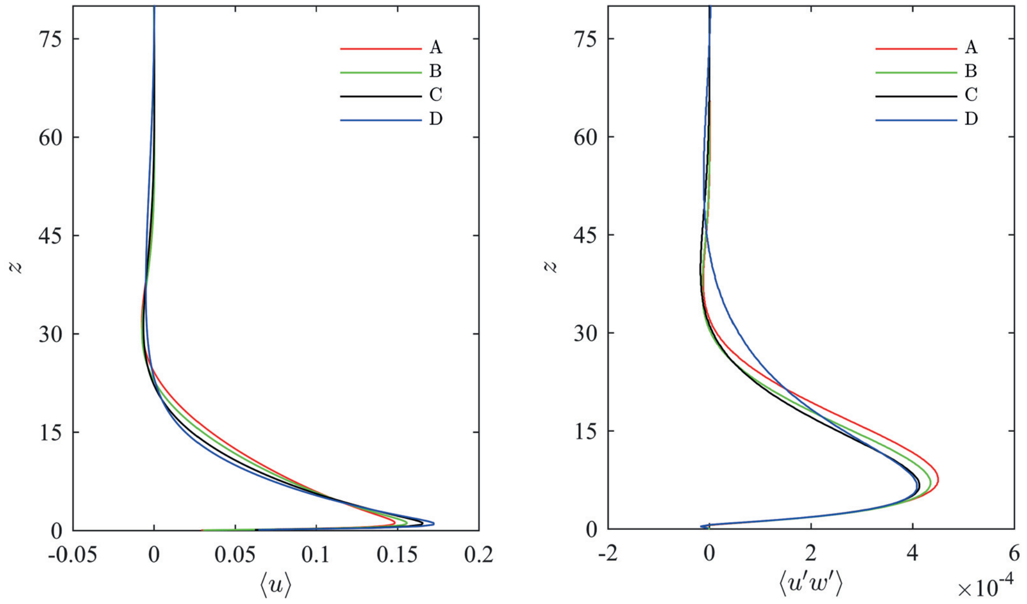

Figure 4.1 – Time and space averaged along-slope normalized velocity $\langle u \rangle$ (left) and Reynolds stress $\langle u'w' \rangle$ (right).

the grid stencil allows to resolve the turbulent scales at which the dissipation peak occurs, but does not satisfy the resolvability condition, especially in the near surface regions. The solution is therefore under-resolved. To determine the quality of the computed results an additional simulation was performed for the $\alpha = 90°$ case, using a twice as fine resolution in the horizontal directions. Results showed negligible differences in mean profiles and second order statistics, thus certifying the quality of computations at the considered resolution. Four sloping angles (α) are considered, as reported in table 5.1. For each case, a warm-up simulation is first performed until dynamic equilibrium is reached (statistical steady-state). Simulations are then further integrated over a minimum of $10T$ for the statistical analyses, where $T = 2\pi Re_m$ is the characteristic period of internal gravity waves that arise in the system, due to the (imposed) stable background stratification.

Throughout the study $\langle\cdot\rangle$ denotes averaging in time and along spatial coordinates of statistical homogeneity (x, y), whereas $(\cdot)'$ will denote a time fluctuation for a given variable.

4.3 Results and discussion

4.3.1 Mean flow and velocity fluctuations

Mean profiles of normalized along-slope velocity $\langle u \rangle$ and normalized Reynolds stress $\langle u'w' \rangle$ are displayed in Fig. 4.1 for the four considered sloping angles (α). $\langle u \rangle$ profiles are characterized by steep gradients in the near wall region, where a *zero-gradient layer* forms, the so-called LLJ. Under the current settings the LLJ can be loosely regarded as a separation layer between the inner (mostly laminar) and outer (turbulent) regions of the flow, characterized by a distinct interplay between dynamics and thermodynamics. Note also the sign change of the average Reynolds flux, which occurs roughly at the height of the LLJ (z_j). $\langle u'w'\rangle$ peaks in the relatively thick shear layer (characterized by a negative shear rate) located in the above-jet regions. As previously mentioned, the proposed set of normalization constants $\hat{U}, \hat{L}$ and $\hat{B}$ allows to remarkably collapse the location of the LLJ ($z_j \approx 1.1$), and to reduce the sensitivity of the outer solution with respect to variations in α, when compared against variations of a corresponding dimensional solution. The peak velocity (u_j) and the height of the dynamic boundary layer δ, which we identify as the location of the second zero-crossing of $\langle u\rangle$ (above the return flow region), vary by less than 15% and 25% respectively across the considered cases.

Figure 4.2 shows the fluctuations of the normalized streamwise velocity in the horizontal plane at $z = 8.2$ for the four cases with different slope angles. The filled 2-D contour plots are representative of the crest of the last internal wave oscillation that was simulated. There is evidence of alternating high and low-speed streaks, elongated in the streamwise direction, and meandering downstream, features that closely resemble those previously observed in the logarithmic region of classic turbulent boundary layers (Kim and Adrian, 1999; Hutchins and Marusic, 2007a; Lee and Sung, 2011). An importation observation here is that the lengths of these streaks increase with decreasing slope angle, and that regions of high-momentum fluid become apparently more sparse in space. For the case of $\alpha = 70^\circ$, the streaks are clearly more elongated than those characterizing the $\alpha = 80^\circ$ and $\alpha = 90^\circ$ runs. For the $\alpha = 60^\circ$ run, the lengths of the streaks is over 5δ, and the patterns resemble those of VLSMs observed in both experimental and DNS studies of classic turbulent boundary layers (Hutchins and Marusic, 2007a; Lee and Sung, 2011), as well as field measurements of ABL flows (Hutchins et al., 2012).

4.3.2 Pre-multiplied power spectra, co-spectra and quadrant analysis

In support of these observations, Fig. 4.3 presents pre-multiplied power spectra of the streamwise velocity u, evaluated in the along-slope direction at various distances from the wall. Premultiplying the spectrum by the wave number is a common technique that provides a more intuitive picture of the energy distribution across wavelengths in logarithmic plots, since equal areas under the curve correspond to equal energies. All the proposed spectra are characterized by a low wavenumber mode located at $\lambda_x \approx \delta$, which indicates the presence of LSMs within the dynamic boundary layer, affecting both the inner and outer regions of the flow. These results are in agreement with findings from canonical boundary-layer flows, where the average turbulent bulge is in the order of the boundary layer thickness (Robinson, 1991), and extends from the buffer to the overlap logarithmic layer. Interestingly, the length of LSMs in the outer layer seems to be independent of the sloping angle α. For the $\alpha = 70^\circ$ and $\alpha = 60^\circ$ cases, a second (larger wavelength) mode is apparent in the pre-multiplied power spectra, signature of VLSMs. The ratio between the two wavelengths is $\mathcal{O}(10)$, which is consistent with the

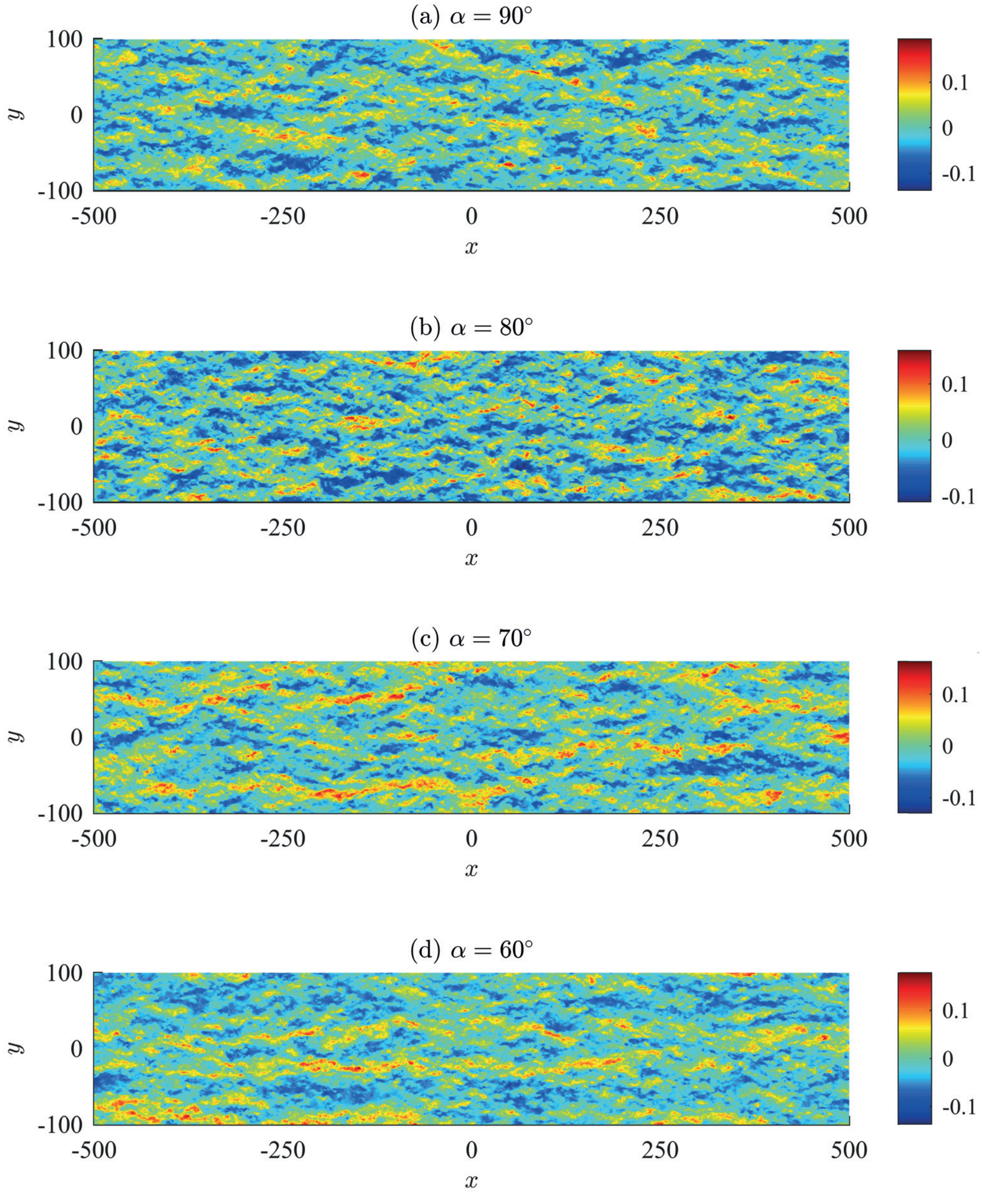

Figure 4.2 – Fluctuations of the normalized streamwise velocity in the horizontal plane at $z = 8.2$. The flow is from left to right. A smaller portion of the computational domain is shown for each case.

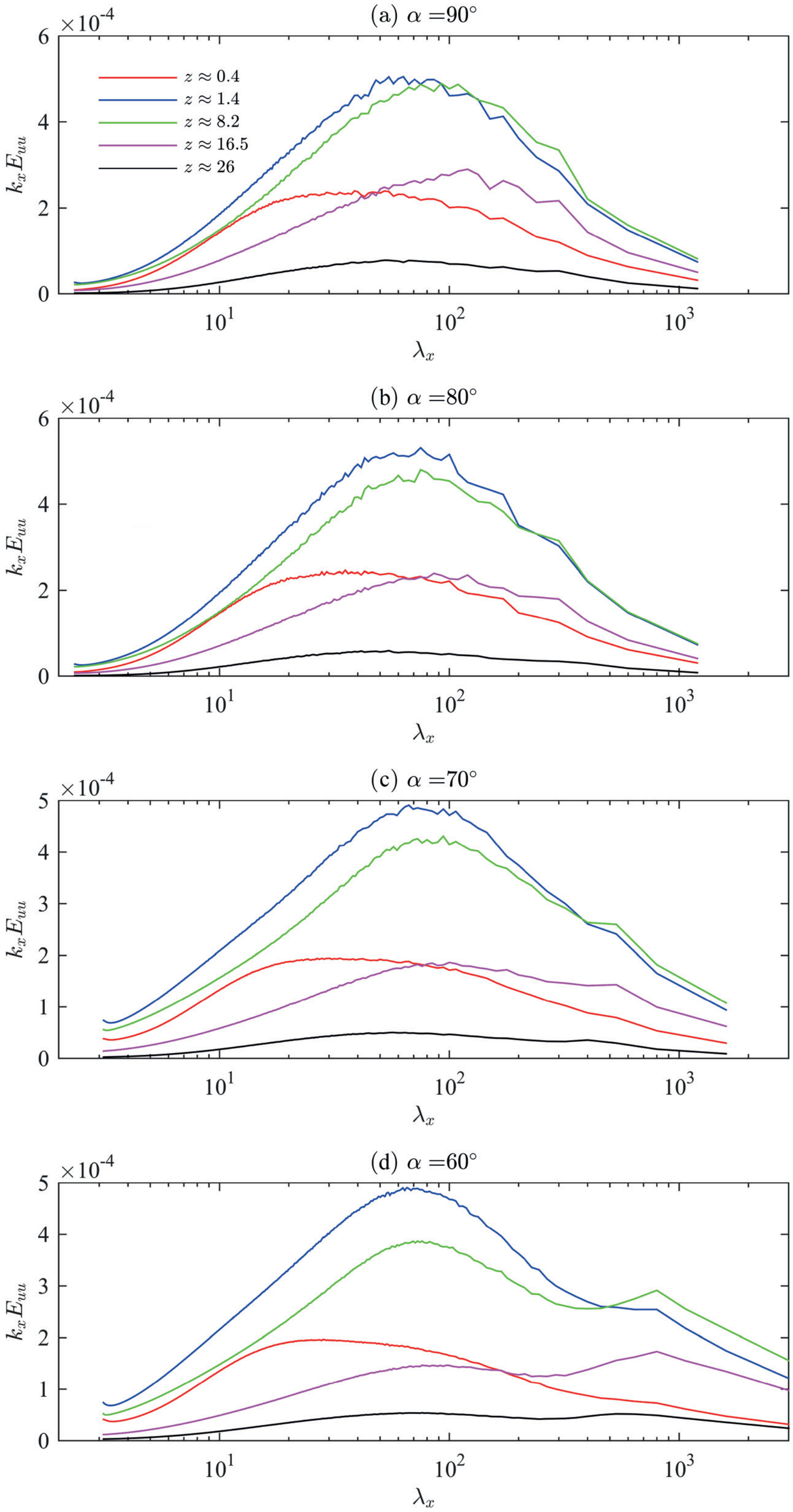

Figure 4.3 – Pre-multiplied power spectra as functions of streamwise wavelength for the streamwise velocity u.

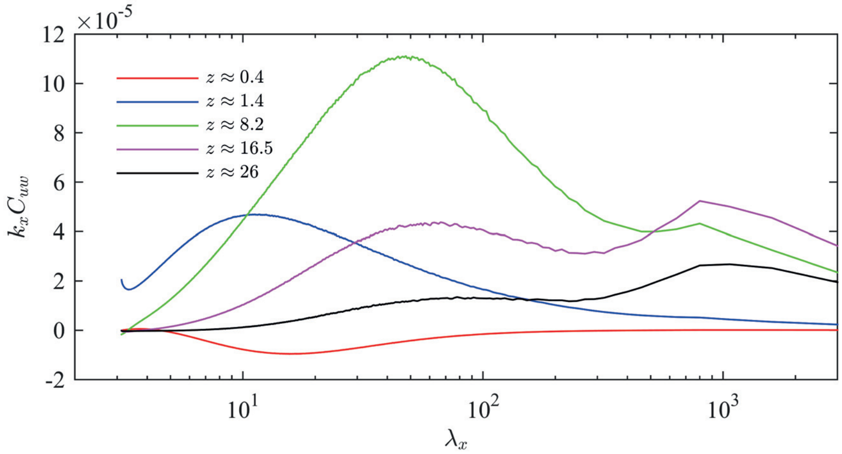

Figure 4.4 – Pre-multiplied co-spectra of the streamwise and normal-to-slope velocity components as functions of streamwise wavelength for the case D ($\alpha = 60°$).

definition of VLSMs by Kim and Adrian (1999). Note that as α decreases, the scale separation between LSMs and VLSMs increases, together with the relative importance of VLSMs in the overall contribution to the streamwise turbulent kinetic energy (TKE) component. Note also that for the $\alpha = 60°$ case, the large wavelength peaks become prominent in the pre-multiplied power spectrum, in particular at larger distances from the wall.

In addition, it is apparent how VLSMs have a modest footprint in the inner regions of the flow for case D ($\alpha = 60°$). The structural information arising from the pre-multiplied power spectra thus support from a statistical perspective observations based on the instantaneous flow patterns that were presented in Fig. 4.2: the flow organizes itself in stream-wise elongated patterns as the sloping angle departs from the vertical wall case ($\alpha = 90°$). It is worth mentioning that, under the current settings, the pre-multiplied power spectra for $\alpha = 30°$ (not shown) do not capture the higher mode of the distribution, and are characterized by an increasing energy as a function of the wavelength λ_x. On one hand, this confirms the finding that decreasing the slope angle leads to an increased size and importance of VLSMs, on the other hand, it suggests that a sound study of coherent structures in katabatic flows over shallow slopes would require a much larger domain size.

Pre-multiplied co-spectra of u and w for the case D are displayed in Fig. 4.4 as functions of the streamwise wavelength λ_x. The pre-multiplied co-spectra share strong similarities with their corresponding pre-multiplied power spectra, and further highlight the existence of LSMs and VLSMs in the dynamic boundary layer. Note in particular the significant contribution of VLSMs to the overall turbulent momentum flux with increasing distance from the wall, highlighting their active role (in the Townsend (1956) sense) in the boundary layer. VLSMs carry a significant portion of both the streamwise component of TKE and of the total turbulent momentum flux. Integrating the computed spectra and co-spectra over $\lambda_x > 5\delta$ (corresponding to the range of scales characterising VLSMs) we found that the contribution to the streamwise TKE and

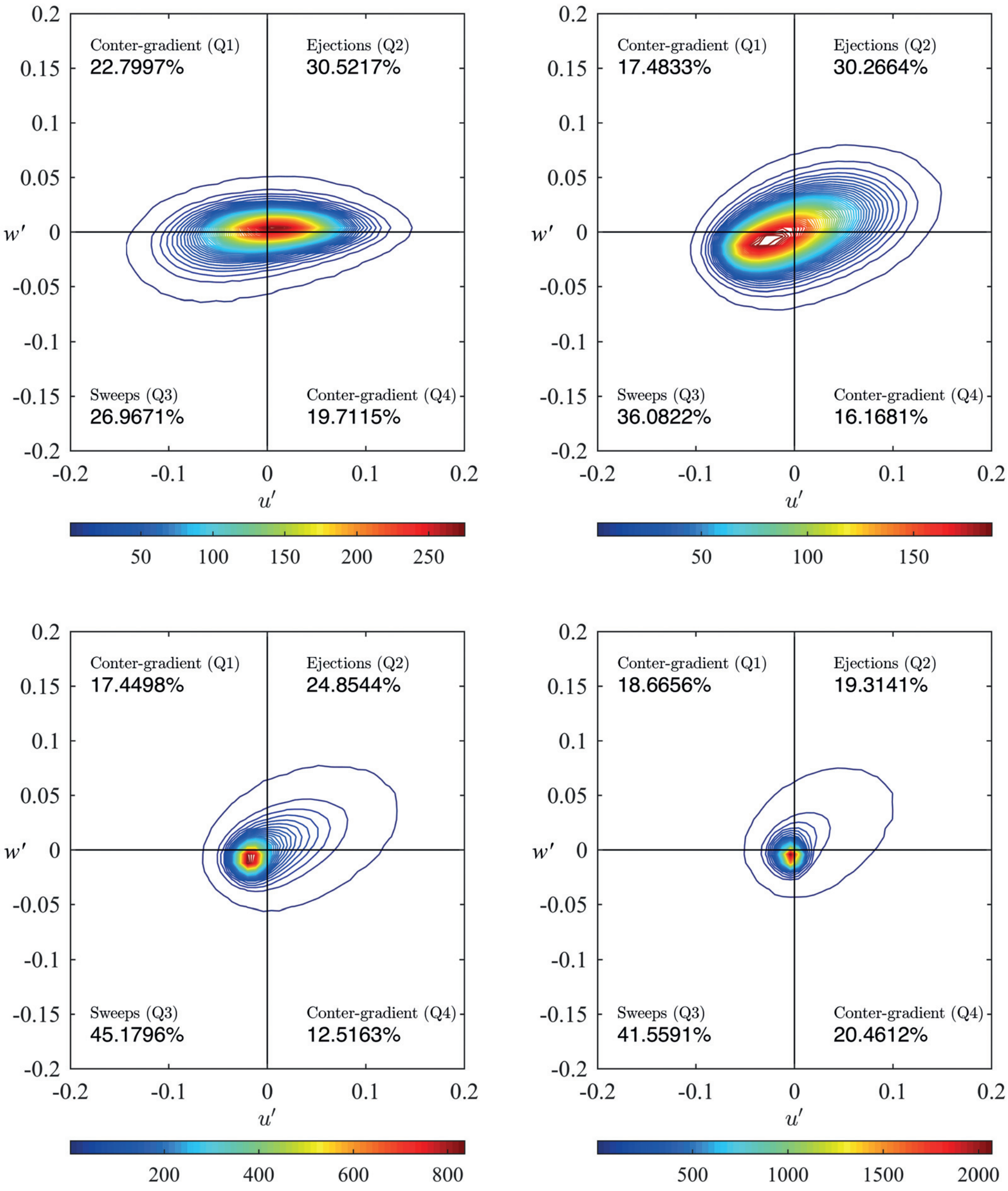

Figure 4.5 – Quadrants for the $u'w'$ momentum flux for the case D ($\alpha = 60°$). From top left to bottom right plots correspond to an increasing distance from the wall ($z = 1.4, 8.2, 16.5$ and 26 respectively).

turbulent momentum flux of VLSMs increases with height and reaches a maximum of 30% and 45% respectively at $z = 16$. The contribution of LSMs and VLSMs to the overall Reynolds flux in the inner regions of the flow is small, as apparent from Fig. 4.4, suggesting large-scale eddies primarily produce wall-parallel motions at the wall (due to its blocking effects), which is consistent with Townsend's idea of inactive motions (Townsend, 1956).

To gain further insights, in Fig. 4.5 we propose a quadrant decomposition of the turbulent momentum flux $u'w'$. Statistics are representative of values at horizontal $x - y$ planes and are computed over several internal-wave oscillations. The quadrant analysis highlights the importance of Q1 events ($u' > 0, w' > 0$) in the near LLJ regions, whereas Q3 events become dominant at further distance from the wall. Note that, given the negative shear rate characterizing the above-jet regions in katabatic flows, Q1 and Q3 events are positive contributions to the turbulent momentum flux, whereas Q2 and Q4 events are a negative contribution. The skewness of $u'w'$, apparent in the quadrants $(b), (c)$ and (d) of Fig. 4.5, highlights the relative strength of ejections (Q1), when compared against sweeps (Q3), despite their relatively minor contribution to the total vertical momentum flux. This is in agreement with the instantaneous stream-wise velocity contour presented Fig. 4.2, where broad (in the spanwise direction) regions of relatively uniform low momentum fluid are surrounded by relatively narrow, stream-wise elongated high speed streaks. The relatively sparse high-speed regions of case D, when compared against the more homogeneous velocity patterns, characterizing cases A and B for instance (see Fig. 4.2), and the dominance of relatively modest Q3 events in the outer regions of the boundary layer might be justified if one considers that as the sloping angle (α) decreases, the flow is characterized by stronger static stability, induced by both the imposed (negative) surface buoyancy, and the background stratification. Buoyancy has a direct effect in damping vertical fluctuations of momentum w', thus suppressing ejections events (Q1), and enhancing sweep events (Q3), which is consistent with presented results. Based on this, one might already speculate that LSMs and VLSMs are bulges of alternating relatively high- low-momentum fluid. High-momentum fluid is ejected from the LLJ regions toward the outer layer, and flanked by broader (in the spanwise direction) regions of low momentum fluid, which become dominant in the upper parts of the outer layer due to direct buoyant suppression of w'. Additional details on the structure and origin of LSMs and VLSMs in katabatic flows will be provided in the following sections.

4.3.3 Two point correlation coefficients

To further characterize the flow's structure, in Fig. 4.6 we display the two-point time and space averaged streamwise correlation coefficients of the instantaneous u velocity ($R_{uu}(\Delta x, 0, z)$), for the case D. Profiles clearly indicate a streamwise and spanwise growth of motions up to $z \approx 16$, in the neighborhood of the first zero-crossing of the $\langle u \rangle$ velocity. The integrated R_{uu} confirms the presence of structures characterized by an Eulerian length scale $\mathscr{L}_{11} \approx \delta$, in agreement with the definition of LSMs. Negative lobes in the correlation function in the spanwise direction are indicative of regions of relatively higher/lower momentum flanking each others, in agreement

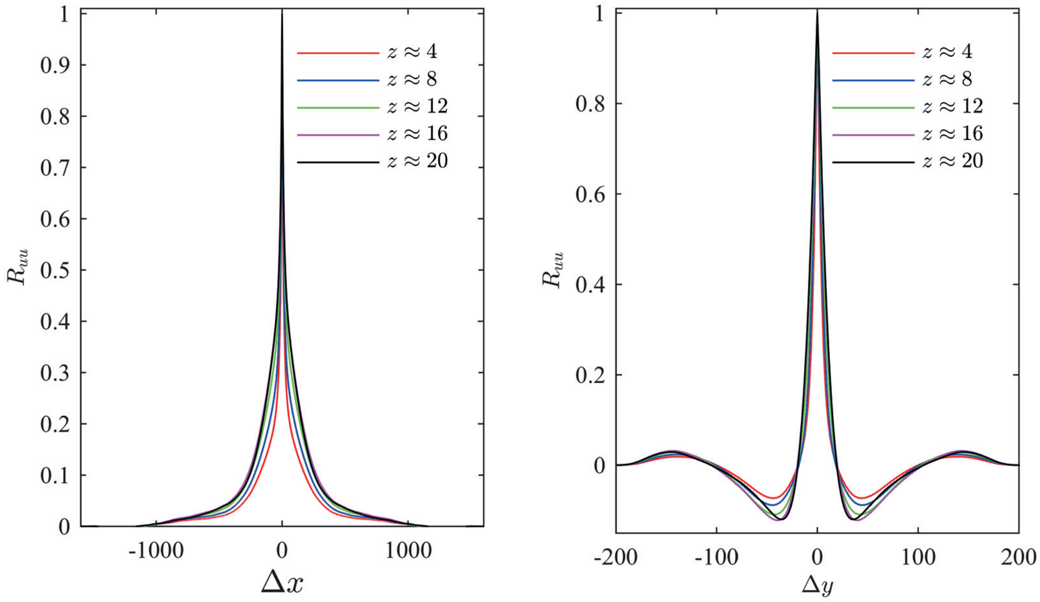

Figure 4.6 – Streamwise (left) and spanwise (right) two-point correlation coefficients of the streamwise velocity ($R_{uu}(\Delta x, 0, z)$ and $R_{uu}(0, \Delta y, z)$) calculated at different distances from the wall for the case D.

to what observed in Fig. 4.2 and in agreement with results from canonical wall-bounded flows (Marusic and Hutchins, 2008). A better picture and a quantification of the vertical coherency of the flow result from the three dimensional spatial correlation function of the streamwise velocity, defined as

$$R_{uu}^{3d}(\Delta x, \Delta y, z, z_r) = \frac{\langle u'(x, y, z_r)\, u'(x+\Delta x, y+\Delta y, z)\rangle}{\langle u'^2(x, y, z_r)\rangle}. \tag{4.5}$$

Isosurfaces of R_{uu}^{3d} are displayed in Figure 4.7, for $z_r = 16$. The region of positive correlation (marked by red) is highly elongated in the streamwise direction and, as expected, is flanked on either side in the spanwise direction by a region of negative correlation (marked by blue). The positive correlation iso-surface extends vertically over the entire layer characterized by a negative shear rate (up to $z \approx 32$). Moreover, the iso-surfaces are inclined upward along the upstream direction and more elongated towards the downstream direction, in net contrast with results from canonical boundary layer flows, where iso-surfaces are usually inclined upward in the downstream direction and are characterized by an elongated tail in the upstream regions. This, as explained in the following, is a direct consequence of the geometrical structure of coherent motions in katabatic flows.

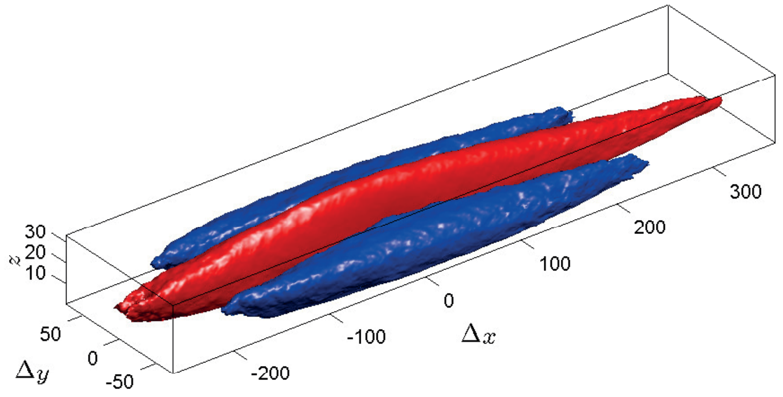
30
20
10
z
50
0
-50
Δy
-200
-100
0
100
200
300
Δx

Figure 4.7 – Iso-surfaces of R_{uu}^{3d} with $z_r = 16$. Red iso-surfaces show positive correlation ($R_{uu}^{3d} = 0.1$), whereas blue iso-surfaces show negative correlation ($R_{uu}^{3d} = -0.1$).

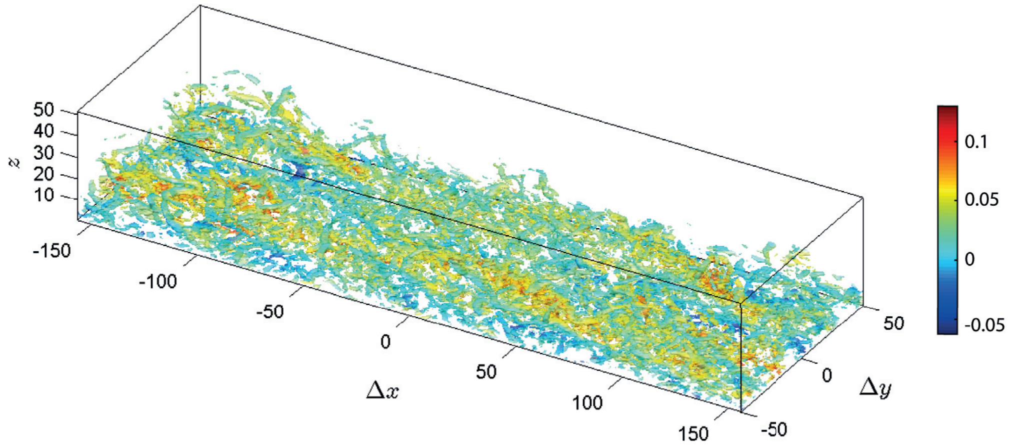
50
40
30
20
10
z
-150
-100
-50
0
50
100
150
Δx
50
0
-50
Δy
0.1
0.05
0
-0.05

Figure 4.8 – Visualization of the vortex distribution detected by the Q-criterion. The $Q = 0.05Q_{max}$ iso-surfaces are colored by u'.

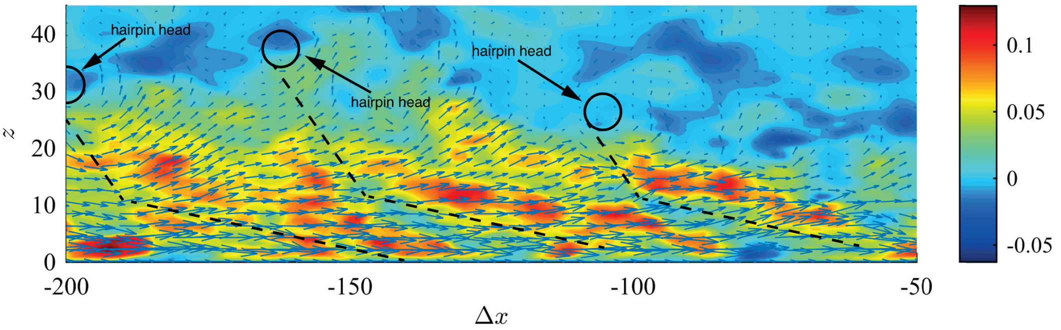

Figure 4.9 – Vector plot of the instantaneous velocity field over a $x-z$ plane intersecting a high-momentum region, colored by the instantaneous velocity fluctuation with respect to the instantaneous planar average value $u'' = u - \langle u \rangle$.

4.3.4 Characterization of LSMs and VLSMs

To gain further insights on the structure of LSMs and VLSMs iso-surfaces of the second invariant of the full-velocity tensor (Jeong and Hussain, 1995)

$$Q = -\frac{1}{2}\frac{\partial u_j}{\partial x_i}\frac{\partial u_i}{\partial x_j} \tag{4.6}$$

are displayed in Fig. 4.8. The considered subset of the domain is centered in correspondence of a high-momentum event. From Fig. 4.8 is clear how the boundary layer is populated by LSMs of high momentum, flanked by similarly elongated regions of low momentum, and coherent over a length scale proportional to the boundary layer thickness δ. The overall picture is consistent with the observed peaks in the pre-multiplied spectra and co-spectra (see Fig. 4.3 and 4.4), and with the trend of the two-point correlation coefficients (see Fig. 4.6). Fig. 4.8 suggests that, similarly to what is observed in canonical boundary layer flows, packets of hairpins concatenate in the streamwise direction to form LSMs in the outer layer. It is also apparent in Fig. 4.8 how LSMs further align to form larger structures, likely resulting in the VLSMs signatures presented in Fig 4.3 and 4.4.

A velocity-vector map, displayed in Fig. 4.9, further confirms the presence of hairpins around the high-momentum bulge. The observed katabatic flow hairpin vortices (KFHV in the following) are characterized by a head located upstream in the return flow region, and by legs inclined at about 12°, protruding downstream into the inner regions of the flow. The tails are connected to the head by vortex necks inclined at roughly 45° to the wall. Note that the specific inclination angles of the vortex neck and tail might depend on the sloping angle of the underlying surface. The streamwise separation of KFHV structures is about $\delta/2$. KFHV are pumping high velocity fluid from the LLJ regions up in the outer layer, resulting in the

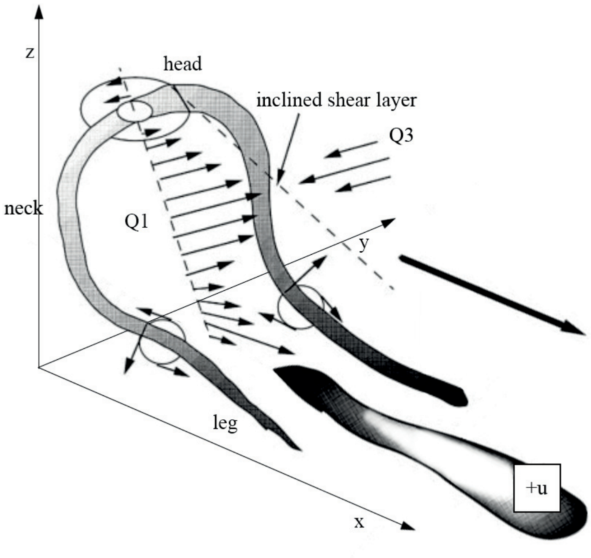

Figure 4.10 – Schematic of a katabatic flow hairpin vortex and the induced motion. Adapted from Adrian et al. (2000).

documented Q1 events (see Fig. 4.5). Adrian et al. (2000) described an idealized hairpin vortex signature for canonical boundary layers as having three characteristics in a $x-z$ plane: (1) a vortex head, (2) an ejection of low-momentum fluid event, created by the induction of the vortex legs, and (3) a stagnation point where the ejected low-momentum fluid meets the faster upstream fluid. Based on the same reasoning, an idealized KFHV might be defined by three characteristics in the $x-z$ plane: (1) a vortex head, (2) an ejection of high-momentum fluid event, created by the induction of the vortex legs, and (3) a stagnation point, where the ejected fast-momentum fluid meets the slower upstream fluid, resulting often in a Q3 event and in the formation of an inclined shear layer upstream. Q1-Q3 events can thus be regarded as the characteristic signature of a hairpin vortex in katabatic flows. As in classical boundary layer flows (Adrian et al., 2000; Tomkins and Adrian, 2003), these signatures in the $x-z$ planes appear frequently in groups in the streamwise direction, and thus the stagnation point might not be present, because the upstream vortex prevents the impingement of the low-speed fluid onto the high-speed fluid. This is the case in the velocity-vector map displayed in Fig. 4.9 for instance. Figure 4.10 schematically depicts the structure of a typical KFHV and the induced flow events on a $x-z$ plane that cuts through the centre of the vortex. The schematic has been adapted from Adrian et al. (2000), to highlight the apparent symmetries between katabatic flows and canonical pressure-driven boundary layers.

Velocity-vector maps consistently report hairpins heads located in the return flow region (as in Fig. 4.9). This might be justified from a purely dynamical point of view, considering the Magnus effect resulting from the positive (anti-clockwise) rotation of the spanwise vortex: heads in the regions of negative shear would experience a negative force in the normal-to-

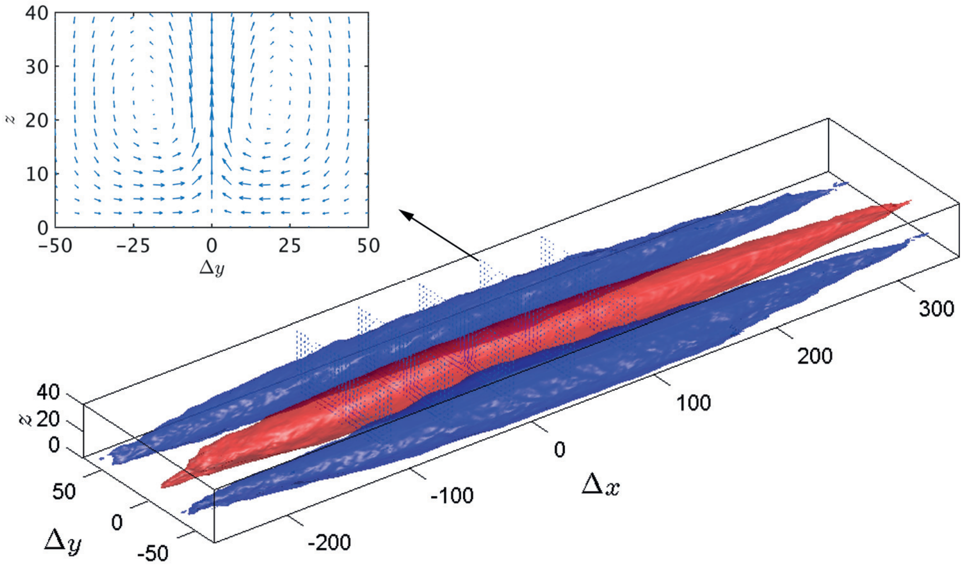

Figure 4.11 – Conditionally-averaged flow field, where the conditional event is a high-speed event (of positive u fluctuation) at $(x, y, z) = (0, 0, 16)$. An Iso-surface of positive u fluctuation ($u' = 0.0039$) is displayed in red, flanked by iso-surfaces of negative u fluctuation ($u' = -0.0031$). An inset providing a zoom on the velocity-vector map in the $y - z$ plane is also shown.

slope (z) direction, shifting them toward the wall, and likely resulting in a collapse of the structure, whereas heads in the return flow region, which is characterized by a negligible shear rate, are likely to hold their position over several eddy turnover times, and might likely be responsible for the growth of the boundary layer δ.

To further clarify (from a statistical perspective) the structure of LSMs and VLSMs Fig. 4.11 displays the conditionally-averaged flow field, where the sampling condition is a high-speed event at $(x, y, z) = (0, 0, 16)$. At such distance from the wall VLSM provide the largest contribution to $\langle u'w' \rangle$. High-momentum regions are represented by a red iso-surface of positive u fluctuation, whereas low-momentum regions are represented by a blue iso-surface of negative u fluctuation. The visualized structures are centered around the conditional point and reach up to $z \approx 32$. Large-scale roll modes are apparent from the proposed inset, where velocity vectors on the $y - z$ cross-plane are displayed. The conditionally-averaged flow field validates the schematic of Fig. 4.10, where a counter-rotating vortex pair (the legs of KFHVs) induce an upwash of high momentum fluid in the above-jet regions. Besides, from Fig. 4.11 is apparent how the counter-rotating vortex pair is directly responsible for the observed low-momentum regions (blue iso-surfaces), generated by Q3 events. In particular, note the radial asymmetry if the roll modes, whose axis is shifted toward the ejection event, resulting in narrow (in the spanwise direction), highly energetic ejection of high speed fluid, flanked on each side by broad sweeps of low momentum fluid.

This suggests a decomposition of the outer layer in katabatic flows in sparse, stream-wise elongated high momentum regions, Q1 events induced by the rotation of radially asymmetric hairpin legs, flanked by broad, low momentum fluid: Q3 events also induced by rotation of the hairpins' legs. The asymmetry of the hairpins' legs is likely a result of the background stable stratification, which confines strong ejections to relatively narrow regions in the flow. Iso-surfaces displayed in Fig. 4.11 further confirms the observed hairpin paradigm: a relatively narrow high momentum fluid is flanked by relatively broader low momentum regions, characterized by an overall stream-wise extension of about 5δ, induced by the clustering and streamwise alignment of hairpin vortices. Note the similarity with the large-scale roll modes previously observed in laboratory experiments of turbulent boundary layers (Marusic and Hutchins, 2008) and large-eddy simulations of atmospheric boundary layers (Fang and Porté-Agel, 2015). Further, from Fig. 4.11 it is also apparent how the high-momentum event is characterized by a negligible time-averaged w component near the wall, likely resulting in the observed inactive role of LSMs and VLSMs in such regions.

4.4 Summary and conclusions

Large and very-large scale motions populating katabatic flows over steep slopes are identified and characterized from DNS at a modified Reynolds number, $Re_m \sim 967$, considering four different slope angles. Based on flow visualization and statistical analysis it is apparent how the energetic coherent structures in katabatic flows are strongly dependent on the slope angle. Pre-multiplied power spectra and co-spectra confirm the presence of LSMs, characterized by a streamwise extension on the order of the boundary layer thickness (δ). A second mode characterizes pre-multiplied spectra and co-spectra when the slope angle is below 70 degrees, indicative of VLSMs. For the smaller among the considered surface sloping angles, VLSMs are found to carry a significant portion of the streamwise TKE component and shear stress in the above-jet regions of the flow, which can represent 30% to 45% of the total TKE over certain layers. Conversely, LSMs and VLSMs can be regarded as inactive motions in the near-wall regions. Results highlight how LSMs and VLSMs are formed when harping vortices concatenate in the streamwise direction, with typical separation of about $\delta/2$. Katabatic flow hairpin vortices (KFHV) are characterized by a head located upstream in the return flow region, and by tails inclined at about 12° protruding downstream into the inner regions of the flow. In addition, the tails are connected to the head by vortex necks inclined at roughly 45° to the wall. The rotation of the hairpins' legs induces high-momentum fluid from the LLJ regions in the outer layer (Q1 event), followed by a sweep of low-momentum fluid (Q3 event) and resulting in an inclined shear layer located upstream of the vortex. A sequence of Q1-Q3 events is hence proposed as characteristic signature of KFHVs. The proposed hairpin paradigm identifies LSMs and VLSMs as the observed alternation of narrow (in the spanwise direction) bulges of high-momentum fluid, and the relatively broader regions of low momentum fluid, both induced by the rotation of hairpin's legs. Results further suggest that a larger domain size is necessary in order to accommodate VLSMs in katabatic flows over shallow slopes.

Bibliography

R. J. Adrian, C. D. Meinhart, and C. D. Tomkins. Vortex organization in the outer region of the turbulent boundary layer. *J Fluid Mech*, 422:1–54, 2000.

Ronald J. Adrian. Hairpin vortex organization in wall turbulence. *Phys Fluids*, 19(4):041301, 2007.

J. D. Albertson and M. B. Parlange. Natural integration of scalar fluxes from complex terrain. *Adv Water Resour*, 23(3):239–252, 1999.

S. Axelsen and H. Dop. Large-eddy simulation of katabatic winds. Part 1: Comparison with observations. *Acta Geophys*, 57(4):803–836, 2009.

B. J. Balakumar and R. J. Adrian. Large- and very-large-scale motions in channel and boundary-layer flows. *Philosophical Transactions of the Royal Society A: Mathematical, Physical and Engineering Sciences*, 365:665–681, 2007.

E. Buckingham. On physically similar systems; Illustrations of the use of dimensional equations. *Phys Rev*, 4(4):345–376, 1914.

B. Burkholder, A. Shapiro, and E. Fedorovich. Katabatic flow induced by a cross-slope band of surface cooling. *Acta Geophys*, 57(4):923–949, 2009.

C. Canuto, M. Y. Hussaini, A. Quarteroni, and T. A. Zang. *Spectral methods*. Scientific Computation. Springer Berlin Heidelberg, Berlin, Heidelberg, 2006.

D. Chung and B. J. McKeon. Large-eddy simulation of large-scale structures in long channel flow. *J Fluid Mech*, 661:341–364, 2010.

J. C. Del Lamo, J. Jimenez, P. Zandonade, and R. D. Moser. Scaling of the energy spectra of turbulent channels. *J Fluid Mech*, 500:135–144, 2004.

J. Fang and F. Porté-Agel. Large-eddy simulation of very-large-scale motions in the neutrally stratified atmospheric boundary layer. *Boundary-Layer Meteorol*, 155(3):397–416, 2015.

E. Fedorovich and A. Shapiro. Turbulent natural convection along a vertical plate immersed in a stably stratified fluid. *J Fluid Mech*, 636:41–57, 2009a.

E. Fedorovich and A. Shapiro. Structure of numerically simulated katabatic and anabatic flows along steep slopes. *Acta Geophys*, 57(4):981–1010, 2009b.

H. J. S. Fernando. Fluid dynamics of urban atmospheres in complex terrain. *Annu Rev Fluid Mech*, 42(1):365–389, 2010.

B. Ganapatisubramani, E. K. Longmire, and I. Marusic. Characteristics of vortex packets in turbulent boundary layers. *J Fluid Mech*, 478:35–46, 2003.

A. A. Grachev, L. S. Leo, S. D. Sabatino, H. J. S. Fernando, E. R. Pardyjak, and C. W. Fairall. Structure of turbulence in katabatic flows below and above the wind-speed maximum. *Boundary-Layer Meteorol*, 2015.

B. Grisogono and J. Oerlemans. Katabatic flow: Analytic solution for gradually varying eddy diffusivities. *J Atmos Sci*, 58(21):3349–3354, 2001.

B. Grisogono, T. Jurlina, Ž. Večenaj, and I. Güttler. Weakly nonlinear Prandtl model for simple slope flows. *Q J R Meteorol Soc*, 141(688):883–892, 2015.

M. Guala, S. E. Hommema, and R. J. Adrian. Large-scale and very-large-scale motions in turbulent pipe flow. *J Fluid Mech*, 554:521–542, 2006.

L. N. Gutman. On the theory of the katabatic slope wind. *Tellus*, 35A:213–218, 1983.

N. Hutchins and I. Marusic. Evidence of very long meandering features in the logarithmic region of turbulent boundary layers. *J Fluid Mech*, 579:1–28, 2007a.

N. Hutchins and I. Marusic. Large-scale influences in near-wall turbulence. *Philosophical Transactions of the Royal Society A: Mathematical, Physical and Engineering Sciences*, 365: 647–664, 2007b.

N. Hutchins, K. Chauhan, I. Marusic, J. Monty, and J. Klewicki. Towards reconciling the large-scale structure of turbulent boundary layers in the atmosphere and laboratory. *Boundary-Layer Meteorol*, 145(2):273–306, 2012.

J. Jeong and F. Hussain. On the identification of a vortex. *J Fluid Mech*, 285:69–94, 1995.

K. C. Kim and R. J. Adrian. Very large-scale motion in the outer layer. *Phys Fluids*, 11(2): 417–422, 1999.

L. S. G. Kovasznay, V. Kibens, and R. F. Blackwelder. Large-scale motion in the intermittent region of a turbulent boundary layer. *J Fluid Mech*, 41(2):283–325, 1970.

J. Hwa Lee and Hyung Jin Sung. Very-large-scale motions in a turbulent boundary layer. *J Fluid Mech*, 673:80–120, 2011.

I. Marusic and N. Hutchins. Study of the log-layer structure in wall turbulence over a very large range of reynolds number. *Flow, Turbul Combust*, 81(1):115–130, 2008.

I. Marusic, B. J. McKeon, P. A. Monkewitz, H. M. Nagib, A. J. Smits, and K. R. Sreenivasan. Wall-bounded turbulent flows at high Reynolds numbers: Recent advances and key issues. *Phys Fluids*, 22(6):065103, 2010.

R. Mathis, N. Hutchins, and I. Marusic. Large-scale amplitude modulation of the small-scale structures in turbulent boundary layers. *J Fluid Mech*, 628:311–337, 2009.

P. Monti, H. J. S. Fernando, and M. Princevac. Waves and turbulence in katabatic winds. *Environ Fluid Mech*, 14(2):431–450, 2014.

D. F. Nadeau, E. R. Pardyjak, C. W. Higgins, and M. B. Parlange. Similarity scaling over a steep alpine slope. *Boundary-Layer Meteorol*, 147(3):401–419, 2013.

J. Oerlemans. The atmospheric boundary layer over melting glaciers. In *Clear and Cloudy Boundary Layers*, pages 129–153. Royal Netherlands Academy of Arts and Sciences, 1998.

J. Oerlemans and H. F. Vugts. A meteorological experiment in the melting zone of the Greenland ice sheet. *Bull Am Meteorol Soc*, 74(3):355–365, 1993.

H. J. Oldroyd, G. G. Katul, E. R. Pardyjak, and M. B. Parlange. Momentum balance of katabatic flow on steep slopes covered with short vegetation. *Geophys Res Lett*, 41(13):4761–4768, 2014.

H. J. Oldroyd, E. R. Pardyjak, H. Huwald, and M.B. Parlange. Adapting tilt corrections and the governing flow equations for steep, fully three-dimensional, mountainous terrain. *Boundary-Layer Meteorol*, pages 1–27, 2015.

T. R. Parish and D. H. Bromwich. A case study of Antarctic katabatic wind interaction with large-scale forcing. *Mon Weather Rev*, 126(1):199–209, 1998.

L. Prandtl. *Führer durch die strömungslehre*. Vieweg & Sohn, Braunschweig, 1942.

A. Renfrew, I. and S. Anderson, P. Profiles of katabatic flow in summer and winter over Coats Land, Antarctica. *Q J R Meteorol Soc*, 132(616):779–802, 2006.

S. Robinson. Coherent motions in the turbulent boundary layer. *Annu Rev Fluid Mech*, 23(1): 601–639, 1991.

U. Schumann. Large-eddy simulation of the up-slope boundary layer. *Q J R Meteorol Soc*, 116 (493):637–670, 1990.

S. Shah and E. Bou-Zeid. Very-large-scale motions in the atmospheric boundary layer educed by snapshot proper orthogonal decomposition. *Boundary-Layer Meteorol*, pages 1–33, 2014.

A. Shapiro and E. Fedorovich. Unsteady convectively driven flow along a vertical plate immersed in a stably stratified fluid. *J Fluid Mech*, 498:333–352, 2004a.

A. Shapiro and E. Fedorovich. Prandtl number dependence of unsteady natural convection along a vertical plate in a stably stratified fluid. *Int J Heat Mass Transf*, 47(22):4911–4927, 2004b.

A. Shapiro and E. Fedorovich. Katabatic flow along a differentially cooled sloping surface. *J Fluid Mech*, 571:149–175, 2007.

A. Shapiro and E. Fedorovich. A boundary-layer scaling for turbulent katabatic flow. *Boundary-Layer Meteorol*, 153(1):1–17, 2014.

P. F. Sheridan, S. B. Vosper, and A. R. Brown. Characteristics of cold pools observed in narrow valleys and dependence on external conditions. *Q J R Meteorol Soc*, 140(679):715–728, 2014.

E. D. Skyllingstad. Large-eddy simulation of katabatic flows. *Boundary-Layer Meteorol*, 106(2): 217–243, 2003.

C. D. Tomkins and R. J. Adrian. Spanwise structure and scale growth in turbulent boundary layers. *J Fluid Mech*, 490:37–74, 2003.

A. A. Townsend. *The structure of turbulent shear flow*. 1956.

C. D. Whiteman. Observations of thermally developed wind systems in mountainous terrain. *Atmos Process over complex terrain, Meteor Monogr*, 45:5–42, 1990.

C. D. Whiteman. Mountain meteorology: Fundamentals and applications. *Mountain Research and Development*, 21(1):355, 2000.

D. Zardi and C. D. Whiteman. Diurnal mountain wind systems. In *Mt Weather Res Forecast*, pages 35–119. Springer, 2013.

J. Zhou, R. J. Adrian, S. Balachandal, and T. M. Kendall. Mechanisms for generating coherent packets of hairpin vortices in channel flow. *J Fluid Mech*, 387:353–396, 1999.

5 Large-eddy simulation of atmospheric boundary-layer flow over Antarctic sea-ice formations using a dynamic roughness model

5.1 Abstract

A series of large-eddy simulations (LES) of fully developed flow over high-resolution snow-ice surfaces of Antarctic sea ice floes are performed to study surface drag and roughness parameters at process scales from 1 cm to 100 m. Snow/ice surface morphology was obtained using a terrestrial laser scanner during the SIPEX II (sea ice physics and ecosystem experiment II) research voyage to East Antarctica (September-November 2012). The effects of large-scale features of the surface on the wind flow (those features that can be resolved in LES) are accounted for through an immersed boundary method (IBM). Conversely, the drag forces caused by subgrid-scale features of the surface should be accounted for through a parameterization. However the effective hydrodynamic surface roughness parameter (z_0) for snow ice is not known. Hence, a recently developed dynamic surface roughness (DSR) model is adopted, in which z_0 is determined using the first-principles based constraint that the total momentum flux (drag) must be independent on the grid-filter scale. The model is found to be robust and yields accurate flow predictions (resolution invariant). An estimate of the dimensionless roughness parameter α is provided for use in climate, weather prediction, and scalar transport models to prescribe the hydrodynamic roughness length z_0

5.2 Introduction

Recent rapid changes in the climatology of sea ice extent in the Arctic as well as in the Antarctic are only partially understood (Kimura et al., 2013; Holland et al., 2014) and the decrease in Arctic sea ice contrasts the marked increase in the Antarctic counterpart (Simmonds, 2015). At the same time, sea ice dynamics has such a large influence on the climate system as a whole (e.g. Papritz et al. (2015)) that any climate or weather predictions remain uncertain if sea ice is not properly represented. One difficulty with accurate model predictions of sea ice dynamics is the very complex and dynamic interaction between the ice/snow surface and the atmosphere. Complex processes such as formation of snow ice (Eicken et al., 1994) or superimposed ice (Nicolaus et al., 2003; Obleitner, 2004), limitation of thermodynamic ice growth (Eicken et al., 1995), the formation of pressure ridges as well as drifting and blowing snow (Leonard and Maksym, 2011) all contribute to this complexity. Snow surfaces are therefore among the most dynamic surfaces on earth and roughness can change within hours (Trujillo et al., 2016; Amory et al., 2015). A particular difficulty is the correct representation of wind-ice drift relationships (Stössel et al., 2011; Uotila et al., 2014), which are intrinsically highly non-linear. Since the roughness of the snow surface can change quickly and over very large areas, a correct representation of momentum transfer is not only required to estimate large-scale ice drift and total ice mass balance (Zhang, 2014) but also to correctly represent erosion and deposition of snow in these heavily wind-blown environments (e.g. Groot Zwaaftink et al. (2014)). Only if the snow and roughness dynamics of the snow-on-sea ice surface are sufficiently well represented, progress in a quantitative assessment of the role of sea ice in the weather and climate system will be possible. This includes important aspects on biological life, which depends on light penetration through snow and ice (Nicolaus et al., 2012). While the importance of snow-atmosphere interactions has been recognized, the simplifications used in atmospheric models at the surface are still limiting, despite some recent progress in the area (Groot Zwaaftink et al., 2014).

Measurements and modeling of canonical boundary-layer flows over rough surfaces is at a somewhat more mature stage. The problem has in fact received great attention since the early works of Schlichting (1936) and Nikuradse (1950), summarized in the reviews by Raupach et al. (1991), Jimenez (2004) and Castro (2007). Much work has focused on flows characterized by a few length scales (Xie and Castro, 2006; Cheng et al., 2007; Kono et al., 2010; Anderson et al., 2015; Yang et al., 2016), which provide a convenient framework for the analysis, but more recently, a considerable amount of work has also focused on flow over objects and surfaces characterized by a broad range of scales, including fractal tree-like shapes immersed in a turbulent boundary layer (Chester and Meneveau, 2007; Chester et al., 2007), flows over urban-like obstacles (Cheng and Castro, 2002; Xie and Castro, 2009; Bou-Zeid et al., 2009), flows over gravel-beds (Nikora et al., 2001, 2004, 2007; Mignot et al., 2008, 2009; Yuan and Piomelli, 2014) and flows over fluvial-like landscapes (Anderson et al., 2012). Much of this knowledge can be used to study turbulent flow over sea-ice surfaces. In simulations of turbulent flow over rough, multi-scale surfaces, computational cost is the limiting factor. Considering sea ice landscapes for instance, on one hand, there is need to properly represent the flow interaction with the surface down to the smallest roughness elements, on the other hand, to be reasonably free from direct roughness effects one would need $H/\max(h) \gtrapprox 50$ (Jimenez, 2004), where H is the height of the computational domain, and h is the height of a generic roughness element. Regarding flow over sea ice surfaces as in fully rough regime one can set $hu_*\nu^{-1} = h^+ \gtrapprox 80$. Then, given the multi-scale nature of such surfaces, one can safely assume (as lower bound) $\max(h)/\min(h) = \mathcal{O}(>10^3)$, hence resulting in $H^+ \gtrapprox 4\times 10^6$. The largest direct numerical simulation (DNS) of wall-bounded flows at present is $H^+ = \mathcal{O}(10^3)$, hence the need for approaches that aim at reducing computational costs.

In this regard, LES represent a valid alternative to DNS, but its use introduces an additional roughness modeling requirement, as elaborated in the following. LES approaches rely on a (implicitly understood or explicit) spatial filtering operation in the bulk of the flow, and on a parameterization of the (removed) subgrid-scale (SGS) dynamics (see for instance Smagorinsky (1963); Germano et al. (1991)). In the case of landscapes characterized by a broad range of scales, the filtering operation also applies to the underlying surface, so one needs to model the effects of subgrid-scale roughness on the flow. Such a task is by no means trivial, given the lack of knowledge on turbulent flows in the interfacial layer (the layer below $\max(h)$), and given that drag contributions of small scales in fractal-like surfaces is usually a significant percentage of the total (Anderson and Meneveau, 2011; Anderson et al., 2012). In geophysical applications, when all roughness elements are unresolved, and viscous drag is negligible, it is common to rely on the equilibrium logarithmic law assumption (Prandtl, 1935; Monin and Obukhov, 1954) to estimate the drag that the surface is exerting on the flow

$$\frac{U(z)}{u_\star} = \frac{1}{\kappa} \ln\left(\frac{z-d}{z_0}\right), \tag{5.1}$$

where $u_\star = \sqrt{\tau_w \rho^{-1}}$ is the friction velocity, τ_w is the wall stress, ρ is a reference constant density, $U(z)$ is the mean streamwise velocity at a given distance z from the wall, $\kappa \approx 0.41$ is the von Kármán constant, z_0 and d are the hydrodynamic roughness length and the zero-plane displacement height respectively. z_0 and d are parameters which needs to be specified. In mechanical engineering a different form of expression 5.1 is often preferred, namely $U(z)/u_\star = \kappa^{-1} \ln(z/k_s) + B^\star$, where k_s is the so-called equivalent sand-grain roughness and $B^\star \approx 8.5$. The two expressions are equivalent, and related by $z_0 = k_s \exp(-B^\star \kappa)$.

z_0 and d values have been deduced for a variety of geophysical flows, including flows over plant canopies (Parlange and Brutsaert, 1989; Raupach et al., 1991; Böhm et al., 2013), over urban canopies (see Grimmond and Oke (1999); Barlow and Coceal (2009) for an extensive review), over snow surfaces(Clifton et al., 2008), and in pipe and channel flows (Zagarola and Smits, 1998), to name but a few. Several models have been proposed to compute z_0 and d based on the morphometric characteristics of a given surface, where important parameters are found to be the solidity λ_f (projected frontal area per unit surface area), the planar density λ_p (projected horizontal area per unit surface area), the r.m.s. of the height fluctuations (σ_h) and the skewness of the height fluctuations s_k. Among others, Brutsaert (2008) suggests $z_0 = h_0/10$ for geophysical flows, where h_0 is a characteristic height of the roughness elements, Flack and Schultz (2010) propose $k_s \approx 4.43\sigma_h(1+s_k)^{1.37}$, based on statistics of flows in fully rough regime over a variety of roughness elements, Zagarola and Smits (1998) reports $k_s = 3\sigma_h$ based on data from pipe flows with Gaussian height distributions. However, z_0 and d are hydrodynamic quantities, and thus, expressions based on purely geometrical statistics is likely to be incomplete or case specific, as stressed in Schultz and Flack (2009). Some type of flow-dependent determination is necessary.

Recently, Anderson and Meneveau (2011) proposed a new dynamic approach to determine the z_0 parameter in LES of turbulent flow over multi-scale rough topographies, which display scale-similarity over a range of length scales. In the so-called dynamic surface roughness (DSR) model (Anderson and Meneveau, 2011), the z_0 parameter is determined using the first-principles based constraint that the total momentum flux (drag) must be independent on the grid-filter scale. In traditional LES, the z_0 coefficient must be prescribed *ad hoc*, whereas the proposed dynamic approach has the advantage of determining the model coefficient at runtime, leveraging the scale-invariance of the surface height statistics, in apparent analogy to the dynamic Smagorisky model (Germano et al., 1991). The DSR model has been successfully applied to study flow over synthetic topographies, constructed as a superposition of randomly phase-shifted Fourier modes with prescribed spectral slopes (Anderson and Meneveau, 2011), to simulate flow over fluvial-like landscapes (Anderson et al., 2012) and flow over ocean waves (Yang et al., 2013). The good performance of the DSR model in such applications is due to the self-similar behavior of the underlying surfaces at the LES filter-width. Scale-similarity is in fact a typical property of natural surfaces, including evolved fluvial landscapes (Rinaldo et al., 1993; Rodriguez-Iturbe et al., 1994; Rodriguez-Iturbe and Rinaldo, 1997), wind-driven ocean surfaces (Yang et al., 2013), tree canopies (Raupach and Thom, 1981; Raupach et al., 1991; Finnigan, 2000; Böhm et al., 2013), snow surfaces (Manes et al., 2008) and snow on topography (Schirmer and Lehning, 2011). Recent analyses based on terrestrial laser scanning (Trujillo et al., 2016) have shown how sea ice surfaces are also characterized by a power-law height distribution, over a well defined range of wavelengths, spanning from the centimeter scale to tens of meters. These results have motivated the current study.

Here, we perform a series of LES of fully developed flow over high-resolution snow/ice surfaces of Antarctic sea ice floes, to determine the total surface drag and roughness parameters at process scales from 1 cm to 100 m. Simulations are performed considering a neutrally stratified atmospheric boundary layer (ABL), without rotational effects ($Ro \gg 1$), and where the flow is forced by a constant streamwise pressure gradient. A high resolution snow/ice surface morphology was obtained using a Terrestrial Laser Scanner during the SIPEX II (Sea Ice Physics and Ecosystem experiment II) research voyage to East Antarctica (September-November 2012) and processed for use in LES. The effects of large-scale features of the surface on the wind flow (those features that can be resolved in LES) are accounted for through an IBM approach. Conversely, the drag forces caused by subgrid-scale features of the surface are accounted for via the DSR model, which has been adapted for use in conjunction with the IBM.

An overview on the sea ice surfaces and on their processing for use in LES is provided in Section §2. Details on the LES, IBM and DSR algorithms is provided in §3. §4 outlines the setup of simulations and main results are presented in §5. Summary and concluding remarks follow in section §6.

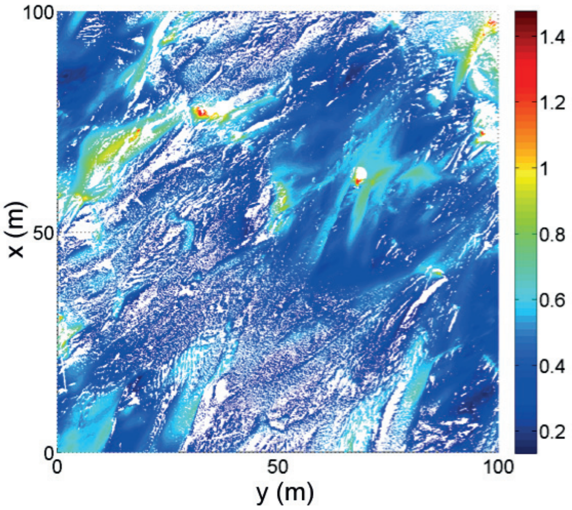

Figure 5.1 – Resulting surface from aggregation of the point cloud dataset at 1 cm resolution over a 100m × 100m area. Gaps are indicated by white areas.

5.3 Sea ice surface models and their processing for use in LES

Detailed observations of snow surface topography were made during the sea ice physics and ecosystem experiment 2 (SIPEX-2) research voyage to East Antarctica in September-November 2012. Data collection during the experiment was performed over several sea ice floes along the voyage track (ice stations). The surface considered in this study was collected on 2012-10-06 and at coordinates $65°4.678'S, 121°40.321'E$. Surface topographic information was obtained using a terrestrial laser scanner (TLS, Leica C5). The operation requires the laser scanner to be positioned at several locations to eliminate scan shade behind ridges and other surface features, resulting in an integrated 3-D model of tens of millions of point returns for areas of tens to hundreds of meters. The study area covers 100 m × 100 m, and the TLS point cloud contains over 41 million points (average density = 4100+ points per m^2). The point cloud was post-processed to generate a regular Cartesian grid characterized by 1 cm grid-stencil in the horizontal coordinate directions (displayed in Fig. 5.1). Gaps in the surface have been filled through a least squares fit on a fourth order polynomial interpolator $P_4(x, y)$ on areas of 10m × 10m. The resulting surface (Γ_b hereafter) reveals a vast amount of detail, such as small-scale ($\sim 30-50\,$cm) dune-like surface patterns, human footsteps and penguin footprints. The technological improvement that TLS provides over more traditional methods is in itself a leap forward in surveying methods in extreme environments (e.g., Williams et al. (2013))

One-dimensional power spectra of surface heights for the x (streamwise) and y (spanwise) directions are displayed in Fig. 5.2. Both spectra are characterized by a power-law behavior, with spectral slopes $\beta = -2.5$ and $\beta = -2.4$ respectively. The range of wavelengths where the

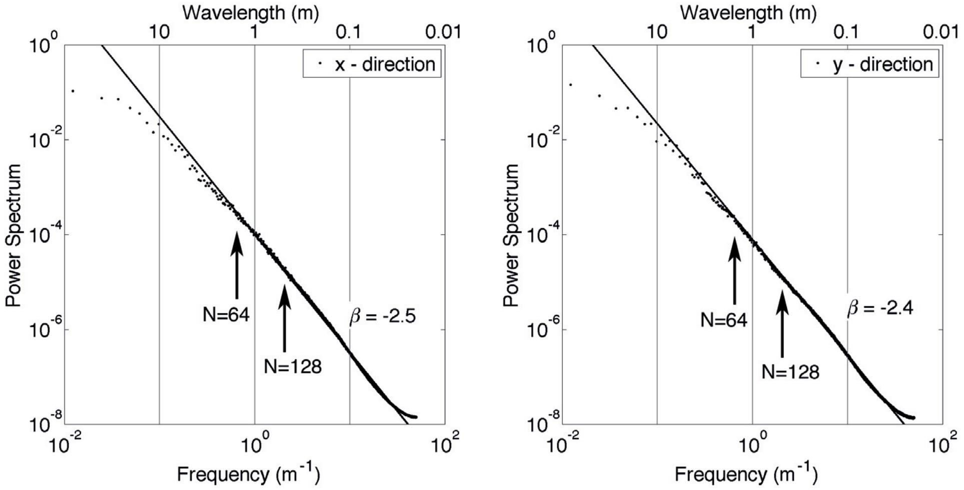

Figure 5.2 – One dimensional power spectral densities of surface heights in the x and y coordinate directions. The LES grid size is highlighted with arrows, for the two resolutions that were here considered. N denotes the number of grid nodes in the horizontal directions.

surface displays scale-similarity extends from few centimeters to tens of meters in both cases.

The LES filter width of the considered study is also displayed in Fig. 5.2, to highlight its correspondence to wavelengths in the self-similar range of the height distribution (this will have important implications for the DSR model).

For use in LES, Γ_b has been de-trended (linear trend) and spatially low-pass filtered using a top-hat filter with support corresponding to the LES filter width, i.e.

$$\tilde{\Gamma}_b = \Gamma_b * G_\Delta(x, y) \tag{5.2}$$

where $\widetilde{(\cdot)}$ denotes the spatial filtering operation, $G_\Delta(x, y)$ is the impulse response of the linear top-hat filter (of unit norm), $*$ denotes a cyclic convolution, and Δ is the LES filter width. This operation removes aliasing errors when coarse sampling at the LES grid size, and returns a periodized surface. Note that the original surface was characterized by an already negligible trend, and that the resulting periodization does not generate corners or ridges of significant height. Further, the surface was rotated, so that the x axes corresponds to the prevailing wind direction. The prevailing wind direction is determined based on the observed erosion and deposition patterns.

Variations in selected surface statistics as a function of the LES filter width are displayed in Fig. 5.3. Note the proportionality between the magnitude of the r.m.s. of the unresolved surface features σ_h^Δ and the filter width Δ. Note also the fast drop in the variance of both the x and y surface gradients. This behavior is justified if one considers that the underlying surface is characterized by $\beta \approx -2.4 \geq -3$, and thus the variance of the h-gradients is dominated by the small scales.

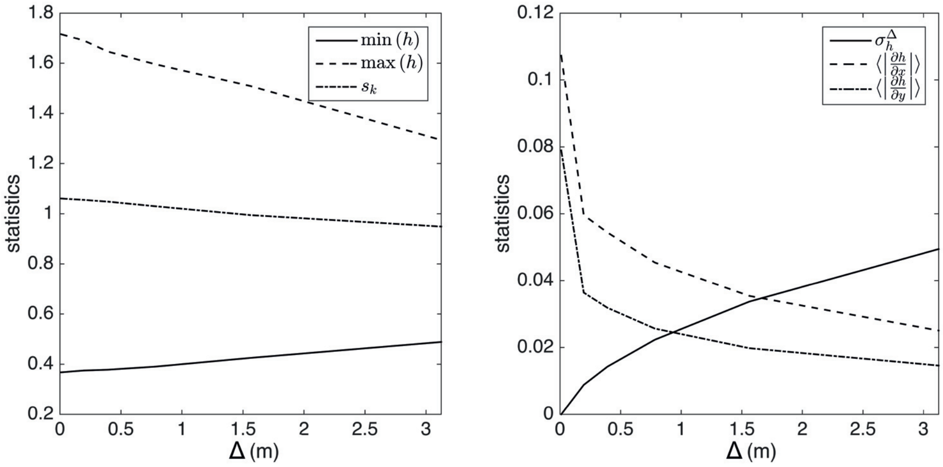

Figure 5.3 – Sea ice surface statistics as a function of the LES filter support (or grid stencil). s_k denotes the skewness of surface heights, σ_h^Δ denotes the r.m.s of the subgrid-scale surface heights.

5.4 Numerical algorithm and the Dynamic Roughness Model

5.4.1 The LES algorithm

In LES, the energy containing scales are explicitly resolved, whereas subgrid-scale (SGS) motions are modeled. The LES approach is particularly attractive if the support of the spatial filter is the inertial subrange of turbulence (Meneveau and Katz, 2000), where the scale-similarity of the flow allows simple parameterisations to be very effective.

We solve the rotational form of the iso-thermal filtered Navier-Stokes equations on a regular domain Ω:

$$\frac{\partial \tilde{u}_i}{\partial t} + \tilde{u}_j\left(\frac{\partial \tilde{u}_i}{\partial x_j} - \frac{\partial \tilde{u}_j}{\partial x_i}\right) = -\frac{\partial \tilde{\pi}}{\partial x_i} - \frac{\partial \tau_{ij}}{\partial x_j} - \frac{1}{\rho}\frac{\partial \tilde{p}_\infty}{\partial x_i}\delta_{i1}, \tag{5.3}$$

$$\frac{\partial \tilde{u}_i}{\partial x_i} = 0, \tag{5.4}$$

where x, y are the horizontal (stream-wise and span-wise) coordinates and z identifies the vertical coordinate direction, $\tilde{u}_i$ are the filtered velocity components, $\tilde{\pi}$ is a modified filtered pressure field, namely $\tilde{\pi} = \frac{\tilde{p}}{\rho} + \frac{1}{3}\tau_{ii} + \frac{1}{2}\tilde{u}_i\tilde{u}_i$, ρ is a reference density, and τ_{ij} represent the subgrid terms, which arise from the filtering operation (Pope, 2000) and $\frac{1}{\rho}\frac{\partial \tilde{p}_\infty}{\partial x_i}\delta_{i1}$ is a volumetric forcing term which is introduced to drive the flow in the x direction. Solving the Navier-Stokes equations in their rotational form ensures conservation of mass and kinetic energy (Orszag and Pao, 1975). The computational boundary is partitioned as $\partial\tilde{\Omega} = \tilde{\Gamma}_\mathrm{b} \cup \tilde{\Gamma}_\mathrm{t} \cup \tilde{\Gamma}_l$, where $\tilde{\Gamma}_\mathrm{t}$ and $\tilde{\Gamma}_l$ denote the top and lateral boundaries respectively. A free-lid boundary condition is prescribed at $\tilde{\Gamma}_\mathrm{t}$, whereas periodic boundary conditions apply in $\tilde{\Gamma}_l$ due to our Fourier partial-sum spatial expansion. $\tilde{\Gamma}_\mathrm{b}$ identifies the underlying (sea ice) surface, where a parameterised boundary condition is applied, as explained in the following.

A pseudo-spectral collocation approach (Orszag, 1969, 1970) based on truncated Fourier expansions is used in the x, y coordinate directions, whereas a second-order accurate staggered centered finite differences scheme is adopted in the vertical direction. Time integration is performed via an explicit second-order accurate Adams-Bashforth scheme and a fractional step method (Chorin, 1968; Kim and Moin, 1985) is adopted to compute the pressure field. All nonlinear terms are de-aliased through the 3/2 rule (Canuto et al., 2006), to avoid the detrimental effects induced by piling up of energy in the high wavenumber range (Kravchenko and Moin, 1997). The core of the LES algorithm was developed in (Albertson and Parlange, 1999a,b), and equipped with an IBM in Chester et al. (2007), to account for underlying surfaces / objects interacting with the flow. The code has been extensively tested in simulation of flow over rough topographies (see for instance (Bou-Zeid, 2004; Yue et al., 2007; Bou-Zeid et al., 2009; Anderson and Meneveau, 2010; Calaf et al., 2010, 2011; Hultmark et al., 2013)) and used to develop and test linear and non-linear LES subgrid-scale models (Meneveau et al., 1996; Porté-Agel et al., 2000; Porté-Agel, 2004; Bou-Zeid et al., 2005; Lu and Porté-Agel, 2010, 2013). To close the system of equations 5.3 and 5.4 we rely on the Lagrangian Scale Dependent Smagorinsky model (hereafter LASD) (Bou-Zeid et al., 2005), which was originally designed for this numerical code. Smagorinsky models are based on the concept of mixing length, and evaluate the traceless SGS stress tensor as function to the resolved strain rate tensor:

$$\tau_{ij} = -2\nu_t \tilde{S}_{ij} = -2(c_{s,\Delta}\Delta)^2 \|\tilde{S}\|_2 \tilde{S}_{ij}, \tag{5.5}$$

where ν_t represents the eddy viscosity, Δ is the filter width (usually proportional to the grid size), $\tilde{S}_{ij}$ is the filtered shear rate tensor and $c_{s,\Delta}$ is the Smagorinsky coefficient at scale Δ, to be determined. Smagorinsky models are distinguished by the way they compute $c_{s,\Delta}$. The LASD model has a number of advantages when used in simulations of wall bounded flows and when coupled with complex geometries. For instance, it allows for a dynamic evaluation of the model coefficient, thus overcoming the need to specify an *ad hoc* wall damping function (Smagorinsky, 1963; Mason and Thomson, 1992). It also accounts for a possible scale-dependency of the model coefficient (as opposite to the dynamic model of Germano et al. (1991)), which is a desirable property at the wall, where the grid size approaches the limits of the inertial subrange (Meneveau and Katz, 2000). Furthermore, the Lagrangian averaging of the model coefficient makes the model well suited for applications involving complex geometries since it preserves local variability, while overcoming the requirement of homogeneous directions. We use a Gaussian filter in conjunction with the LASD model, whose relatively compact support (in both physical and wavenumber space) reduces the Gibbs oscillations that arise when the IBM approach is coupled with pseudo-spectral algorithm (Tseng et al., 2006).

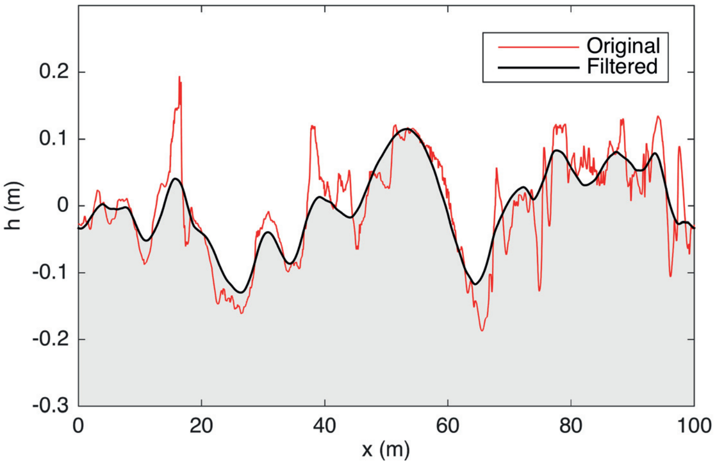

Figure 5.4 – One-dimensional transect at $y = 10$ m of the scanned sea ice surface, and equivalent transect on a filtered version of the sea ice surface (filter support $\Delta = 6.3$ m). The displayed transects have been vertically translated so that their average height equals zero.

5.4.2 The Immersed Boundary Method

As stated in the introduction, the underlying sea ice surface is accounted for through an IBM algorithm (Mohd-Yusof, 1997; Mittal and Iaccarino, 2005). $\tilde{\Gamma}_b(x, y)$ is represented implicitly as the zero level-set of a signed distance function $\tilde{\phi}(x, y, z)$, which is evaluated through a recently developed projection algorithm. The IBM algorithm is a minor modification of the Chester et al. (2007). The discrete forcing approach with indirect BC imposition results in great variations of the pressure field inside the interface ($\tilde{\phi}(x, y) < 0$), thus complicating matters for the DSR model (as elaborated in the following subsection). In the current version of the IBM, $\tilde{u}_i = 0$ is thus enforced in $\tilde{\phi} \leq 0$ as a boundary condition at time t, before advancing the solution. In Fig. 5.4 we display a one-dimensional transect of the scanned sea ice surface at 1 cm resolution, and a filtered version of it, which corresponds to the underlying surface of a LES simulation with grid stencil $\Delta = 6.3$ m. It is apparent how the filtered surface is smoother, i.e. how a significant portion of the roughness features is removed. The form drag that would have resulted from the interaction of the flow with such unresolved surface roughness needs to be accounted for through a model. To account for the SGS contribution to the total drag force, we rely on the equilibrium logarithmic law of the wall (Prandtl, 1935; Monin and Obukhov, 1954), enforced at all the collocation nodes which fall in the region $-1.1\Delta \leq \tilde{\phi} \leq 1.1\Delta$, as in Chester et al. (2007). In the specific, a local reference system is introduced: $\mathbf{e}_1 = \tilde{\mathbf{u}}_t, \mathbf{e}_2 = \tilde{\mathbf{u}} \times \tilde{\mathbf{n}}$ and $\mathbf{e}_3 = \tilde{\mathbf{n}}$, with $\mathbf{u}_t = \tilde{\mathbf{u}} - (\tilde{\mathbf{u}} \cdot \tilde{\mathbf{n}})\tilde{\mathbf{n}}$. In this coordinate system, the law of the wall is applied to compute the $\tau_{13} = \tau_{31}$ components of the Cauchy stress tensor (all other components are assumed to be zero), resulting in

$$\tau_{13} = \tau_{31} = \left(\frac{\kappa \|\tilde{\mathbf{u}}_t\|_2}{\ln(\mathrm{d}z/z_0^{\Delta})} \right)^2 , \tag{5.6}$$

where dz represent the grid stencil in the vertical direction, $\tilde{\mathbf{u}}_t$ is the tangential-to-surface velocity, evaluated at a normal-to-surface distance dz, and z_0^Δ is the hydrodynamic roughness length that is used to account for the effects of the unresolved roughness (that below scale Δ). The local stress tensor is then rotated back to the global (x, y, z) Cartesian reference system for further differentiation. To alleviate the Gibbs oscillations that arise due to the C^0 nature of the solution in an horizontal plane cutting the surface, a smooth velocity profile $\tilde{u}_i$ is generated inside the interface ($\tilde{\phi} \leq 0$) before the spectral differentiation step (Tseng et al., 2006) adopting a Laplacian smoothing operator which resembles the reconstruction scheme proposed in Cai et al. (1989) and Greer and Banerjee (1997). Other techniques are also available (Fang et al., 2011).

5.4.3 The dynamic surface roughness model

In the following, we will provide details on the dynamic surface roughness model, which was recently developed in Anderson and Meneveau (2011), and here adapted for use in conjunction with the current version of the IBM method. The low-pass filtering operation described in Sect. 5.3 decomposes the surface into a resolved and into a subgrid-scale height contribution. The filtered height distribution $\tilde{\Gamma}_{\mathrm{b}}$ is accounted for through the IBM method, whereas the effects of the SGS height contribution on the flow is modeled using the equilibrium logarithmic law of the wall (Prandtl, 1935; Monin and Obukhov, 1954) (as described above), where a hydrodynamic roughness length $z_{0,\Delta}$ has to be specified. The total force vector acting on the fluid due to the underlying surface is given by

$$F_i = \int\int_{\tilde{\Gamma}_{\mathrm{b}}} (\tilde{p}\, \tilde{n}_i)\, \mathrm{d}\tilde{\Gamma}_{\mathrm{b}} + \rho \int\int_{\tilde{\Gamma}_{\mathrm{b}}} (\tau_{ij}^{\Delta}\, \tilde{n}_j)\, \mathrm{d}\tilde{\Gamma}_{\mathrm{b}}\,, \tag{5.7}$$

where $\tilde{p}$ is the resolved pressure, $\tilde{n}_i$ is the unit normal to the filtered surface, ρ is a reference (constant) fluid density and τ_{ij}^{Δ} is the SGS kinematic surface stress, evaluated at scale Δ. In the DSR approach, $z_{0,\Delta}$ is set proportional to the r.m.s. of the (unresolved) surface roughness below scale Δ:

$$z_{0,\Delta} \equiv \sqrt{z_{0,p}^2 + (\alpha \sigma_h^{\Delta})^2}\,, \tag{5.8}$$

where $z_{0,p}$ is a regularization factor, and the dimensionless roughness parameter α is responsible to adjust the geometrical length scale (σ_h^{Δ}) to account for hydrodynamic effects. σ_h^{Δ} is evaluated as the r.m.s. of the unresolved surface height on an area of $\Delta \times \Delta$:

$$\sigma_h^{\Delta} = \frac{1}{\Delta^2} \int\int_{\Delta \times \Delta} (\widetilde{h^2} - \tilde{h}^2)\, dS\,. \tag{5.9}$$

Equation 5.8 is designed so that $z_{0,p}$ can also be regarded as a contribution from roughness at scales below the resolution of the instrument (e.g., laser scanner) that allowed to build the original surface. Throughout the study, we assume $z_{0,p} = 10^{-5} \ll \alpha \sigma_h^{\Delta}$, thus treating $z_{0,p}$ as a mere regularization factor. The unknown parameter α is evaluated dynamically by imposing a self-consistency condition on the averaged total drag force, which is assumed to be scale-invariant at the grid- and at a test-filter width, i.e. $F_i^{\Delta} = F_i^{2\Delta}$, resulting in

$$\langle \tilde{p}\,\tilde{n}_i \rangle_{\tilde{\Gamma}_\mathrm{b}} + \langle \left(\frac{\kappa\, U^{\Delta}}{\ln\left(\mathrm{d}z/z_{0,\Delta}\right)} \right)^2 \frac{\tilde{u}_i^*}{U^{\Delta}} \rangle_{\tilde{\Gamma}_\mathrm{b}} = \langle \overline{\tilde{p}}\,\overline{\tilde{n}}_i \rangle_{\overline{\tilde{\Gamma}}_\mathrm{b}} + \langle \left(\frac{\kappa\, U^{2\Delta}}{\ln\left(\mathrm{d}z/z_{0,2\Delta}\right)} \right)^2 \frac{\overline{\tilde{u}}_i^*}{U^{2\Delta}} \rangle_{\overline{\tilde{\Gamma}}_\mathrm{b}} , \tag{5.10}$$

where $\langle \cdot \rangle_{\tilde{\Gamma}_\mathrm{b}}$ and $\langle \cdot \rangle_{\overline{\tilde{\Gamma}}_\mathrm{b}}$ denotes averaging over values at $\tilde{\Gamma}_\mathrm{b}$ and $\overline{\tilde{\Gamma}}_\mathrm{b}$ respectively, $U^{\Delta}(x, y)$ and $U^{2\Delta}(x, y)$ are the resolved horizontal velocity magnitude at scale Δ and 2Δ, evaluated at a normal-to-surface distance dz, i.e.

$$U^{\Delta}(x, y) \equiv \sqrt{\tilde{u}(\tilde{\mathbf{r}})^2 + \tilde{v}(\tilde{\mathbf{r}})^2}, \qquad U^{2\Delta}(x, y) \equiv \sqrt{\overline{\tilde{u}}(\overline{\tilde{\mathbf{r}}})^2 + \overline{\tilde{v}}(\overline{\tilde{\mathbf{r}}})^2}, \tag{5.11}$$

where $\overline{(\cdot)}$ denotes filtering over horizontal planes (x, y) using a top-hat kernel with support 2Δ, and $\mathbf{r} = (x + \mathrm{d}z\, n_1, y + \mathrm{d}z\, n_2, \Gamma_\mathrm{b}(x, y) + \mathrm{d}z\, n_3)$, where n_1, n_2, n_3 are the components of the normal-to-surface vector at the surface. Further, $u_i^*(x, y) = u_i(\mathbf{r})$. At scale 2Δ we expect a reduced contribution from the resolved pressure field, and and increase in the SGS component, to result in the same overall drag force (sum of resolved + SGS).

The only unknown in Eq. 5.10 is the parameter α, which can thus be computed through a method of choice. In the current study we rely on the robust bisection method, which results in negligible computational overhead. The bisection method is initialized adopting $\alpha_1 = z_{0,p}$ and $\alpha_2 = 1$. Once α is specified, $z_{0,\Delta}$ is readily derived, to be used in Eq. 5.6 to compute the SGS surface stress tensors. Note that condition 5.10 is enforced adopting a simplified expression for the SGS drag term, which circumvents the need of mapping local reference systems with the global one for the computation of the SGS surface stress tensor, hence simplifying matters from an algorithmic perspective. Such a simplification is justified if one considers that surface gradients are small, and thus w is also expected to be relatively small, when compared against u and v, in the near surface regions.

In formulating Eq. 5.10 it is implicitly assumed that the parameter α is scale-invariant (Meneveau and Katz, 2000). Because of this, an important conceptual requirement for the DSR model, is that the LES filter width (or grid stencil) has to be in the landscape's self-similar range, where the height statistics display a scale-invariant behavior. From Fig. 5.5 is also apparent how increasing the filter support progressively removes surface features. The contribution from the IBM algorithm is thus expected to decrease as the filter width increases, and the SGS stress contribution to increase, proportionally to the support of the filter. This because the two parts of the force must still add up to the correct total value, independently of the scale.

In the current study we average quantities across the whole landscape, thus considering a single $z_{0,\Delta}$, assumed to be representative of the entire surface. This choice is motivated by the relative statistical homogeneity of the roughness features. A possible extension / improvement of the model would be to average Eq. 5.10 over smaller subregions of the surface, allowing $z_{0,\Delta}$

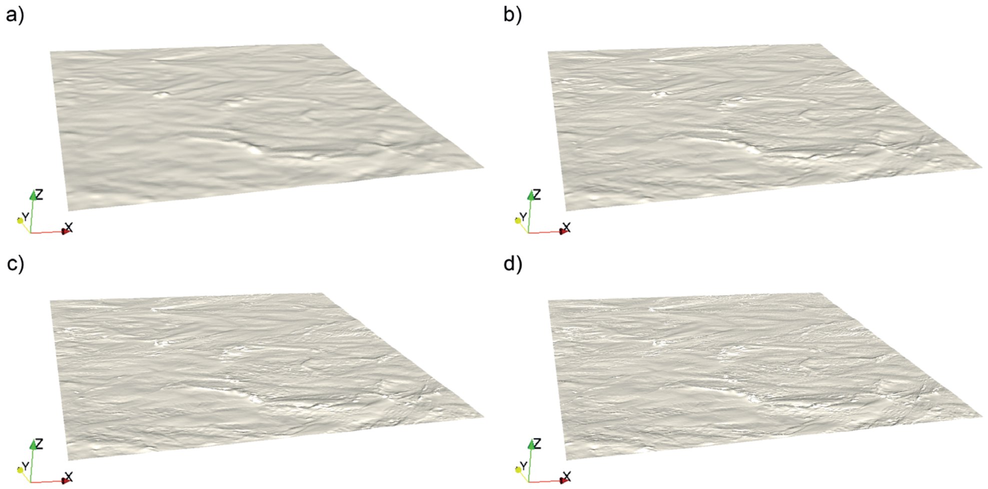

Figure 5.5 – Rendering of the periodic sea ice 100m × 100m filtered surfaces (top hat filter). Filter support is $\Delta = 1.56\,\text{m}$ (a), $\Delta = 0.78\,\text{m}$ (b), $\Delta = 0.39\,\text{m}$ (c) and $\Delta = 0.195\,\text{m}$ (d) in the x, y coordinate directions.

Label	$L_x/H \times L_y/H \times L_z/H$	$N_x \times N_y \times N_z$	Δ/H	$z_{0,\Delta}/H$
A	$16.6 \times 16.6 \times 1$	$128 \times 128 \times 64$	0.13	dynamic
B	$16.6 \times 16.6 \times 1$	$64 \times 64 \times 32$	0.26	dynamic
C	$16.6 \times 16.6 \times 1$	$128 \times 128 \times 64$	0.13	1.6×10^{-6}
D	$16.6 \times 16.6 \times 1$	$64 \times 64 \times 32$	0.26	1.6×10^{-6}

Table 5.1 – Geometry and parameters for the LES runs.

to vary in space.

5.5 Setup of simulations

Table 5.1 summarizes the setup of the current study. Four LES runs have been considered, using two different filter support. Simulations A and B make use of the DSR model, whereas simulations C and D do not, and are both characterized by a fixed $z_{0,\Delta} = z_{0,p} = 10^{-5}\,\text{m}$. The flow is forced by a constant pressure gradient $\partial_x p_\infty/\rho$, which, together with lateral periodic boundary conditions, defines a friction velocity $u_\tau = \sqrt{(\delta - d)\partial_x p_\infty/\rho} \approx 0.45$ m s^{-1}. Simulations are initialized from a logarithmic mean velocity profile, with superimposed white noise with prescribed variance, to speedup the transition to turbulence thus shortening the initial transient regime. Simulations are integrated in time for $40T$, where $T = H u_\tau^{-1}$ denotes a reference eddy turnover time. The first $20T$ are required to reach a dynamic equilibrium condition (Monin, 1977), and statistics are collected during the last $20T$. Averaging over $20T$ results in good estimates of the expected value for first and second order statistics. As in Anderson and Meneveau (2011), to preserve numerical stability of the DSR model, an initialization period of

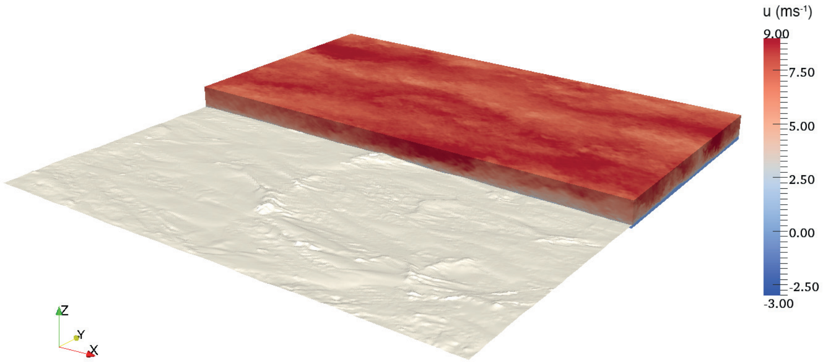

Figure 5.6 – Instantaneous (dimensional) stream-wise u velocity over the filtered sea ice surface for case A. The realization corresponds to the last simulated time step.

$0.2T$ is adopted, corresponding to the first 0.5% of the total simulation time, during which a static $\alpha = 0.3$ is adopted. Different values of the static α were found to have a negligible impact on the initial transient and on the computed statistics. Throughout the study $\langle\cdot\rangle$ will denote the double averaging (DA) operator, where averaging is performed in time and along spatial coordinates of statistical homogeneity (x, y), considering the fluid regions only (Nikora et al., 2007). Time fluctuations are written as $(\cdot)'$.

5.6 Results and discussion

Figure 5.6 displays a snapshot of the instantaneous (dimensional) stream-wise velocity field for simulation A. As typical of LES approaches, the boundary layer is populated by a broad range of scales, and is characterized by alternation of high- and low-momentum streamwise elongated streaks, apparent signature of the so-called large-scale and very large-scale organized motions (Tomkins and Adrian, 2003; Fang and Porté-Agel, 2015).

5.6.1 The DSR model

Fig. 5.7 depicts the typical dependence of the resolved, subgrid-scale, and of the resulting total kinematic momentum fluxes, as a function of the α parameter, for the grid- and test-filter scales. The solution we seek (through the bisection method) is represented by the intersection of the total momentum flux curves (occurring at $\alpha = 4.5 \times 10^{-4}$ in this specific case). Note how the resolved stress component (which does not depend on α) is reduced at the test-filter scale (2Δ), as expected, given that the filtering operation removes the highest wavenumber range of roughness features, thus resulting in a lower contribution from small-scale pressure drag. The SGS drag terms $\langle\tau_{xz}^{\Delta}\rangle_{\tilde{\Gamma}_b}$ and $\langle\tau_{xz}^{2\Delta}\rangle_{\bar{\tilde{\Gamma}}_b}$ increase as a function of α, as expected. Moreover, in the considered α range, $\langle\tau_{xz}^{2\Delta}\rangle_{\bar{\tilde{\Gamma}}_b}$ is characterized by a faster increase with respect to $\langle\tau_{xz}^{\Delta}\rangle_{\tilde{\Gamma}_b}$, thus

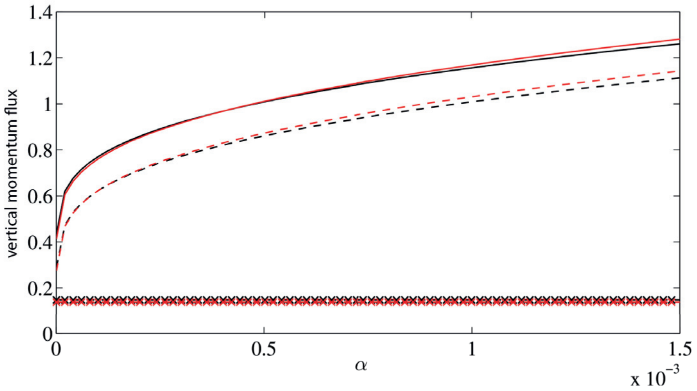

Figure 5.7 – Resolved, SGS and total (resolved+SGS) surface stress as a function of the surface roughness parameter α. Curves are representative of the last α-update step. Results are shown for both grid-filter scale (Δ) (black lines) and test-filter scale (2Δ) (red lines). Symbols: solid black lines, $\langle \tau^{\Delta}_{xz} \rangle_{\tilde{\Gamma}_\mathrm{b}} + \langle \tilde{p}_i \tilde{n}_i \rangle_{\tilde{\Gamma}_\mathrm{b}}$; dashed black lines, $\langle \tau^{\Delta}_{xz} \rangle_{\tilde{\Gamma}_\mathrm{b}}$; black crosses, $\langle \tilde{p}_i \tilde{n}_i \rangle_{\tilde{\Gamma}_\mathrm{b}}$, solid red lines, $\langle \tau^{2\Delta}_{xz} \rangle_{\overline{\tilde{\Gamma}}_\mathrm{b}} + \langle \overline{\tilde{p}}_i \overline{\tilde{n}}_i \rangle_{\overline{\tilde{\Gamma}}_\mathrm{b}}$; dashed red lines, $\langle \tau^{2\Delta}_{xz} \rangle_{\overline{\tilde{\Gamma}}_\mathrm{b}}$; red crosses, $\langle \overline{\tilde{p}}_i \overline{\tilde{n}}_i \rangle_{\overline{\tilde{\Gamma}}_\mathrm{b}}$.

allowing the total stress to match at a given α.

Fig. 5.8 displays the evolution of the roughness parameter α and of the corresponding values of the resolved and SGS stress components for simulation A. The α coefficient shows rapid convergence from the initial imposed value ($\alpha = 0.3$) to its surface-dependent range of values. Note that the displayed time steps correspond to the initial transient phase, and as apparent, both the α coefficient and the resolved and SGS kinematic stresses are characterized by a negative linear trend, underlying a slow decrease in time, toward their equilibrium value. With this regard, from Fig. 5.8 is indeed clear how the total momentum flux is out of equilibrium with respect to the imposed pressure gradient forcing, since $\langle \tilde{p}_i \tilde{n}_i \rangle_{\tilde{\Gamma}_\mathrm{b}} + \langle \tau^{\Delta}_{xz} \rangle_{\tilde{\Gamma}_\mathrm{b}} > (1/\rho)\partial \tilde{p}_\infty / \partial x$. Note however that despite the transient regime, the resolved momentum flux at scale 2Δ is consistently smaller than its counterpart at scale Δ, which results in a stable behavior of the model (no instabilities). This is in large part related to the broad support of the averaging operator, more localized averaging procedures might in fact require clipping of the α coefficient.

5.6.2 Velocity profiles

Mean stream-wise velocity profiles for cases A, B (DSR model) and C, D (no DSR model) are displayed in Fig. 5.9. Averaging is performed in time (20 T) and in space over horizontal planes using an intrinsic averaging approach (Nikora et al., 2007) (i.e. only fluid regions are considered). It is apparent how applying the DSR model results in a better collapse of velocity profiles in the logarithmic and outer layer, when compared to the cases where no DSR model is applied. When no DSR model applies, higher resolution simulations account for a larger amount of roughness features, thus resulting in enhanced surface drag, when compared to lower resolution cases. Simulation C ($N_x \times N_y \times N_z = 128 \times 128 \times 64$) is in fact characterized by

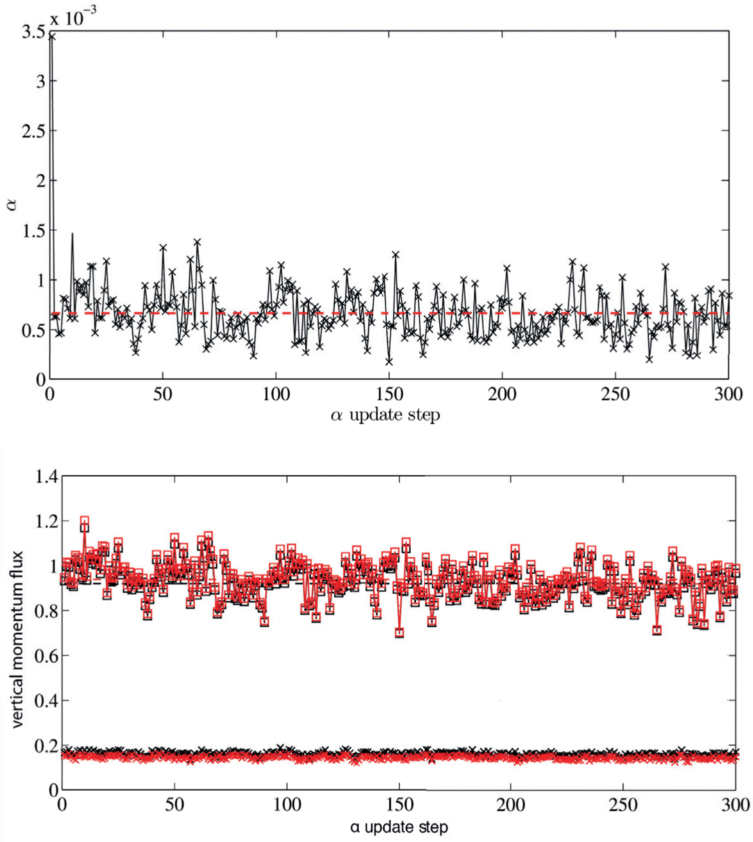

Figure 5.8 – Time evolution of the roughness parameter α (top) and corresponding values of spatially averaged kinematic surface stress components (bottom) for case A. Symbols: black squares, $\langle \tau^{\Delta}_{xz} \rangle_{\tilde{\Gamma}_{\mathrm{b}}}$; red squares, $\langle \tau^{2\Delta}_{xz} \rangle_{\bar{\tilde{\Gamma}}_{\mathrm{b}}}$; black crosses, $\langle \tilde{p}_i \tilde{n}_i \rangle_{\tilde{\Gamma}_{\mathrm{b}}}$; red crosses, $\langle \bar{\tilde{p}}_i \bar{\tilde{n}}_i \rangle_{\bar{\tilde{\Gamma}}_{\mathrm{b}}}$. α is updated every 10 LES time steps, thus the displayed plot accounts for the first 3000 simulation steps after the DSR model has been activated (corresponding to 0.75% of the total simulation time).

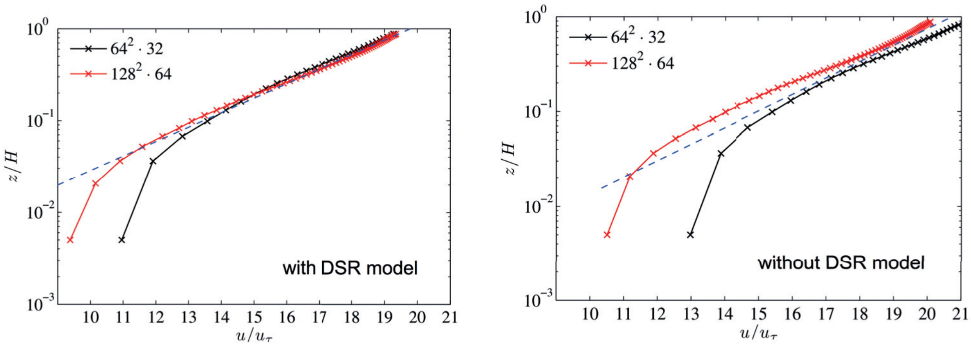

Figure 5.9 – Averaged stream-wise velocity profile for cases A,B (left) and C,D (right).

a relatively weaker mean flow with respect to case D ($N_x \times N_y \times N_z = 64 \times 64 \times 32$). When the DSR model is applied, velocity profiles are very similar at the two considered scales (Δ and 2Δ), confirming the enhanced contribution of SGS momentum fluxes as the LES filter width increases, thus resulting in a grid-independent surface drag force.

Based on current simulations, we report a preliminary value of $\alpha = 3.5 \times 10^{-4}$ for the considered sea ice surfaces, for flow along the prevailing wind direction. This value is consistent across the considered resolutions, confirming the scale-invariance of the model coefficient, thus indirectly validating the LES+IBM+DSR approach. It is also notable how the resulting roughness parameter α is of the same order of magnitude of that reported in Anderson and Meneveau (2011) for the same spectral slope. Anderson and Meneveau (2011) report $\alpha = \mathcal{O}(10^{-4})$ for LES of turbulent flow at $Re \rightarrow \infty$ over synthetically generated surfaces characterized by a spectral slope $\beta = -2.4$. This indirectly confirms the good performance of the considered IBM and of the SGD (Anderson and Meneveau, 2010) methods in accurately accounting for the aggregate effects of roughness features that fall into the resolvable range of scales for LES.

5.7 Summary and conclusions

The current study has focused on characterizing roughness properties of Antarctic sea ice floes via large-eddy simulation of fully developed boundary-layer flow. Snow/ice surface morphology was obtained using a terrestrial laser scanner during the SIPEX II (sea ice physics and ecosystem experiment II) research voyage to East Antarctica (September-November 2012), and has been mapped to a 100m × 100m Cartesian grid at 1 cm resolution. Surface topography is characterized by a power-law height distribution over a wide range of scales (from a few cm to tens of meters), with spectral slope $\beta \approx -2.4$. Current LES resolution is not capable of resolving the flow down to the smallest roughness features, thus requiring a low-pass filtering of the underlying surface, for use in simulations (to avoid aliasing errors). The range of roughness scales directly representable through the LES grid is accounted for through an IBM algorithm, whereas drag effects associated with unresolved roughness modes are parameterized through a recently developed DSR model, which has been here adapted for use in conjunction with the IBM. The DSR model is based on Monin-Obukhov similarity theory to parameterize the drag from SGS roughness, and evaluates the $z_{0,\Delta}$ parameter dynamically, based on the self-consistency condition that total drag is independent on the grid-filter scale. The dynamic surface roughness model is inspired by the Germano identity, traditionally used to determine model parameters for closing subgrid-scale stresses in the bulk of a turbulent flow, and overcomes the need to specify a-priory a $z_{0,\Delta}$, which for sea ice surfaces is not known.

The proposed DSR model is found to be robust, requiring no clipping of the α parameter, and leads to accurate flow predictions (resolution invariant). The resulting estimate of the model parameter is $\alpha = 3.5 \times 10^{-4}$. α can be used to prescribe the hydrodynamic roughness length $z_{0,\Delta}$ in simulations based on purely geometrical statistics of the underlying sea ice surface, thus greatly simplifying matters. Surface drag over sea ice is of primary control on sea ice flow patterns and deformations at scales that are important for climate and weather prediction models. Therefore, an accurate specification of the hydrodynamic roughness length $z_{0,\Delta}$ is of great importance. Specification of the surface roughness parameter for sea ice surfaces over a broader range of spectral slopes and approaching wind directions is the subject of current research.

Bibliography

J. D. Albertson and M. B. Parlange. Surface length scales and shear stress: implications for land-atmosphere interaction over complex terrain. *Water Resour Res*, 35(7):2121–2132, 1999a.

J. D. Albertson and M. B. Parlange. Natural integration of scalar fluxes from complex terrain. *Adv Water Resour*, 23(3):239–252, 1999b.

C. Amory, F. Naaim-Bouvet, H. Gallée, and E. Vignon. Two cases of aerodynamic adjustment of sastrugi. *Cryosph Discuss*, 9(6):6003–6024, 2015.

W. Anderson and C. Meneveau. A large-eddy simulation model for boundary-layer flow over surfaces with horizontally resolved but vertically unresolved roughness elements. *Boundary-Layer Meteorol*, 137(3):397–415, 2010.

W. Anderson and C. Meneveau. Dynamic roughness model for large-eddy simulation of turbulent flow over multiscale, fractal-like rough surfaces. *J Fluid Mech*, 679:288–314, 2011.

W. Anderson, P. Passalacqua, F. Porté-Agel, and C. Meneveau. Large-eddy simulation of atmospheric boundary-layer flow over fluvial-like landscapes using a dynamic roughness model. *Boundary-Layer Meteorol*, 144(2):263–286, 2012.

W. Anderson, Q. Li, and E. Bou-Zeid. Numerical simulation of flow over urban-like topographies and evaluation of turbulence temporal attributes. *J Turbul*, 16(9):809–831, 2015.

J. F. Barlow and O. Coceal. A review of urban roughness sublayer turbulence. *Report*, (527): 1–69, 2009.

M. Böhm, J. J. Finnigan, M. R. Raupach, and D. Hughes. Turbulence structure within and above a canopy of bluff elements. *Boundary-Layer Meteorol*, 146(3):393–419, 2013.

E. Bou-Zeid. Large-eddy simulation of neutral atmospheric boundary layer flow over heterogeneous surfaces: blending height and effective surface roughness. *Water Resour Res*, 40(2), 2004.

E. Bou-Zeid, C. Meneveau, and M. B. Parlange. A scale-dependent Lagrangian dynamic model for large eddy simulation of complex turbulent flows. *Phys Fluids*, 17(2):025105, 2005.

E. Bou-Zeid, J. Overney, B. D. Rogers, and M. B. Parlange. The effects of building representation and clustering in large-eddy simulations of flows in urban canopies. *Boundary-Layer Meteorol*, 132(3):415–436, 2009.

W. Brutsaert. *Hydrology: An Introduction. 3rd ed.* 2008.

W. Cai, D. Gottlieb, and C. Shu. Essentially nonoscillatory spectral Fourier methods for shock wave calculations. *Math Comput*, 52(186):389–410, 1989.

M. Calaf, C. Meneveau, and J. Meyers. Large eddy simulation study of fully developed wind-turbine array boundary layers. *Phys Fluids*, 22(1):015110, 2010.

M. Calaf, M. B. Parlange, and C. Meneveau. Large eddy simulation study of scalar transport in fully developed wind-turbine array boundary layers. *Phys Fluids*, 23(12):126603, 2011.

C. Canuto, M. Y. Hussaini, A. Quarteroni, and T. A. Zang. *Spectral methods*. Scientific Computation. Springer Berlin Heidelberg, Berlin, Heidelberg, 2006.

I. P. Castro. Rough-wall boundary layers: mean flow universality. *J Fluid Mech*, 585:469, 2007.

H. Cheng and I. P. Castro. Near wall flow over urban-like roughness. *Boundary-Layer Meteorol*, 104(2):229–259, 2002.

H. Cheng, P. Hayden, A. G. Robins, and I. P. Castro. Flow over cube arrays of different packing densities. *J Wind Eng Ind Aerodyn*, 95(8):715–740, 2007.

S. Chester and C. Meneveau. Renormalized numerical simulation of flow over planar and non-planar fractal trees. *Environ Fluid Mech*, 7(4):289–301, 2007.

S. Chester, C. Meneveau, and M. B. Parlange. Modeling turbulent flow over fractal trees with renormalized numerical simulation. *J Comput Phys*, 225(1):427–448, 2007.

A. J. Chorin. Numerical solution of the Navier-Stokes equations. *Math Comput*, 22(104): 745–762, 1968.

A. Clifton, C. Manes, J. D. Rüedi, M. Guala, and M. Lehning. On shear-driven ventilation of snow. *Boundary-Layer Meteorol*, 126:249–261, 2008.

H. Eicken, M. A. Lange, and P. Wadhams. Characteristics and distribution patterns of snow and meteoric ice in the Weddell Sea and their contribution to the mass balance of sea ice. *Annu Geophys*, 12(1):80–93, 1994.

J. Fang and F. Porté-Agel. Large-eddy simulation of very-large-scale motions in the neutrally stratified atmospheric boundary layer. *Boundary-Layer Meteorol*, 155(3):397–416, 2015.

J. Fang, M. Diebold, C. Higgins, and M. B. Parlange. Towards oscillation-free implementation of the immersed boundary method with spectral-like methods. *J Comput Phys*, 230(22): 8179–8191, 2011.

J. Finnigan. Turbulence in plant canopies. *Annu Rev Fluid Mech*, 32(1):519–571, 2000.

K. A. Flack and M. P. Schultz. Review of hydraulic roughness scales in the fully rough regime. *Journal of Fluids Engineering*, 132(4):041203, 2010.

M. Germano, U. Piomelli, P. Moin, and W. Cabot. A dynamic subgrid-scale eddy viscosity model. *Phys Fluids*, 3(7):1760–1765, 1991.

J. Greer and S. Banerjee. Exponentially accurate approximations to piece-wise smooth periodic functions. *J Sci Comput*, 12(3):253–287, 1997.

C. S. B. Grimmond and T. R. Oke. Aerodynamic properties of urban areas derived from analysis of surface form. *J Appl Meteorol*, 38(9):1262–1292, 1999.

C. D. Groot Zwaaftink, M. Diebold, S. Horender, J. Overney, G. Lieberherr, M. B. Parlange, and M. Lehning. Modelling small-scale drifting snow with a Lagrangian stochastic model based on large-eddy simulations. *Boundary-Layer Meteorol*, 153(1):117–139, 2014.

P. R. Holland, N. Bruneau, C. Enright, M. Losch, N. T. Kurtz, and R. Kwok. Modeled trends in Antarctic sea ice thickness. *J Clim*, 27(10):3784–3801, 2014.

M. Hultmark, M. Calaf, and M. B. Parlange. A new wall shear stress model for atmospheric boundary layer simulations. *J Atmos Sci*, 70(11):3460–3470, 2013.

J. Jimenez. Turbulent flows over rough walls. *Annu Rev Fluid Mech*, 36(1):173–196, 2004.

J. Kim and P. Moin. Application of a fractional-step method to incompressible Navier-Stokes equations. *J Comput Phys*, 59(2):308–323, 1985.

N. Kimura, A. Nishimura, Y. Tanaka, and H. Yamaguchi. Influence of winter sea-ice motion on summer ice cover in the Arctic. *Polar Research*, 32:1–8, 2013.

T. Kono, T. Tamura, and Y. Ashie. Numerical investigations of mean winds within canopies of regularly arrayed cubical buildings under neutral stability conditions. *Boundary-Layer Meteorol*, 134(1):131–155, 2010.

A. G. G. Kravchenko and P. Moin. On the effect of numerical errors in large eddy simulations of turbulent flows. *J Comput Phys*, 131(2):310–322, 1997.

K. C. Leonard and T. Maksym. The importance of wind-blown snow redistribution to snow accumulation on Bellingshausen Sea ice. *Annu Glaciol*, 52(57):271–278, 2011.

H. Lu and F. Porté-Agel. A modulated gradient model for large-eddy simulation: Application to a neutral atmospheric boundary layer. *Phys Fluids*, 22(1):015109, 2010.

H. Lu and F. Porté-Agel. A modulated gradient model for scalar transport in large-eddy simulation of the atmospheric boundary layer. *Phys Fluids*, 25(1):015110, 2013.

C. Manes, M. Guala, H. Löwe, S. Bartlett, L. Egli, and M. Lehning. Statistical properties of fresh snow roughness. *Water Resour Res*, 44(11), 2008.

P. J. Mason and D. J. Thomson. Stochastic backscatter in large-eddy simulations of boundary layers. *J Fluid Mech*, 242:51–78, 1992.

C. Meneveau and J. Katz. Scale-invariance and turbulence models for large-eddy simulation. *Annu Rev Fluid Mech*, 32(1):1–32, 2000.

C. Meneveau, T. S. Lund, and W. H. Cabot. A Lagrangian dynamic subgrid-scale model of turbulence. *J Fluid Mech*, 319:353–385, 1996.

E. Mignot, E. Barthélemy, and D. Hurther. Turbulent kinetic energy budget in a gravel-bed channel flow. *Acta Geophys*, 56(3):601–613, 2008.

E. Mignot, E. Barthelemy, and D. Hurther. Double-averaging analysis and local flow characterization of near-bed turbulence in gravel-bed channel flows. *J Fluid Mech*, 618:279–303, 2009.

R. Mittal and G. Iaccarino. Immersed boundary methods. *Annu Rev Fluid Mech*, 37(1):239–261, 2005.

J. Mohd-Yusof. Combined immersed-boundary/B-spline methods for simulations of flow in complex geometries. *Annual Research Briefs. NASA Ames Research Center*, pages 317–327, 1997.

A. S. Monin. *Statistical fluid mechanics: The mechanics of turbulence*, volume 45. 1977.

A. S. Monin and A. M. Obukhov. Basic laws of turbulent mixing in the surface layer of the atmosphere. *Contrib. Geophys. Inst. Acad. Sci. USSR*, 24(151):163–187, 1954.

M. Nicolaus, C. Haas, and J. Bareiss. Observations of superimposed ice formation at melt-onset on fast ice on Kongsfjorden, Svalbard. *Phys Chem Earth*, 28:1241–1248, 2003.

M. Nicolaus, C. Katlein, J. Maslanik, and S. Hendricks. Changes in Arctic sea ice result in increasing light transmittance and absorption. *Geophys Res Lett*, 39(24), 2012.

V. Nikora, D. Goring, I. McEwan, and G. Griffiths. Spatially averaged open-channel flow over rough bed. *J Hydraul Eng*, 127(2):123–133, 2001.

V. Nikora, K. Koll, I. McEwan, S. McLean, and A. Dittrich. Velocity distribution in the roughness layer of rough-bed flows. *J Hydraul Eng*, 130(10):1036–1042, 2004.

V. Nikora, S. McLean, S. Coleman, D. Pokrajac, I. McEwan, L. Campbell, J. Aberle, D. Clunie, and K. Koll. Double-averaging concept for rough-bed open-channel and overland flows: theoretical background. *J Hydraul Eng*, 133(8):884–895, 2007.

J. Nikuradse. *Laws of flow in rough pipes*, volume 3. VDI-Forschungsheft 361, 1950.

F. Obleitner. Measurement and simulation of snow and superimposed ice at the Kongsvegen glacier, Svalbard (Spitzbergen). *J Geophys Res*, 109(D4):D04106, 2004.

S. A. Orszag. Numerical methods for the simulation of turbulence. *Phys Fluids*, 12(12):II–250, 1969.

S. A. Orszag. Transform method for the calculation of vector-coupled sums: application to the spectral form of the vorticity equation. *J Atmos Sci*, 27(6):890–895, 1970.

S. A. Orszag and Y. H. Pao. Numerical computation of turbulent shear flows. In *Adv Geophys*, volume 18 of *Advances in Geophysics*, pages 225–236. Elsevier, 1975.

L. Papritz, S. Pfahl, H. Sodemann, and H. Wernli. A climatology of cold air outbreaks and their impact on air–sea heat fluxes in the high-latitude south Pacific. *J Clim*, 28(1):342–364, 2015.

M. B. Parlange and W. Brutsaert. Regional roughness of the landes forest and surface shear stress under neutral conditions. *Boundary-Layer Meteorol*, 48(1):69–81, 1989.

S. B. Pope. *Turbulent flows*. Cambridge University Press, 2000.

F. Porté-Agel. A scale-dependent dynamic model for scalar transport in large-eddy simulations of the atmospheric boundary layer. *Boundary-Layer Meteorol*, 112(1):81–105, 2004.

F. Porté-Agel, C. Meneveau, and M. B. Parlange. A scale-dependent dynamic model for large-eddy simulation: application to a neutral atmospheric boundary layer. *J Fluid Mech*, 415: 261–284, 2000.

L. Prandtl. *The mechanics of viscous fluids (aerodynamic theory)*, volume 3. Springer, 1935.

M. R. Raupach and A. S. Thom. Turbulence in and above plant canopies. *Annu Rev Fluid Mech*, 13(1):97–129, 1981.

M. R. Raupach, R. A. Antonia, and S. Rajagopalan. Rough-wall turbulent boundary layers. *Appl Mech Rev*, 44(1):1–25, 1991.

A. Rinaldo, I. Rodriguez-Iturbe, R. Rigon, E. Ijjasz-Vasquez, and R. L. Bras. Self-organized fractal river networks. *Phys Rev Lett*, 70(6):822–825, 1993.

I. Rodriguez-Iturbe and A. Rinaldo. *Fractal river basins: chance and self-organization*. Cambridge University Press, 1997.

I. Rodriguez-Iturbe, M. Marani, R. Rigon, and A. Rinaldo. Self-organized river basin landscapes: Fractal and multifractal characteristics. *Water Resour Res*, 30(12):3531–3539, 1994.

M. Schirmer and M. Lehning. Persistence in intra-annual snow depth distribution: 2. Fractal analysis of snow depth development. *Water Resour Res*, 47(9), 2011.

H. Schlichting. Experimentelle untersuchungen zum rauhigkeitsproblem, 1936.

M. P. Schultz and K. A. Flack. Turbulent boundary layers on a systematically varied rough wall. *Phys Fluids*, 21(1):015104, 2009.

I. Simmonds. Comparing and contrasting the behaviour of Arctic and Antarctic sea ice over the 35 year period 1979–2013. *Annu Glaciol*, 56(69):18–28, 2015.

J. Smagorinsky. General circulation experiments with the primitive equations. *Mon Weather Rev*, 91(3):99–164, 1963.

A. Stössel, Z. Zhang, and T. Vihma. The effect of alternative real-time wind forcing on Southern Ocean sea ice simulations. *J Geophys Res*, 116(C11):C11021, 2011.

C. D. Tomkins and R. J. Adrian. Spanwise structure and scale growth in turbulent boundary layers. *J Fluid Mech*, 490:37–74, 2003.

E. Trujillo, K. Leonard, T. Maksym, and M. Lehning. Changes in snow distribution and surface topography following a snowstorm on Antarctic sea ice. *J Geophys R, Submitt*, 2016.

Y. H. Tseng, C. Meneveau, and M. B. Parlange. Modeling flow around bluff bodies and predicting urban dispersion using large eddy simulation. *Environmental Science & Technology*, 40 (8):2653–2662, 2006.

P. Uotila, P. R. Holland, T. Vihma, S. J. Marsland, and N. Kimura. Is realistic Antarctic sea-ice extent in climate models the result of excessive ice drift? *Ocean Modelling*, 79:33–42, 2014.

G. D. Williams, T. Maksym, C. Kunz, P. Kimball, H. Singh, J. Wilkinson, T. Lachlan-Cope, E. Trujillo, A. Steer, Rob Massom, Klaus Meiners, Petra Heil, Jan Lieser, Katherine Leonard, and Chris Murphy. Beyond point measurements: Sea ice floes characterized in 3-D. *Eos, Transactions American Geophysical Union*, 94(7):69–70, 2013.

Z. Xie and I. P. Castro. LES and RANS for turbulent flow over arrays of wall-mounted obstacles. *Flow, Turbul Combust*, 76(3):291–312, 2006.

Z. T. Xie and I. P. Castro. Large-eddy simulation for flow and dispersion in urban streets. *Atmos Environ*, 43(13):2174–2185, 2009.

D. Yang, C. Meneveau, and L. Shen. Dynamic modelling of sea-surface roughness for large-eddy simulation of wind over ocean wavefield. *J Fluid Mech*, 726:62–99, 2013.

X. I. A. Yang, J. Sadique, R. Mittal, and C. Meneveau. Exponential roughness layer and analytical model for turbulent boundary layer flow over rectangular-prism roughness elements. *J Fluid Mech*, 789:127–165, 2016.

J. Yuan and U. Piomelli. Numerical simulations of sink-flow boundary layers over rough surfaces. *Phys Fluids*, 26(1), 2014.

W. Yue, M. B. Parlange, C. Meneveau, W. Zhu, R. Hout, and J. Katz. Large-eddy simulation of plant canopy flows using plant-scale representation. *Boundary-Layer Meteorol*, 124(2): 183–203, 2007.

M. V. Zagarola and A. J. Smits. Mean-flow scaling of turbulent pipe flow. *J Fluid Mech*, 373: 33-79, 1998.

J. Zhang. Modeling the impact of wind intensification on Antarctic sea ice volume. *J Clim*, 27 (1):202–214, 2014.

6 Conclusions and Perspectives

Land-atmosphere interactions occur mostly over complex terrain, resulting in a broad variety of phenomena governing the exchange of energy and mass between the ABL and the underlying surface. In this thesis, two among the relevant phenomena were characterized, namely that of slope flows, and ABL flow over multi-scale rough topographies.

In Chapter 2 a closed form analytic solution of the steady-state Prandtl model equations was derived, valid for spatially varying eddy diffusivities (O'Briens type) and arbitrary constant Prandtl number. The resulting velocity and buoyancy profiles show significant variations in both phase and amplitude of minima and maxima compared to the classic constant eddy viscosity model and the more recent (approximate) WKB solutions, thus shedding new light on the problem. The near wall region is characterized by a relatively stronger surface inversion and velocity gradients, the LLJ is further displaced toward the surface, with peak velocity strongly depending on the model parameters. The proposed solution has the potential to be used as surface closure in large-scale models, as an alternative to MOST.

In Chapter 3 DNS was employed to characterize the turbulent structure of slope flows and to determine the sensitivity of the solution to variations in the parameter space. Simulations were performed within the conceptual framework of the Prandtl model, with focus on variations in the mean flow, second order statistics, and MKE and TKE budget terms, as a function of the sloping angle α and Reynolds number Re. Turbulent anabatic and katabatic regimes were found to be structurally similar at high sloping angles, qualitatively resembling the Prandtl solution, but to undergo a different transition as the sloping angle decreases, leading to stark statistical differences when $\alpha \lessapprox 30^\circ$. No region with constancy (even approximate) of fluxes with distance from the wall was observed (basic requirement for MOST to hold). A subdivision of the boundary layer was also proposed, based on analysis of the TKE budget terms: 1. an *outer layer*, where turbulent transport balances dissipation, 2. an *intermediate layer*, where shear and buoyant production overcome dissipation, and turbulent and pressure fluctuations are responsible for relocating the excess of TKE, and 3. a *wall layer*, capped by the jet, where pressure and turbulent transport balance dissipation and viscous diffusion of TKE. Results complement previous findings on the topic (Fedorovich and Shapiro, 2009a,b), and provide insight on the system that are of great importance toward the development of reliable parameterizations for use in LES and lower dimensional models (such as the one proposed in Chapter 2).

Chapter 4 further explored the structure of turbulence in slope flows. Statistical analysis and identification criteria were combined to characterize coherent energetic motions in katabatic flows over steep slopes, within the DNS framework of Chapter 3. Coherent structures proved to be strongly dependent on the slope angle. LSMs were persistently observed over the considered range of sloping angles, characterized by a streamwise extension in the order of the boundary layer thickness (δ). A second low-wavenumber mode characterized pre-multiplied spectra and co-spectra when the slope angle was below 70 degrees, indicative of VLSMs, with a streamwise extension of about 10δ, contributing to the turbulent kinetic energy and shear stress in the above-jet regions up to 30% and 45%. LSMs and VLSMs were found to arise due to streamwise alignment and concatenation of packets of hairpins, characterized by a head located upstream in the return flow region and by tails protruding downstream into the inner regions of the flow. Based on such hairpin paradigm, LSMs and VLSMs can be regarded as the observed high momentum regions, flanked on each side by relatively broader regions of low momentum fluid, also induced by rotation of the hairpin legs.

In Chapter 5, a recently developed DSR model was adapted for use in conjunction with the immersed boundary method IBM to characterize surface drag and roughness properties of multi-scale sea ice surfaces. Snow/ice surface morphology was obtained using a terrestrial laser scanner during the SIPEX II (sea ice physics and ecosystem experiment II) research voyage to East Antarctica (September-November 2012), and has been mapped to a 100m × 100m Cartesian grid at 1 cm resolution. LES of fully developed ABL flow were performed, relying on an IBM approach to represent large-scale surface features (the features that can be resolved in LES). Conversely, the drag forces caused by subgrid-scale surface features were accounted for through a DSR model, adapted for use in conjunction with the IBM. The DSR model represents a major step forward in the study of flow over multi-scale rough surfaces. It is based on Monin-Obukhov similarity theory to parameterize the drag from SGS roughness, and evaluates the $z_{0,\Delta}$ parameter dynamically, based on the self-consistency condition that total drag is independent on the filter scale. An important conceptual requirement for the DSR model to perform well, is that the grid- and test-filter scales have to be within the scale-invariant range of the surface height distribution. Given the wide range of scales where sea ice floes display a power-law height distribution (from a few cm to tens of meters), such an approach is deemed as a successful avenue for future research. In the specific case considered herein, the model generated accurate flow predictions (resolution invariant), and yielded a well-defined, rapidly converging, roughness parameter ($\alpha = 3.5 \times 10^{-4}$). Knowledge of the roughness parameter α is of great use in climate, weather prediction and scalar transport models, because it allows to evaluate the hydrodynamic roughness length (z_0) of sea ice surfaces, based on available geometrical statistics.

With regard to slope flows, this dissertation has provided relevant insight on the physical mechanisms sustaining mean flow and turbulence. Beyond some apparent (but not straightforward) further research directions, such as confirming observed trends over a broader range of Reynolds numbers, perhaps the most relevant future development may be deriving a reliable parameterization of turbulent effects on the flow, of use in LES and in lower dimensional models. For instance, an accurate model for the eddy viscosity and diffusivity coefficients for anabatic and katabatic flows would represent a first important step toward the development of a near-surface closure. Other possible research directions include using the setup of Chapters 3 and 4 to gain insight on coherent motions populating anabatic flows, and katabatic flows in the lower range of sloping angles, although the latter would require a larger domain and hence be very expensive from a computational perspective. Thus far, slope flows over an hydraulically smooth surface have been considered. Further developments include accounting for explicitly resolved roughness elements, and for the presence of canopies in the slope, where radiative transfer schemes in the canopy layer will be explicitly needed and considered.

Further research directions with regard to LES of flow over multi-scale rough surfaces include generalizing the DSR model to account for spatial variability of the model coefficient, and for its possible scale dependency. Spatial variations in the dimensionless roughness parameter α would allow to account for heterogeneity of the underlying surface, in terms of roughness properties, but also in terms of hydrodynamic regimes within the same surface. SGS effects in regions of attached flow might in fact result in different α values, when compared to that characterizing SGS effects in the wake of roughness elements. In Porté-Agel et al. (2000) the scale-invariant dynamic Smagorinsky model was generalized to account for scale dependency of the model coefficient, and yielded a better approximation of SGS effects in the bulk of a turbulent flow, when the filter width was in the energy containing range of scales (away from the self-similar inertial range). Accordingly, a further research direction would be to generalize the DSR model to account for scale dependency of the model coefficient, according to some functionality whose parameters have to be determined dynamically. This would likely yield a more accurate approximation of the SGS drag contribution, especially when the LES filter width is not in the self-similar range of scales.

Bibliography

E. Fedorovich and A. Shapiro. Turbulent natural convection along a vertical plate immersed in a stably stratified fluid. *J Fluid Mech*, 636:41–57, 2009a.

E. Fedorovich and A. Shapiro. Structure of numerically simulated katabatic and anabatic flows along steep slopes. *Acta Geophys*, 57(4):981–1010, 2009b.

F. Porté-Agel, C. Meneveau, and M. B. Parlange. A scale-dependent dynamic model for large-eddy simulation: application to a neutral atmospheric boundary layer. *J Fluid Mech*, 415: 261–284, 2000.

Marco Giovanni Giometto

Ch. de Champ Rond 36b

1010 Lausanne, Switzerland

mgiometto@gmail.com

Italian, born 1985

Languages: Italian (native), English (proficient), Spanish (proficient), French (basic)

Research interests:

Complex systems, fluid mechanics, numerical methods, boundary-layer flows, thermally driven flows.

Education

- **2016:** Ph.D. in Mechanical Engineering, École Polytechnique Fédérale de Lausanne, EPFL, laboratory of Environmental Fluid Mechanics (EFLUM), Switzerland;
- **2014:** Ph.D. in Civil and Environmental Engineering (Summa cum Laude), Braunschweig TU University and University of Florence (International Ph.D. program);
- **2010:** M.Sc., Civil Engineering (Summa cum Laude), Padua University, Italy;
- **2007:** B.Sc., Civil Engineering, Padua University, Italy.

Grants and Awards

- **2015:** Best oral presentation award. 9th International conference on urban climate, 12th Symposium on the urban environment, Toulouse, France. The related paper was selected to appear in the IAUC's newsletter, Urban Climate News;
- **2015:** Third prize in the animation category of the 2015 Application-Centered Computational Engineering Science Visualization Contest, École Polytechnique Fédérale de Lausanne, Switzerland;
- **2015:** Grant for production project "Study of land-atmosphere interaction over Antarctic snow-ice formations by large-eddy simulation", CSCS Supercomputing Center, Lugano, Switzerland;
- **2014:** Outstanding Student Paper Award. AGU General Assembly Conference, San Francisco, USA;
- **2012:** Grant for validation of the Kratos Multiphysics Software for the study the aeroelastic behavior of bridge sections forced by homogeneous turbulent flows (12'000 Euro), University of Padua, Italy;
- **2011:** Ph.D. scholarship at Braunschweig TU University and Università di Firenze (joint Ph.D. program);

- **2010:** Scholarship from the bank Banca San Giorgio Quinto e Valle Agno, "Progetto Erasmus";
- **2010:** Erasmus scholarship for the development of M.Sc. thesis at the Center for Numerical Methods in Engineering, Barcelona, Spain.

Workshops and Summer Schools

- **2013:** Workshop on Intel VTune**,** Dept. of Information Technology at École Polytechnique Fédérale de Lausanne, Lausanne, Switzerland;
- **2013:** Summer school "Unsteady Simulations for Industrial Flows", Dept. of Applied Mechanics, Chalmers University of Technology, Gothenburg, Sweden;
- **2013:** Summer school "Fluid Dynamics of Sustainability and the Environment", Dept. of Applied Mathematics & Theoretical Physics, Cambridge, UK;
- **2012:** Convention "Advances and Applications of GiD", International Center for Numerical Methods in Engineering, Barcelona, Spain;
- **2012:** Summer school "Environmental Fluid Mechanics", Dept. of Environmental Engineering, University of Trento, Italy.

Publications in peer-reviewed journals

1. M. G. Giometto, A. Christen, C. Meneveau, J. Fang, M. Krafczyk, M. B. Parlange. Spatial characteristics of roughness sublayer mean flow and turbulence over a realistic urban surface. Boundary Layer Meteorology, in review (2016);
2. M. G. Giometto, R. Grandi, J. Fang, and M. B. Parlange. . On the solution of katabatic flows with spatially varying eddy viscosity and diffusivity. Boundary Layer Meteorology, in review (2016);
3. M. G. Giometto, J. Fang, G. G. Katul, and M. B. Parlange. Direct numerical simulation of slope flows: characterization of mean flow and turbulence. In preparation (2016);
4. M. G. Giometto, J. Fang, and M. B. Parlange. Large- and very-large-scale motions in katabatic flows over steep slopes. In preparation (2016);
5. M. G. Giometto, E. Trujillo, K. C. Leonard, T. L. Maksym, J. Fang, C. Meneveau, M. Lehning, M. B. Parlange. Large-eddy simulation of atmospheric boundary-layer flow over Antarctic sea-ice formations using a dynamic roughness model. In preparation (2016);

Conference abstracts

1. M. G. Giometto, A. Christen, C. Meneveau, J. Fang, M. B. Parlange. Large-eddy simulations to characterize the role of turbulent and dispersive production, transport and dissipation of TKE over and within a realistic urban canopy. In 9th International Conference on Urban Climate (ICUC9), Toulouse, France, July 2015;
2. M. G. Giometto, A. Christen, M. Calaf, M. B. Parlange. The impact of variable building height on drag, flow and turbulence over a realistic suburban surface. In AGU General Assembly Conference Abstracts, San Francisco, USA, December 2014;
3. M. G. Giometto, J. Fang, M. B. Parlange. The vertical structure of eddy diffusivity in pure slope flows over smooth surfaces. In 67th Annual Meeting of the APS Division of Fluid Dynamics, San Francisco, USA, November 2014;
4. M. G. Giometto, J. Fang, M. B. Parlange. An inter-comparison of LES subgrid-scale models for simulations of slope flows. In 21st Symposium on Boundary Layers and Turbulence, Leeds, UK, June 2014;
5. M. G. Giometto, E. Trujillo, K. Leonard, T. Maksym, C. Meneveau, M. Lehning, M. B. Parlange. LES modeling of wind over Antarctic snow-ice formations using a dynamic surface roughness approach. In AGU General Assembly Conference Abstracts, San Francisco, USA, December 2013;
6. M. G. Giometto, M. Calaf, H. Oldroyd, J. Fang, and M. B. Parlange. High resolution LES study of the nocturnal low level jet. In EGU General Assembly Conference Abstracts, Vienna, Austria, April 2013;
7. M. G. Giometto, J. Fang, M. Putti, A. Saetta, S. Lanzoni, and M. B. Parlange. A mixed RKPM/RBF immersed method for FSI simulations. In EGU General Assembly Conference Abstracts, Vienna, Austria, April 2012;
8. M. G. Giometto, J. Fang, M. Putti, A. Saetta, M. B. Parlange. An immersed radial basis function method for FSI simulations coupled with spectral elements. XII convegno nazionale di ingegneria del vento, Venezia, Italy, October 2012.

Invited talks / seminars

- M. G. Giometto, H. Oldroyd, M. B. Parlange. Numerical simulations of katabatic flows. Meeting organized at the Complex Fluids Laboratory in The University of British Columbia (UBC), Vancouver, Canada, April 2014;
- M. G. Giometto, J. Fang, M. Putti, M. B. Parlange. An immersed meshless method for simulation of fluid-structure interaction, seminar talk at UNIL, Department of Geophysical Sciences, Lausanne, Switzerland April 2013.

Professional Experiences

- **2015:** Manuel Schmidt**,** M.Sc. thesis co-supervisor: resolution of the Gibbs phenomenon for Navier-Stokes simulations, École Polytechnique Fédérale de Lausanne, Lausanne, Switzerland;
- **2014:** Visiting Ph.D. (March - April) at department of Civil and Environmental Engineering, University of British Columbia, Vancouver, Canada;
- **2014:** Pascal Egli, M.Sc. thesis co-supervisor: turbulent flow over and within an urban canopy in Vancouver, Canada, École Polytechnique Fédérale de Lausanne, Lausanne, Switzerland;
- **2012-2013:** Teaching assistant in fluid mechanics for civil and environmental engineering at École Polytechnique Fédérale de Lausanne, Lausanne, Switzerland;
- **2012-2013:** Teaching assistant in numerical methods for civil and environmental engineering at École Polytechnique Fédérale de Lausanne, Lausanne, Switzerland;
- **2012:** Alessandro Leonardi**,** M.Sc. thesis co-supervisor: Fluid-Structure Interation and Fluid-Dynamic Analysis for Vertical Axis Wind Turbines, University of Padua, Padua, Italy;
- **2012:** Programme committee member XII Convegno Nazionale Di Ingegneria Del Vento, Venice, Italy;
- **2010:** Erasmus exchange student at the International Center for Numerical Methods in Engineering, Barcelona, Spain;
- **Reviewer** for Journal of Theoretical and Applied Climatology and Journal of Urban Climate.

Other skills

- Proficient in the use of supercomputing facilities, user at the Swiss National Supercomputing Center (CSCS);
- Proficient in Bash scripting, Fortran90, C++, Python, Matlab and in the use of the Paraview rendering software;
- Good knowledge of the OpenMP, MPI, BLAS, LAPACK libraries.